XFEL.EU TR-2017-001

CONCEPTUAL DESIGN REPORT

Dynamic Laser Compression Experiments at the HED Instrument of European XFEL

February 2017

Malcolm McMahon and Ulf Zastrau

(Editors)

for HIBEF and European XFEL

HiBEF

European XFEL

Contents

1 Introduction

by M. McMahon, J. Eggert, and U. Zastrau

1.1 General purpose and goals

Since the publication of the conceptual design report (CDR) for the High Energy Density Science (HED) instrument at the European XFEL in 2013, it has become clear that a community-wide discussion for **shock and ramp compression experiments** at the HED instrument is needed. The HED group at European XFEL and the Helmholtz International Beamline for Extreme Fields at the European XFEL user consortium (HIBEF UC) [71] agreed to do this together. This CDR on dynamic laser compression experiments at HED was drafted prior to the *Dynamic Laser Compression* workshop that was held on 12–14 September 2016 at European XFEL, where the CDR served as an outline for the presentations. Both the CDR drafting and the workshop programme were organized by Malcolm McMahon (for the HIBEF UC) and Ulf Zastrau (for European XFEL). An international team of contributing authors assembled this CDR and presented it to the entire community at the workshop.

We thank all the authors for their time and their sustained interest in ensuring that the HED instrument at European XFEL will become a world-leading platform for dynamic compression experiments. A lot of the material and ideas presented here came from proposals and results at the Matter in Extreme Conditions (MEC) instrument at the Linac Coherent Light Source (LCLS) at SLAC National Accelerator Laboratory in the USA and the FLASH facility at Deutsches Elektronen-Synchrotron (DESY) in Germany. We would like to acknowledge the contributions of both teams as well as the collaborations between experimentalists and theorists that have paved the way towards many successful experimental tests and theory developments.

- K. Appel (European XFEL, HED, Germany)
- C. Baehtz (HZDR, Germany, and HIBEF)
- E. Brambrink (LULI, France)
- R. Briggs (ESRF, France)
- T. Butcher (CLF, UK)
- B. Cauble (LLNL, US)
- B. Chen (CAEP, China)
- H. Damker (DESY, Germany)
- C. Deiter (European XFEL, Sample Environment, Germany)

- J. Eggert (LLNL, US)
- K. Falk (ELI Beamlines, Czech Rep.)
- L. Fletcher (SLAC HED, US)
- S. H. Glenzer (SLAC/Stanford Univ., US)
- S. Göde (European XFEL, HED, Germany)
- M. Harmand (UPMC Paris, France)
- A. Higginbotham (U York, UK)
- Z. Konôpková (European XFEL, HED, Germany)
- D. Kraus (HZDR, Germany)
- H.-P. Liermann (DESY, PETRA III ECB, Germany)
- M. McMahon (U Edinburgh, UK)
- M. Nakatsutsumi (European XFEL, HED, Germany)
- A. Pelka (HZDR, Germany, and HIBEF)
- G. Priebe (European XFEL, Optical Lasers, Germany)
- R. Redmer (U Rostock, Germany, and HIBEF)
- A. Schropp (DESY, Germany)
- R. Smith (LLNL, US)
- P. Sperling (European XFEL, HED, Germany)
- I. Thorpe (European XFEL, HED, Germany)
- S. Toleikis (DESY, FLASH, Germany)
- U. Zastrau (European XFEL, HED, Germany)

In addition, we would also like to thank all participants of the *Dynamic Laser Compression* workshop for their valuable input and fruitful discussions. We also acknowledge assistance in implementing comments, typesetting LaTeX, and proofreading by Karen Appel, Zuzana Konôpková (both European XFEL), and in particular Wolfgang Morgenroth (U Frankfurt). We also thank Kurt Ament (European XFEL) and Ilka Flegel (Textlabor) for the final edits and proof-reading.

1.2 Other international facilities and their mission

by U. Zastrau

Brightness is a fundamental parameter for a light source that cannot be changed by any passive optics. When LCLS became operational in 2009, the record brightness of any X-ray source on our planet increased by a billion. As a result, scientists using X-ray free-electron lasers (X-ray FELs) now have an X-ray source at their disposal that provides sub-ps pulse duration, i.e. a time shorter than a phonon period. We can now record diffraction pattern and study matter faster than ions vibrate.

At **X-ray FEL**s, there are currently two instruments that offer a combination of a ns laser shock driver and an X-ray probe beam.

At **MEC** [106] **at LCLS** [42] (SLAC, Menlo Park, USA), the ns laser can deliver about 1 J per ns with pulse durations up to 20 ns. It is a commercially available, flashlamp-pumped, frequency-doubled system. The repetition rate is limited to one shot every 7–10 min due to cooling of the laser rods. It has basic pulse-shaping capabilities. For a report about experience with this system, refer to Section 5.2. MEC's mission is to combine the unique LCLS beam with high-power optical laser beams and a suite of dedicated diagnostics tailored for this field of science (including an X-ray Thomson scattering spectrometer, an XUV spectrometer, a Fourier domain interferometer, and a VISAR system). While the large vacuum target chamber makes the instrument very versatile, it has been designed to service key scientific areas, including warm dense matter physics, high-pressure studies, shock physics, and high energy density physics [55].

Mid-term upgrade plans (2017–2018) include the installation of two more laser arms to enhance the available pulse energy to about 80 J and to implement frequency tripling.

In Japan, Osaka University and RIKEN constructed the **High Energy density Revolution of Matter in Extreme States** (HERMES) system at the SPring-8 Angstrom Compact Free Electron Laser (SACLA) experimental facility [78]. Kodama [87] have constructed a 20 J / 530 nm long-pulse laser system, which is synchronized with SACLA. Extreme states of matter with pressures of less than 100 GPa are created by the optical laser, and the X-ray FEL beam is used to study the dynamics of the compression, deformation, and phase transition of extreme states of matter. In a current upgrade, SACLA is implementing a 400 J long-pulse laser, which is a

commercial system from Hamamatsu.

At **third-generation synchrotrons**, there are two instruments that offer a ns laser for shock compression.

At the European Synchrotron radiation facility (ESRF, Grenoble, France), ID24 plans an upgrade to a **High Power Laser Facility** (HPLF) for laser shock compression. The timeline [114] foresees feasibility studies with a ~ 100 J laser at ID24, which commenced already in 2016. In April 2016, a full proposal with cost estimates and a model for operating the laser was finished. A 100 J laser should be delivered in 2018. User operation of HPLF is foreseen in 2018.

At the Advanced Photon Source (APS, Argonne, USA), the **Dynamic Compression Sector** (DCS) is under construction at Sector 35. A particular part of DCS is the laser shock facility. All the following parameters are cited from the DCS website [158], although some of the information is clearly out of date:

> Laser shock experiments will be conducted using a 100 J, 5–15 ns pulsed laser system. Additional laser system characteristics include a focused spatial profile with a 250 or 500 micron diameter flat top, pulse shape control, and high throughput (a shot every 20 minutes). This facility will be available in 2017.
>
> The DCS laser system output is 100 Joules with a 351 nm fixed wavelength. It is capable of operating continuously at a pulse per 20 minutes and features flexible pulse shape control and beam smoothing of better than 3%. The nominal pulse width is 5–15 ns, and the focused spatial profile is either a 250 or 500 micron diameter flat top.
>
> The laser-shock facility (currently under development) includes a clean room to house the laser and a specialized target chamber that includes a cryogenic target holder and large ports for diagnostics. Both transmission and reflection X-ray diffraction geometries are accommodated by automated target and laser focal spot positioning capabilities. A high-speed X-ray chopper isolates single X-ray pulses from the APS. The X-ray pulses and laser trigger are synchronized to the storage ring RF clock to ensure precise timing of the X-ray and laser pulses.

2 Scientific goals for compression with a long-pulse laser

This chapter describes the scientific goals for compression with a long-pulse laser, the pressures, temperatures, and densities needed to access the corresponding regimes, and the laser parameters required to drive the sample into this condition.

2.1 Study of phase stabilities and EOS at pressures and temperatures of the interior of extrasolar planets

by M. McMahon and R. Redmer

The prediction and subsequent discovery of the planet Neptune in the mid-19th century completed our discovery of the diverse range of solar planets. Ranging from smaller, rocky terrestrial planets up to the larger gas giants, even our own solar system offers a remarkable array of planetary conditions. Then, in the 1990s, the first confirmed extra-solar planetary discoveries were made. We now know of over 3000 planets outside our solar system, and it is already clear that the variety seen within these planets is much wider than that seen in our near neighbours. With masses ranging from a fraction of that of Earth to many times that of Jupiter and an equally wide spread in distance from the parent star, the conditions found on these exoplanets are expected to be vastly more diverse than even our own eclectic solar system offers. Theorists predict planets composed primarily of iron, carbon, water, or any of a number of other materials, in addition to larger analogues of more familiar bodies, such as the so-called super-Earths and super-Jupiters.

The physical conditions found within these planets also span a vast range—much greater than those seen within the planets of our solar system. The forms of iron, carbon, ice, etc. that exist in such planets are entirely unknown, and may not exist anywhere within our solar system. Yet, to date, only a very small fraction of the pressure–temperature (P-T) conditions relevant to even solar planetary physics have been explored. For example, static high-pressure techniques, such as the diamond anvil cell (DAC) have, until very recently, been limited to studies below 400 GPa (4 million atmospheres)—just above the Earth's core pressure, but a factor of 10 below Jupiter core conditions. And such pressures are obtainable only at room temperatures,

well below the core temperatures of thousands to ten thousands of Kelvin found within planets.

But such conditions *can* be achieved using laser compression methods, which have recently demonstrated the ability to create solid matter at several TPa, leading to a vast increase in the range of relevant phase space open to study. Coupled to the European XFEL, X-ray diffraction and spectroscopy experiments will become possible at conditions previously unobtainable at any synchrotron. Our scientific goal is to create the P–T states of matter relevant to exoplanetary interiors and to study the structural and melting behaviour of key planetary materials at these conditions. Our initial goal will be to achieve pressures of 1 TPa and temperatures up to 10 000 K using 5 ns, frequency-doubled 50 J pulses from the DiPOLE100X laser focused to 100 µm. In order to keep the compressed sample cool enough to probe solid rather than liquid phases, ramp compression using time-profiled laser pulses will be essential.

2.1.1 Melting curve and structures of Fe up to 1 TPa and 8000 K

The melting curve and high-P–T structural behaviour of Fe (and its alloys) is of vital importance to geoplanetary science. For example, the temperature of Earth's inner-core boundary is expected to be close to the melting temperature of Fe at 330 GPa, and this temperature places very important constraints on parameters such as heat flow to the mantle and cooling rate, both of which are vital to understanding the Earth's internal dynamics. The importance of knowing the behaviour of Fe at extreme P–T conditions has driven technique advances in extreme-conditions research for decades, but, despite this and a great number of studies, almost nothing is known about the melting and structural behaviour of solid Fe above 300 GPa. The computed phase diagram of Fe to 100 TPa and 40 000 K is shown in Figure 2.1.

The highest pressure at which melting was confirmed in a DAC is ~2 Mbar [4, 16], and considerable extrapolation is therefore required in order to estimate the melting temperature at 330 GPa as 6230(±50) K. For more massive Earth-like planets, so-called super-Earths, with masses some 5–10 times that of Earth, the melting curve of Fe up to at least 1 TPa is required in order e.g. to determine whether they possess Earth-like liquid metallic cores and thereby understand their internal dynamics. Such P–T conditions are completely inaccessible at present using static compression techniques, and the extrapolations required from existing data are therefore enormous.

The melting temperature of Fe at 225–260 GPa is known from shock compression

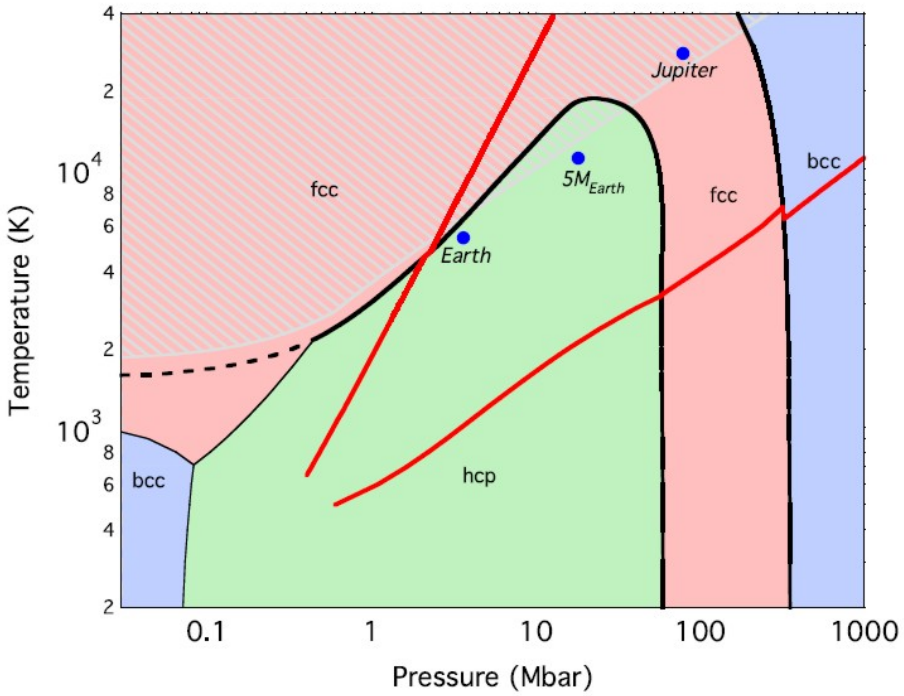

Figure 2.1: Phase diagram of iron. Figure reproduced from Stixrude [146].

studies to be 5100–6100 K, and this experimental data point has long been a high-pressure anchor for the Fe melt curve. The most recent DAC studies are in good agreement with it, and they used it in their extrapolation to 330 GPa. But we now need to measure the melting temperature above 260 GPa—initially to 500 GPa and then ideally to 1 TPa.

Such pressures and temperatures can be reached with dynamic compression, using time-profiled laser pulses to access P–T states away from the principal Hugoniot. Indeed, a recent ramp compression study of Fe reached 560 GPa and 8000 K, and showed it was still solid at these conditions [113]. Shock melting of Fe at 220–260 GPa was determined previously [108] from the effect it has on the shock wave profile, as determined by a velocity interferometer system for any reflector (VISAR, see Section 5.1). By using the European XFEL, however, melting can be determined directly through the disappearance of crystalline Bragg scattering and the observation of X-ray scattering from the liquid itself.

We propose to combine time-profiled laser pulses from the DiPOLE100X laser with European XFEL radiation to determine the melting curve of Fe to 0.5 TPa, where the melting temperature is $>$ 8000 K, with the longer-term goal of reaching 1 TPa, where melting occurs at $\sim$ 10 000 K.

2.1.2 BC8 phase of carbon above 1 TPa

It is well known that diamond is not the stable phase of carbon at ambient pressure and temperature. However, despite being metastable, its very high thermal conductivity, its excellent transparency in the visible range, and the highest bulk modulus of any material make it a material of great technological importance. Diamond is the thermodynamically stable phase of carbon above 1–10 GPa (depending on T), but the behaviour of carbon at higher pressures is almost completely unknown. As carbon is predicted to be a major constituent of exoplanetary interiors as a result of the decomposition of methane at extreme pressures and temperatures, a knowledge of what structures carbon adopts at these conditions is vital. A series of phase transitions have been predicted to occur in carbon at pressures of 0.5 to 3 TPa, and there now seems to be a consensus that diamond will transform to the cubic BC8 structure (long known in silicon) at ~1 TPa (Figure 2.2). Some evidence of a transition has been claimed based on very subtle changes in the Hugoniot slope and on the melting temperature of diamond. Unfortunately, molecular-dynamics simulations suggest that the diamond–BC8 transition may be very slow, or that diamond may remain metastable throughout the stability range of BC8. The BC8 phase may also be metastable when relaxing back to ambient conditions and may be recoverable at ambient pressure, as it is in silicon. The recovery of BC8 carbon to ambient conditions would provide us with a remarkable new allotrope of carbon never previously seen.

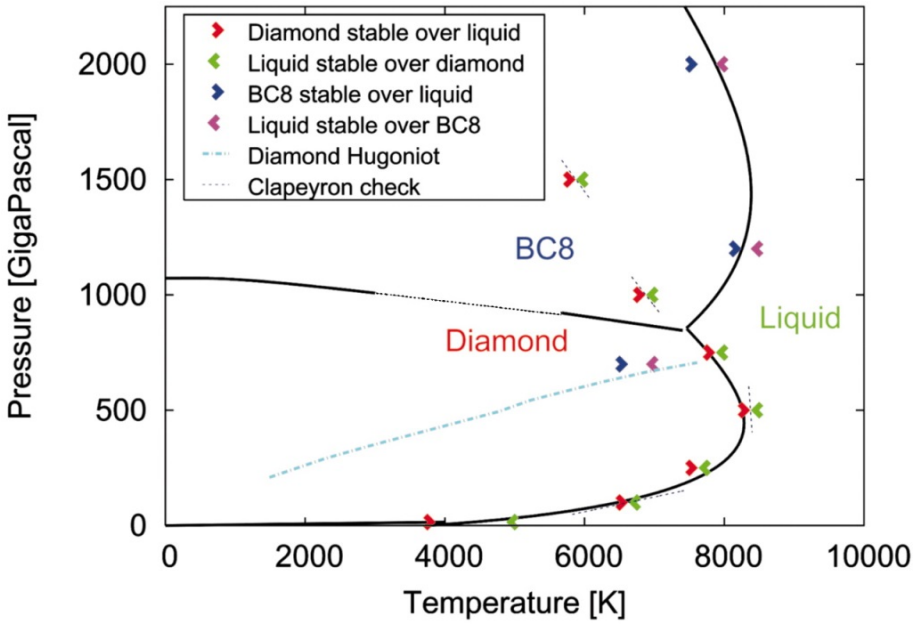

Figure 2.2: Computed phase diagram of carbon to 2 TPa and 10 000 K. Figure reproduced from Correa, Bonev, and Galli [32].

Recent experiments at the National Ignition Facility (NIF) at Lawrence Livermore National Laboratory (LLNL) in the USA ramp-compressed to 5 TPa without seeing any evidence of the BC8 phase—but no diffraction data were obtained. The observation of the BC8 phase in carbon is an extremely challenging experiment—but there will be no better place than the HED instrument at the European XFEL to obtain the diffraction data required to observe it. We propose to combine time-profiled laser pulses from the DiPOLE100X laser with European XFEL radiation to determine the structural stability of carbon above 1 TPa.

2.1.3 Metallic hydrogen

Key questions for the behaviour of H–He mixtures at high pressure in the context of planetary physics are the metallization of hydrogen—as already predicted by Wigner and Huntington in 1935 but still not proven directly—and the demixing of helium from hydrogen. By metallization, hydrogen dramatically changes its thermo-physical properties, in particular the equation of state (EOS), and electrical transport properties, which determines the interior, evolution, and magnetic field of Jupiter-like planets. Demixing of helium from hydrogen leads to vertical mass transport—first predicted to occur in the deep interior of Saturn as helium rain—and, thereby, to a substantial contribution to the intrinsic luminosity. This high-pressure effect is the major candidate to correctly describe the cooling history of Saturn, compared with homogeneous-evolution models, which all underestimate its age considerably.

Both effects are predicted to occur at 0.1 TPa pressure and at temperatures of only a few thousand Kelvin (< 1 eV), meaning that specific compression paths have to be realized in order to reach this parameter domain, preferably by quasi-isentropic compression. Such setups have been realized so far with e.g. multiple shocks using gas guns and ramp compression, as recently performed at the Z machine at Sandia National Laboratories in the USA (see Figure 2.3). The power of the DiPOLE100X laser system at the HED instrument and its pulse-shaping option would enable such experiments, but combined with the novel X-ray diagnostic tools implemented there. The demixing of helium from hydrogen is addressed in current laser-driven shock-wave experiments using pre-compressed targets. Since DAC technology will be available at the HED instrument, such setups could be realized there as well.

2.1.4 Superionic phases

First studies of the H–C–N–O complex at high pressure have revealed a rich phase diagram. Besides the various ice phases in H_2O, NH_3, and CH_4, superionic

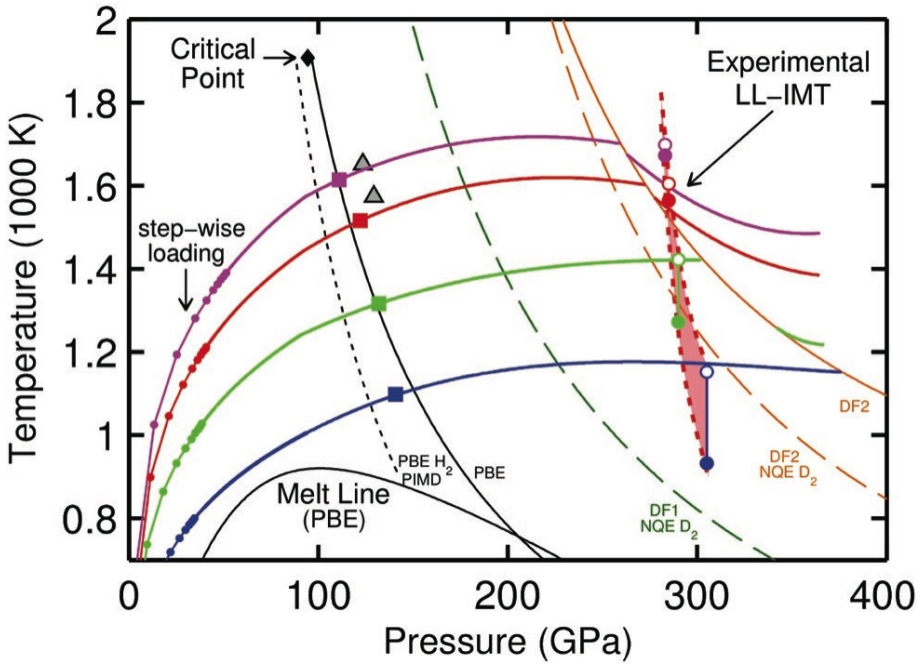

Figure 2.3: Metallization of hydrogen as a liquid–liquid first-order phase transition derived from ramp compression experiments performed at Sandia's Z machine. Figure reproduced from Knudson, Desjarlais, Becker, et al. [86].

phases have been predicted for water and ammonia. This exotic phase represents a combination of a solid lattice composed of the heavy ions and a fluid of protons almost freely diffusing through the lattice. Important questions in the context of planetary physics are related to the region where such superionic phases occur in the P–T diagram and to their stability against mixing with other components, e.g. in H_2O–NH_3 mixtures (see Figure 2.4). Another fascinating question is whether or not carbon might demix in the complex H–C–N–O mixture at high pressures so that carbon rain would occur, similar to helium rain in Saturn. Since pressures might be sufficient to form diamond, this has led to the speculation of diamond rain or diamond layers in Neptune-like planets.

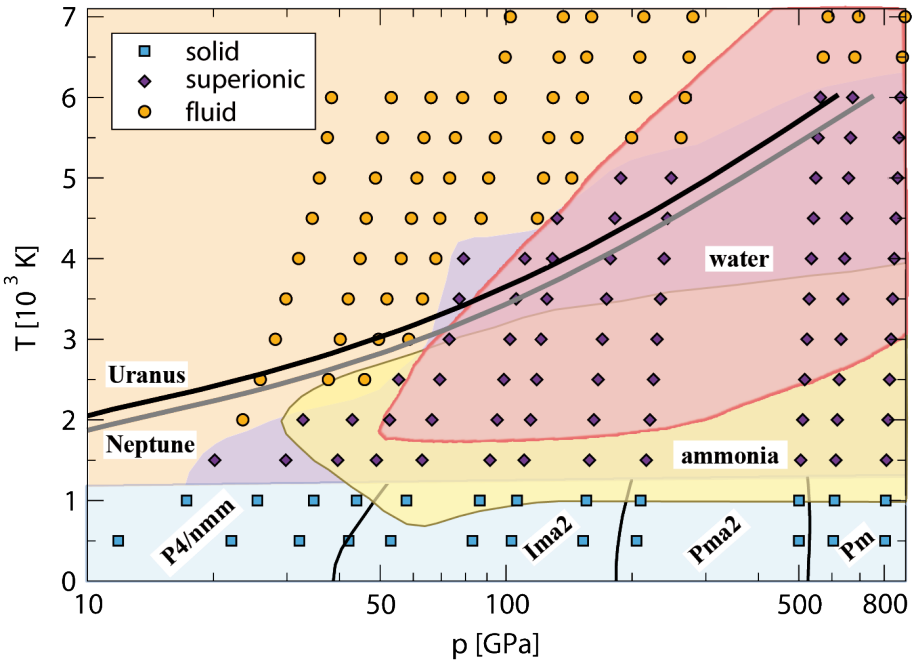

Figure 2.4: Phase diagram of a 1:1 water–ammonia mixture. Figure reproduced from Bethkenhagen, Cebulla, Redmer, et al. [11].

2.2 Dynamic compression pathways

by J. H. Eggert and A. Higginbotham

While the study of high-pressure phases, EOS, and other planetary relevant data will clearly be a key goal for many experiments at the HED instrument, there remain many outstanding questions about the fundamental response of materials to dynamic compression. The shock- and ramp-based experiments described above access high-pressure states through compressions with strain rates on the order of 10^8–10^{10} s^{-1}, which are of course many orders of magnitude above that expected in static, and even dynamic, diamond anvil cell compression experiments. It is therefore critical that we carefully study and account for the dynamic nature of materials response. In particular, we must understand the effects of compression pathway and associated strain rate dependence on the final compressed state.

2.2.1 Inelastic response

The deformation pathway of materials undergoing dynamic compression is often complex. Figure 2.5 illustrates the response of a sample subjected to a planar

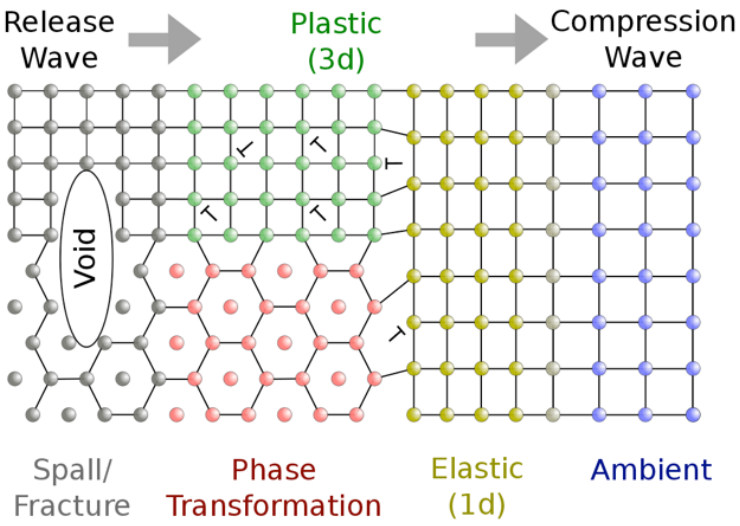

Figure 2.5: Schematic of the complex dynamic compression pathway of a typical solid target undergoing dynamic compression. Any given material may exhibit all, or just a subset, of these responses, or indeed, may have a more complex response with multiple high-pressure phases / plasticity mechanisms. Figure by A. Higginbotham after J. McNaney.

compression to multi-100 GPa pressures. Crucially, in all materials, response is initially mediated by a planar, elastic (1d) response. This elastic precursor can be significant, with precursor stresses of up to 70 GPa seen in short-pulse compression experiments coupled with X-ray diffraction [100]. This resistance to deformation, or strength, is a key characteristic of solid matter, and, critically, its influence is unavoidable in the uniaxially driven and thus anisotropic compression waves utilized in laser-based experiments.

Upon reaching the elastic limit, the material will generally act so as to revert back towards a more favourable, hydrostatic stress state. This may be via a phase transition, via the generation and flow of defects, via crystallographic tinning or via crystal plasticity. Plasticity in rapid, uniaxially-strained dynamic compression experiments is more prevalent and may occur by different mechanisms than within the slower, more hydrostatic environment provided by diamond anvil cells. The scale of this effect can be understood by appealing to Orowan's equation for the rate of plastic strain, ϵ_p,

$$\epsilon_p = \rho v b \tag{2.1}$$

where ρ is the density of defects mediating plastic flow, v the average velocity of such defects, and b the Burgers vector associated with them. Assuming modest strain rates of around $10^8\,\mathrm{s}^{-1}$, corresponding to around 10% strain over a nanosecond,

one can estimate defect densities of around 10^{10} cm^{-2}. This is a figure orders of magnitude higher than those found in typical engineering materials. This suggests that the plastic flow rates seen experimentally require the *in situ* generation of large volumes of defects to mediate plastic response. Moreover, at these significant defect densities, materials strength can become significant, and thus stress anisotropy a significant consideration. Given this, it is clearly necessary not only to understand the final state of materials undergoing dynamic compression, but also to study the significant microstructural modification required to reach such states.

Materials may also relieve the applied uniaxial strain by structural phase transition. This can potentially alleviate the need for large-scale plasticity by accommodating strain anisotropy within phase mixtures, a change of crystal symmetry, or the formation of small, rotated crystallites. Here again, there is much that still needs to be understood about the progression of such mechanisms. For example, the texture evolution of materials can be used as a diagnostic of the relative orientation and therefore the transition mechanism followed on the path between phases [99].

As well as providing information on structure, X-ray diffraction is able to access information on strain anisotropy (and hence infer strength). In carefully crafted experiments, it can reveal details of microstructure [30, 147, 68]. The high-quality X-ray beam and large reciprocal space coverage afforded by HED/HIBEF will enable such studies to be greatly extended. Moreover, the fact that the European XFEL pulses are shorter than a phonon period and that the beam can be focused to below 100 nm, allows for unprecedented spatial and temporal resolution.

2.2.2 Strain rate dependence

Shock compression, although conceptually simple, is far from the only dynamic route to high pressure. It can be considered as a limiting (stable) case of strain rate. As discussed in the work of Swegle and Grady, a near-universal law exists for typical materials in which the strain rate scales as the fourth power of shock stress, regardless of the underlying physics mediating inelastic response [149]. For elemental metals at 100 GPa, this implies strain rates of over 10^9 s^{-1} or compression timescales below 100 ps.

However, such high strain rates bring with them highly irreversible and entropic loading paths. This means that most materials shock melt at around 100–200 GPa, thus ramp (shockless) compression techniques are required to access the multi-100 GPa states, which are of considerable interest to applications such as planetary science and materials synthesis. In doing so, we encounter the potential

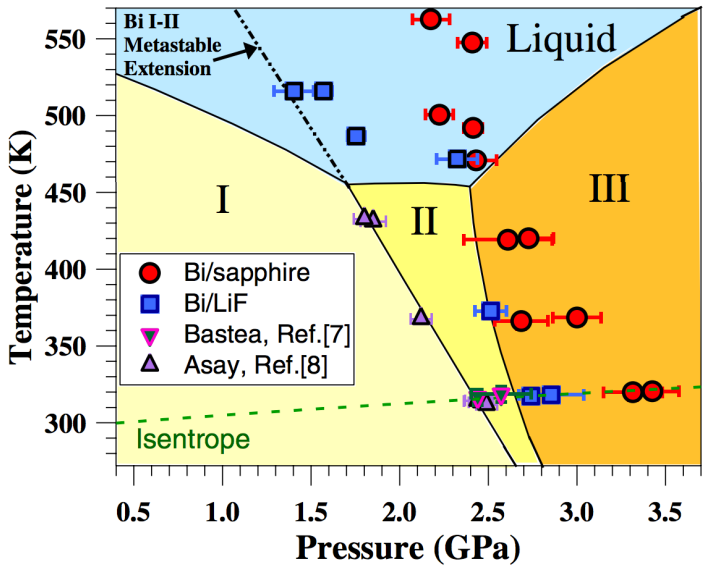

Figure 2.6: Statically determined Bi phase diagram with the inferred I→II phase transition boundary at strain rates on the order of $10^6\,s^{-1}$. Figure reproduced from Smith, Eggert, Saculla, et al. [140].

for complications due to strain rate effects. In particular, kinetics, which may be on a comparable timescale to loading, can lead to significant effects, where the alteration of loading rate can have significant effects on materials response. As shown in Fig. 2.6, Smith et al. infer a significant shifting of phase transition boundaries in Bi during ramp compression where kinetic and hydrodynamic timescales become comparable [140].

Understanding the effects of kinetics on sample response is a key goal for research at HED/HIBEF. Once again, the addition of high-quality X-ray diffraction to confirm the nature of high-pressure phases is critical, not least as the effects of kinetics are coexistent with the complications and modifications to material response due to uniaxial loading, as discussed above.

In summary, studies of dynamic compression are far from limited to a focus on final state, but there are significant outstanding questions as to how this compression occurs, and indeed in how this final state depends on, and is influenced by, the compression path.

2.3 Properties of shock-compressed WDM

by S. Toleikis and R. Redmer

Warm dense matter (WDM), i.e. material at solid-like densities or beyond and at temperatures of some eV (1 eV = 11 605 K), represents the state of matter relevant for the interior of planets. For instance, a pressure of 136 GPa and a temperature of about 4000 K are expected at the core–mantle boundary (CMB) of Earth, separating the outer liquid iron core and the lower rock mantle. The CMB in Jupiter, separating a core of so-far-unknown composition and an inner liquid envelope composed of metallic hydrogen, helium, and a small amount of heavier elements, is predicted at a pressure of $>$ 4000 GPa and a temperature of about 20 000 K.

Since the discovery of extrasolar planets in the mid-1990s, a great diversity of planets has been found in mass and composition, ranging from Earth-like planets, super-Earths, and Neptune-like planets up to Jupiter-like planets and even more massive super-Jupiters. Three major material classes can be identified: the lightest elements hydrogen and helium are the main components of gas giants like Jupiter and Saturn, Neptune-like planets are mainly composed of H–C–N–O mixtures, and minerals of the MgO–FeO–SiO_2 complex are the building blocks of Earth-like planets. For the determination of the interior structure, evolution, and magnetic field of such planets, knowledge on the thermal and caloric EOS on transport coefficients, such as electrical and thermal conductivity, and on material properties, such as viscosity and diffusion in the WDM regime, is of outstanding importance.

The EOS of hydrogen (metallization) and hydrogen–helium mixtures (demixing) have been discussed in Section 2.1.3 and that of H_2O–NH_3 mixtures (superionic phase) in Section 2.1.4. In order to benchmark theoretical predictions based on *ab initio* simulations and to verify the database used in planetary modeling, dynamic compression experiments with the DiPOLE100X laser (see Section 4.1) with so-far-unprecedented resolution are planned at the HED instrument of the European XFEL; for the optical and X-ray diagnostics (see Chapters 5–7).

As a first example, we show in Figure 2.7 the high-pressure water EOS, which is key for modeling Neptune-like planets. The Hugoniot curve extracted from Z machine experiments has error bars of only a few percent and agrees perfectly with *ab initio* data. Earlier predictions of either the SESAME database and of laser-driven shock-wave experiments (note the large error bars) show a substantially softer high-pressure behaviour above 100 GPa. This discrepancy could be addressed in

new experiments using the DiPOLE100X laser.

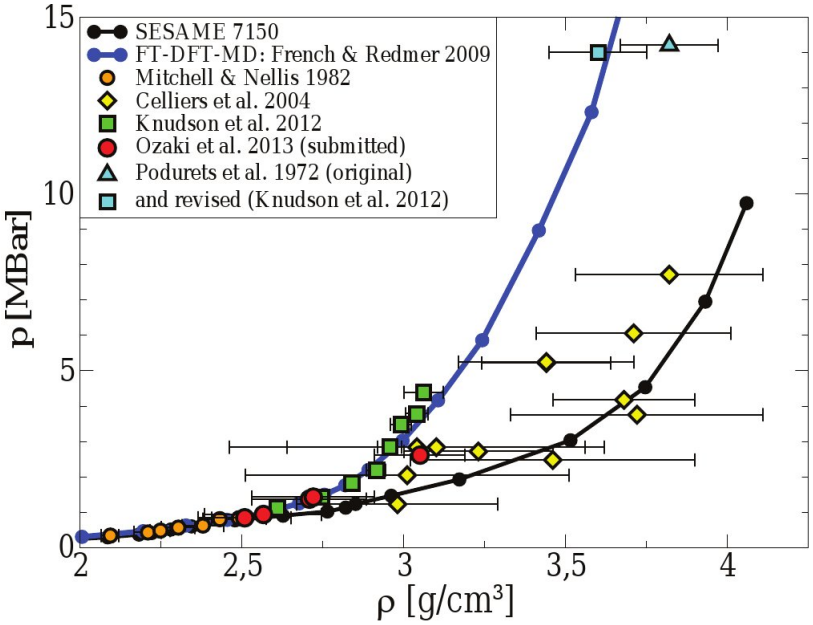

Figure 2.7: Hugoniot curve of water: Theoretical predictions based on *ab initio* simulations (FT–DFT–MD: blue line) agree very well with experiments performed at the Z machine (green boxes). Note the large error bars of previous laser-driven shock-wave experiments (yellow diamonds), which show agreement with Knudson, Desjarlais, Lemke, et al. [85].

Another representative example is the determination of the electrical conductivity in WDM. Measuring this transport coefficient in dense plasmas has been a challenge for decades, and the large error bars (typically 20–50%) that are present in dynamic compression experiments prevent a discrimination of various existing theoretical approaches. However, this is all-important for state-of-the-art dynamo simulations, which predict the magnetic field structure of planets. Recently, the direct extraction of the electrical conductivity from the collisional-damped plasmon feature has been shown for the first time in X-ray Thomson scattering experiments (see Figure 2.8). For this goal, the X-ray scattering spectra have to be measured with high resolution, enabling the determination not only of the collision frequency required for the electrical conductivity but also of the dispersion relation and damping of the plasmon mode in WDM.

A more microscopic property in a plasma/WDM environment is the effect of ionization potential depression (IPD), as atomic energy levels are significantly altered by electric fields of neighbouring ions and by free electrons. This can significantly alter the ionization balance and limit the number of accessible bound states (pressure ionization), shifting the charge state distribution (CSD) in the direction of increased ionization. This shift strongly affects the thermodynamic properties of the system,

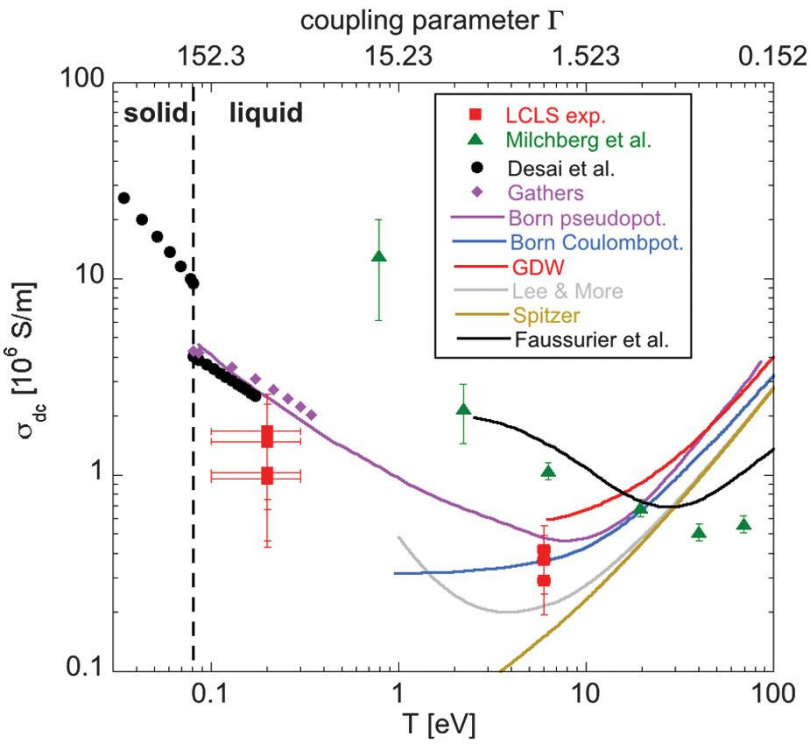

Figure 2.8: Electrical conductivity of aluminium as derived from self-Thomson scattering experiments performed at LCLS (red boxes) [144]. Note the great scatter of theoretical predictions for the WDM region. A unified theory for the liquid metal up to the WDM region is necessary.

including its EOS and opacity, and as such the IPD is of fundamental importance. Despite its importance, experimental data on IPD in dense systems remain elusive due its complication to directly measure it.

With the advent of X-ray FELs, an experiment on aluminium by Vinko, Ciricosta, Cho, et al. [157] showed that, by varying the photon energy of the X-rays that both create and probe the plasma, and by observing the K_α fluorescence, one can directly measure the position of the K-edge of the highly charged ions within the system. The results are found to disagree with the predictions of the extensively used Stewart–Pyatt model (SP), but are consistent with the earlier model of Ecker and Kröll (EK), which predicts a significantly greater depression of the ionization potential [28] (see Figure 2.9).

As one can see in Figure 2.9, the discrepancy between the two models becomes larger for higher charge states and leads to the fact that, e.g. in Al VIII, the M-shell would be still bound according to the SP model, whereas in the EK model the M-shell lies already in the continuum. As both models are simple, semi-classical models, they

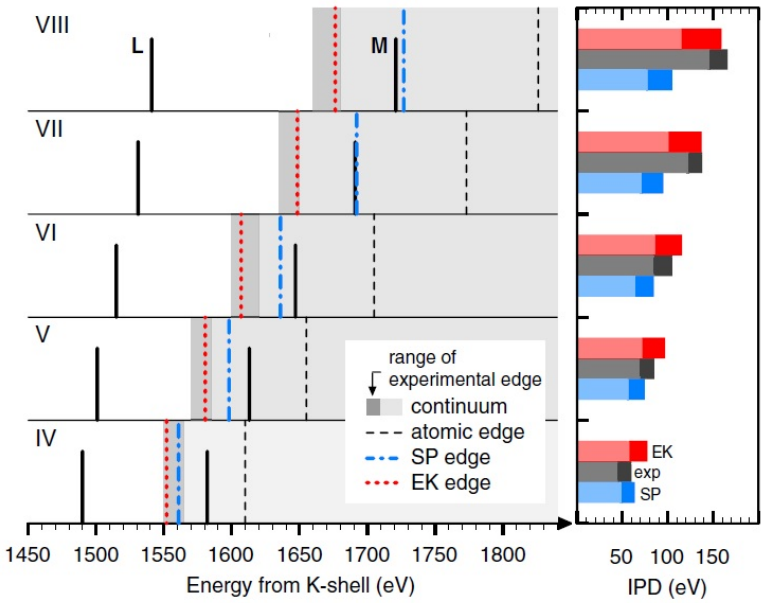

Figure 2.9: *Left:* The grey region shows the continuum for different charge states in aluminium determined from the experiment and the values given by the SP and EK calculations. *Right:* Measured and simulated IPD values. Figure reproduced from Ciricosta, Vinko, Chung, et al. [28].

are both unlikely to fully capture the complex physics of atomic systems embedded within dense plasma environments over wide ranges of plasma conditions and charge states. Thus, more sophisticated self-consistent models of IPD within dense WDM / plasma environment are needed. Further IPD data from shock-compressed matter experiments would certainly broaden our understanding. However, such challenging experiments are planned at the HED instrument.

2.4 Non-equilibrium state in shock-compressed matter

by U. Zastrau

Astrophysical objects typically evolve on very slow timescales—at first glance, one would therefore associate ultrashort dynamics in WDM with experimental shortcomings in its preparation (such as finite laser pulse lengths and small laser foci) rather than with fundamental properties.

However, beyond gaining knowledge about quasi-static properties such as the EOS and boundaries in the phase diagram, the scope is to measure the transport properties of WDM. It is obvious that heat and radiative transport through various layers will influence the layer structure and convection of astrophysical objects, and that electrical AC and DC conductivity will strongly affect magnetic fields. Transport properties are commonly accessed by the introduction of a non-equilibrium state and the subsequent time-resolved observation of the re-establishment of equilibrium. These properties are inherent to the electronic subsystem and hence evolve on ultrafast timescales.

The rate at which atoms and ions within a plasma are further ionized by collisions with the free electrons is a fundamental parameter that dictates the dynamics of plasma systems at intermediate and high densities. While collision rates are well known experimentally in a few dilute systems, similar measurements for non-ideal plasmas at densities approaching or exceeding those of solids remain elusive. Concerning collisions of an excited (*warm*) free electron with other free electrons, this is described as an electron scattering with a thermally equilibrated electron gas. If the material is cold (e.g. a cold metal), it has a band structure due to the ion lattice, and the phase space for an electron after the collision is different from the phase space within a hot electron gas. So the mean free path for the hot electron to equilibrate with a material is a function of (ion) temperature, even for collisions with the free electrons. In this context, we note that for an ideal plasma, Debye screening is valid. Electron fluctuations are screened on the Debye screening length. This also impacts the electron–electron collision rate, since the Debye screening length limits the range of the Coulomb collisions.

2.5 Temperature measurements and ion-acoustic modes on WDM

by U. Zastrau

2.5.1 Debye–Waller factor in XRD

At an X-ray FEL instrument dedicated to HED research, dynamic laser-compressed samples can be characterized with respect to shock speeds (VISAR), density and phase transitions (X-ray diffraction, XRD), ionization degree (X-ray emission spectroscopy, XES; X-ray absorption near-edge structure, XANES) and several other parameters. However, a direct temperature measurement, essential in the P, T, V ensemble for an EOS, is one of the most challenging tasks. Streak optical pyrometry (SOP) is a possibility. An indirect diagnostic uses the Debye–Waller effect for crystalline media, where temperature is encoded in the intensity of both the Bragg spots and the diffuse scattering.

Before a solid becomes a plasma and evolves into a strongly coupled fluid, it is usually in a (poly-)crystalline state. Here, incoherent elastic scattering is strongly suppressed by destructive interference from neighbouring atoms except for wave vectors that satisfy the Bragg condition. Heating of the ions leads to displacements about their equilibrium position, which reduces this destructive interference. For a mono-atomic crystal in the Einstein model, the scattering intensity can be written as

$$I = I_e f^2 e^{-2W} \sum_m \sum_n e^{i\vec{k}\cdot(\vec{r_m}-\vec{r_n})} + I_e f^2 N(1 - e^{-2W}) \tag{2.2}$$

where I_e is the average intensity and the sum is taken over m and n independent atoms. The first term represents coherent elastic scattering, weighted by the double sum, while the second is the incoherent scattering. The intensity of each term is modified by the Debye–Waller factor, which can be written as [60]

$$2W = \frac{\pi^2 \vec{k}^2 h^2}{4 M k_B T_D} \left(\frac{T_i}{T_D}\right)^2 \tag{2.3}$$

where M is the mass per unit cell, T_D is the Debye temperature, and T_i is the ion temperature, which we assume is at equilibrium with the electrons. Extraction of the temperature from the elastic scattering will require the measurement of accurate Bragg intensities to high diffraction angles. While possible, the challenge will be to differentiate the intensity fall-off resulting from the Debye–Waller factor with other effects that affect Bragg intensities, such as texture.

2.5.2 High-resolution inelastic X-ray scattering

The measurement of the dynamic structure factor using high-resolution inelastic X-ray scattering (hrIXS) with meV resolution provides information on the properties of the ions [59]. The ion-acoustic modes in the ion–ion structure factor are separated by $2\hbar\omega_{pi} \sim 0.2$–$1$ eV in most WDM states (ω_{pi} is the ion–plasma frequency). Experiments at small q values (small scattering angles) provide information about the acoustic waves, in particular about the longitudinal sound velocity and viscosity.

At large q values (in backscattering geometry, e.g. at scattering angles of around 120–170° at ~ 7 keV), the single-particle limit is approached. Here, the individual motion of the ions leads to a Doppler broadening of the scattered X-rays, which is directly related to temperature. Here, hrIXS with a resolution on the order of 10 meV could be used for measuring ion-acoustic modes and phonons. Since this is an absolute ion temperature measurement, it can be used to calibrate the Debye–Waller factor method described above.

3 Showcase experiments

3.1 Probing the structure of high-density alkali metal fluids

by M. McMahon

It is clear nowadays that structural complexity is ubiquitous in high-density matter. In solid elemental metals, this complexity can arise from density-induced localization of electrons on interstitial sites, resulting from strong quantum mechanical constraints in the electronic wave functions of both core and valence electrons. This electron localization into non-nuclear maxima (NNMs) can result in electride structures, where the NNMs act as almost massless pseudo-anions. Electronic structure calculations have revealed that electride phases are widespread at ultrahigh densities, including in aluminium above 3.2 TPa, but are most readily obtained in the alkali metals Li and Na. In Na, the localization of the electrons at 200 GPa results in a remarkable transparent insulating form, which is calculated to be stable to extremely high pressures.

But what about the fluid states—is the structural complexity seen in solid alkali metals also present in the dense fluids, and is there an electride structure equivalent? Numerous computational studies have predicted that such phases do indeed exist. In fluid Na, computation has predicted a series of pressure-induced structural and electronic transitions, analogous to those observed in solid Na, but occurring at lower pressures in the presence of liquid disorder. In Li, molecular dynamics (MD) simulations predict a series of structural changes in the fluid that again mirror those seen in the solid. Above 150 GPa, fluid Li is predicted to be metallic with a four-coordinate diamond-like structure, with significant core–core overlap and valence electrons squeezed into interstitial regions. At higher pressures still, quantum-MD studies find a phase of Li whose conductivity is typical for a degenerate electron liquid. The prediction of this phase in the liquid may suggest the existence of similarly exotic solid phases, at pressures beyond the limits of any computational studies conducted to date.

Computational studies thus predict that there is indeed both structural complexity in the fluid alkali metals and a dense-liquid electride equivalent. *But none of this has been verified experimentally to date*. High-pressure high-temperature studies of the alkali metals are constrained by the extremely high chemical reactivity of the samples and their very high diffusivity. In Li, this means that static compression studies using

a diamond anvil cell must be performed below 200 K in order to prevent the sample diffusing into the diamonds above 20 GPa, leading to their failure. Laser heating studies of the alkali metals in DACs are therefore prohibitively difficult.

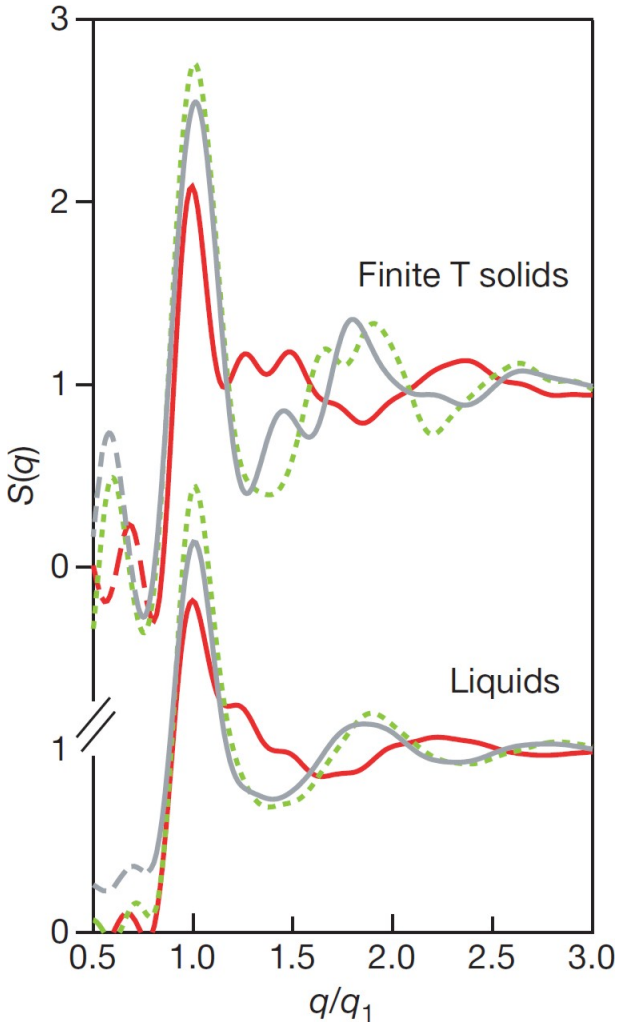

Figure 3.1: Structure factors $S(q)$ in solid and liquid sodium as a function of pressure and temperature. The bottom three curves are liquid $S(q)$ values computed at 3 GPa and 650 K (grey line), 59 GPa and 745 K (dotted line), and 106 GPa and 500 K (red). The upper three curves are computed S(q) values of the following solid phases: bcc at 20 GPa and 700 K (grey line), fcc at 69 GPa and 500 K (dotted line), and cubic *cI*16 at 105 GPa and 200 K (red). The curves are scaled with respect to their first peak positions, q_1. Figure reproduced from Raty, Schwegler, and Bonev [117].

But extreme P–T conditions can be obtained in Li and Na using dynamic compression, where the nanosecond duration of the experiments prevents both diffusion and chemical reactions. Both metals are extremely compressible and have low melting temperatures. They therefore both melt at pressures less than 6 GPa under shock compression. However, using shock and ramp compression, it is possible

to melt the sample using an initial shock and then ramp-compress the resulting fluid to high densities with little further increase in temperature. By varying the timing and energies of the shock and ramp, large areas of P–T space can be surveyed to search for the predicted transitions.

Using the pulse-shaping capabilities of the DiPOLE100X laser, we propose to shock and ramp-compress Li, Na, and K to pressures and temperatures completely inaccessible to static compression techniques. The three different metals probe *s-p*, *p-d*, and *s-d* electron hybridization, respectively. We will obtain simultaneous diffraction and inelastic X-ray scattering data from the hot dense liquids to determine changes in their density and ion structure. Initial studies will be to 100 GPa and 5000 K to investigate previously predicted structural changes, with the ultimate aim of reaching 500 GPa and 10 000 K where quantum-MD simulations predict the existence of a degenerate electron liquid in Li.

Equipment needed:

- **X-ray detectors**
  Two large-area detectors. Positions maximized to obtain the necessary q range for the diffraction from the liquid phases. Background reduction vital.

- **ns drive laser**
  2ω, with shock and ramp pulse profile and laser energies to be determined by hydrodynamic simulations, and optimized by experiment. Variable electronic timing relative to X-ray pulse from -5 ns to $+25$ ns. Focal spot size 100–200 µm.

- **VISAR**
  Yes. Can also be used to measure the reflectivity of the fluids at the VISAR laser wavelength.

- **Streaked optical pyrometer (SOP)**
  Yes.

- **European XFEL parameters**
  25 keV (to maximize q range of data), but will be optimized to obtain highest signal-to-noise ratio of liquid scattering data.
  Maximal pulse energy, pulse length not critical. Focus 20 µm.

- **Repetition rate**
  Shot on demand. Quality of data more important than quantity.

3.2 Transverse geometry—90° shock probing

by U. Zastrau and A. Higginbotham

Currently, experimental setups at X-ray FEL facilities are mostly refined versions of known geometries from either the laser plasma or synchrotron community, rather than designs that are unique to the capabilities of X-ray FELs. However, transverse geometry (90° between shock propagation and X-ray probing, see Figure 3.2) is maybe the first setup tailored for X-ray FELs.

If the X-rays are aligned collinearly with the shock wave propagation, the X-ray beam usually strikes through released, compressed, pre-compressed, and cold material all at the same time. By contrast, transverse geometry probes only the cold state plus a single compressed state at a time. However, this ideal picture needs some clarification: gradients from lateral shock fronts may still contain about 10% other (intermediate) phases. Experimentally, no peak broadening from pressure gradients is observed when using the transverse geometry; thus, it seems not to be a major problem. The typical liquid background peak—present in collinear geometry—is not observed in 90° geometry, although diffraction from liquid formed on release at the sides of the target can be seen. The transverse geometry also probes an order of magnitude less sample volume than the collinear geometry. The liquid scattering signal is the diffuse ring in the lower part of the detector (Fig. 3.2), it just happens to have a solid material peak overlapping.

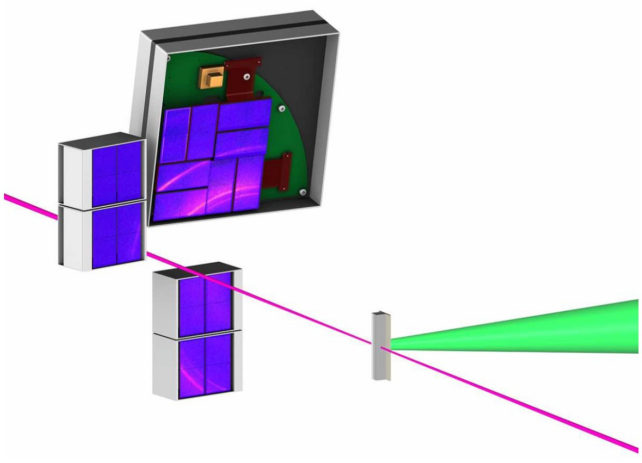

Figure 3.2: Diffraction setup in transverse geometry. *Green:* ns laser. *Purple:* X-ray FEL beam, arriving from the bottom right.

Normal geometry:

- **Phase**: ~ 2 µm thick
- **Shock front**: ~ 0.1–0.01 µm thick
- **Gradient**: 1–10%
- **Thickness**: ~ 2 µm
- **Spot size**: ~ 50 µm
- **Probed volume**: 4000 μm^3

Transverse geometry:

- **Phase**: ~ 100 µm thick
- **Rarefactions**: ~ 10 µm thick
- **Gradients**: 10%
- **Spot size**: ~ 2 µm
- **Probed volume**: 300 μm^3

Many interesting applications of transverse geometry can be though of, especially when coupled with X-ray phase contrast imaging (PCI). However, this needs special target design, mostly 10 µm needle-like targets.

Equipment needed:

- **X-ray detectors**
  Two large-area detectors. Positions maximized to obtain maximal q range. Background reduction vital.

- **ns drive laser**
  2ω, with shock and ramp pulse profile and laser energies to be determined by hydrodynamic simulations, and optimized by experiment. Variable electronic timing relative to X-ray pulse from -5 ns to $+25$ ns. Focal spot size 100–200 µm.

- **VISAR**
  Yes.

- **Streaked optical pyrometer (SOP)**
  Yes.

- **European XFEL parameters**
  10–25 keV (to maximize *q* range of data and transmission through thick samples). Maximal pulse energy, pulse length not critical. Focus ~ 5–10 µm.

- **Repetition rate**

Shot on demand to 10 Hz, matching DiPOLE100X repetition rate.

3.3 Counter-propagating shocks

by U. Zastrau and S. H. Glenzer

Here, two ns laser beams of equal strength launch shock waves on opposite sides of a planar target. With counter-propagating shocks, one can reach higher final densities. This comes at the cost that VISAR cannot be coupled with the experiment. In counter-propagating shock experiments at MEC, less than 5% gradients in the plasma parameters are observed in Al samples, although Al may be more forgiving than other materials. Meanwhile, results from graphite and diamond are under analysis.

Counter-propagating shocks collide head-on and therefore lead to zero velocity at coalescence; this constraint could be used to close the Hugoniot relations, but in order to apply this assumption, one needs very precise laser and shock control.

Equipment needed:

- **ns Laser drive**:
  two equal beams (energy, pulse duration, focus) from opposing sides of the target, aligned to the same point.
- **VISAR**: no.
- **X-rays**: any.
- **X-ray diagnostics**: any.
- **Targets**: mostly planar. Could be foils or also planar liquid jets.
- **Repetition rate**: any.

3.4 Chemistry of mixing and demixing in warm dense planetary liquids

by D. Kraus

Giant planets in our and other solar systems usually consist of mixtures of various light elements (H, He, C, N, O, etc.) [63]. Here, the constituents' chemistry of mixing and demixing plays a crucial role for the internal dynamics of such planets. Prominent examples are hydrogen–helium demixing in Saturn [93] or possible diamond precipitation in Uranus and Neptune due to methane dissociation and phase separation into liquid carbon/diamond and hydrogen [123].

X-ray scattering techniques can be highly sensitive to these kinds of demixing processes, a As the ionic structure factor, usually denoted $S_{ii}(k)$, contains all the microscopic correlations of the atoms/ ions, and, at the same time, the amplitude of elastically scattered X-rays from a sample, $W_{el}(k)$, is directly proportional to this quantity. For small k, which is equivalent to long-range correlations, $S_{\mathrm{ii}}(k)$ can be highly sensitive to mixing/demixing, due to the cross correlation between different species. In general, the elastic scattering amplitude of a multicomponent system is given by [163]:

$$W_{\mathrm{el}}(k) = \sum_{a,b} \sqrt{x_a x_b}[f_a(k) + q_a(k)][f_b(k) + q_b(k)]S_{ab}(k), \tag{3.1}$$

where $x_{a,b}$ are the number fractions of the different ion components, $f_{a,b}(k)$ denote the atomic form factors, $q_{a,b}(k)$ the screening cloud due to free electrons, and $S_{ab}(k)$ are the partial ion structure factors.

Ideally, the scattered radiation is monitored k-resolved and spectrally resolved (at specific k values) simultaneously. In particular, a large-area X-ray detector can record the diffraction pattern and thus the relative variations of $W_{\mathrm{el}}(k)$ at different scattering angles (see Figure 3.3). It can also be highly sensitive to phase separation, e.g. the creation of solid single-species chunks out of a multicomponent liquid. At the same time, a spectrometer at large enough angles guaranteeing S_{ii} to be sufficiently close to unity can quantify absolute values for $W_{\mathrm{el}}(k)$ via the ratio of elastically and inelastically scattered radiation. This provides an absolute scale for the diffraction data. Additional spectrometers at smaller k values with the relative sensitivities cross-calibrated to the large-k spectrometer can lead to even higher precision in the absolute scale of the diffraction. These results can then be compared to theoretical model predictions for $S_{\mathrm{ii}}(k)$. In case of demixing, leading to strong density fluctuations on the nanoscale, scattering at very small k (SAXS) can be sensitive to the absolute size of these density fluctuations with an appropriate resolution down to nanometres or below.

Many of the described methods were recently demonstrated at LCLS (experiment LL58 in May 2016), where the demixing and phase separation of hydrocarbons into pure diamond and hydrogen could be observed at pressures of 150 GPa and temperatures around 5000 K. Using the DiPOLE100X laser with a sophisticated pulse-shaping capability, this technique can be applied to higher pressures and different material mixtures, e.g. hydrogen–helium, where a comparable change in scattering intensity at low k is expected [164].

Equipment needed:

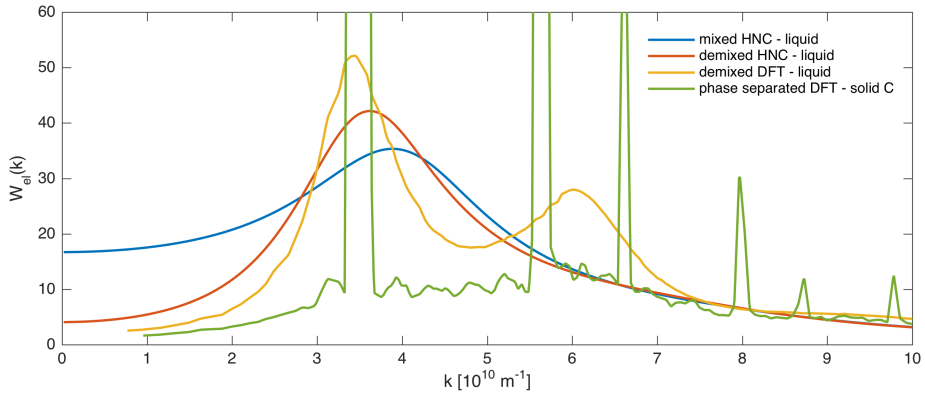

Figure 3.3: Elastic scattering amplitude of fully mixed or fully demixed CH at 3 g/cm^3 and 6000 K, calculated with a hyper-netted chain (HNC) approach and density-functional theory (DFT). Highly dominated by the carbon atoms, the elastic scattering gives a strong difference between mixed and demixed CH at low k. At the same time, the underlying carbon structure is highly visible at intermediate k, especially in case of phase separation showing strong diffraction maxima. Large k can be used for normalization, since the elastic scattering will be very similar for all cases (except when a Bragg condition is met in case of solid C).

- **Laser drive**
  ~ 100 J total energy in 10 ns, ~ 200 µm spot or larger. Flat top (single shock), step pulses (multiple shocks), or ramp pulse. Highly reliable pulse shaping required.

- **VISAR**
  100 ps temporal and 5 µm spatial resolution. One-dimensional field of view of ~ 300 µm. High dynamic range (~ 10000:1).

- **X-rays**
  ~ 10 keV photon energy, ~ 10^{12} photons per pulse, ~ 20 µm spot size.

- **X-ray diagnostics**
  Large-area X-ray detector for diffraction (covering 2θ range of ~ 15° to ~ 80°), ~ 3 HAPG spectrometers for spectrally resolved X-ray scattering (< 5 eV resolution, variable angle, whole range should cover ~15°–170°), SAXS.

- **Targets**
  Cryogenic techniques will be required for H–He experiments, otherwise flat foils (may consist of several layers and optional VISAR window).

- **Repetition rate**
  Shot on demand.

3.5 Distinguishing dynamic plasma models from plasmon dispersion in 1 Mbar matter

by U. Zastrau and P. Sperling

Modeling astrophysical objects, e.g. the interiors of giant planets [24, 105], low-mass stars, and brown dwarfs [18], requires an understanding of matter at pressures on the order of $P = 100$ GPa [72, 88] and temperatures $T \sim$ few eV [110]. In addition, the success of inertial confinement fusion [80] depends on the relevant equation of state [84, 17], but more importantly on the dynamic thermodynamic [89] and transport properties [48] at 100 GPa.

These can only be accessed by inelastic scattering experiments. Seeded X-rays in combination with a monochromator will allow the determination of highly resolved dynamic structure factor data [143]. One can thus explore the validity of Thomas–Fermi models at low temperatures (< 1 eV) and of local field corrections (LFCs) for higher temperatures. The data will yield unique access to the dielectric function and thermodynamic properties, allowing calculations of the conductivity, pressure, and entropy of astrophysically relevant plasmas.

Theoretical models for the dynamic structure factor $S^0_{\mathrm{ee}}(k,\omega)$ result in vastly different plasmon dispersions. Both the (collision-less) random phase approximation (RPA) as well as the Born–Mermin approximation (BMA)—accounting for electron–ion collisions—predict a parabolic (Bohm–Gross) dispersion. But our plasmon dispersion data observed in cold metals deviate from the parabolic dispersion. Neumayer, Fortmann, Döppner, et al. [107] performed the first frequency- and k-vector-resolved plasmon spectra from shock-compressed boron at large-scale laser facilities. Although the error bars are large, their data suggest a non-parabolic, flat dispersion relation due to electron–electron local field effects, which occur simultaneously with electron–ion collisions affecting plasmon damping.

With a seeded X-ray laser, it becomes possible to distinguish between the one or other model to be employed. As an example, Figure 3.4 shows predictions for the plasmon dispersion (shift) and width (damping) for aluminium at 100 GPa pressure for various temperatures. While RPA is collision-less, BMA accounts for (weak) collisions. The pronounced influence of LFCs on the plasmon dispersion is shown, but the plasmon dispersion is not very sensitive to collisions (RPA/BMA). Our most recent calculations show excellent agreement with previous X-ray-heated plasmon data (see Figure 7.9). But the influence of collisional damping on the plasmon width is

expressed in the difference between RPA and BMA models. Note that even for small momentum transfer (forward scattering), the plasmon shift is $>$ 20 eV and its width is on the order of 7 eV.

In 2013, these shifts and width became resolvable using the highly annealed pyrolytic graphite (HAPG) X-ray Thomson scattering (XRTS) spectrometer developed and implemented at the MEC instrument [170]. A 40 µm thin HAPG crystal in the forward-XRTS provides a resolving power of $E/\Delta E \sim 1500$ (5 eV at 7 keV) for a source size of $\leq$ 50 µm. However, when higher repetition rates and low-noise detectors become available at the European XFEL, spectrometers with perfect crystals and $\sim$ 1 eV resolution can ultimately yield high-resolution plasmon spectra. A first attempt for such a spectrometer for simultaneous frequency- and k-vector-resolved measurements was proposed and tested at LCLS [154].

From our earlier experience at LCLS, the hard X-ray (8 keV) self-seeded beam has a bandwidth of $\sim$ 1 eV, but shows small spikes to the high-energy side within the self-amplified spontaneous emission (SASE) amplification bandwidth (up to 20 eV window). A subsequent monochromator with $\sim$ 1 eV bandwidth can therefore efficiently clean the X-ray spectrum.

By measuring both the plasmon dispersion and width with 1 eV resolution, we can select the appropriate model and hence precisely determine the collision rate and the local field effects. Finally, one can explore the dielectric function and optical conductivity of dense, strongly coupled matter. In the big picture, this is relevant to recent ongoing studies aiming to generate and analyse laboratory equivalents of planetary interiors—both gas giants and rocky planets—at the HED-capable X-ray FELs worldwide. More detailed knowledge on the transport properties of warm dense matter will in particular refine the modeling of the inner-core composition, magnetic dynamo effects, and thermal conductivity, impacting also planetary formation and evolution models.

A second X-ray spectrometer in backscattering geometry will allow us to cross-check the limit of non-collective Compton scattering and record Compton profiles with few-eV spectral resolution. The moderate $\sim$ 5 eV spectral resolution allows us to infer the electron temperature and density from these Compton profiles.

Typically, the temperature and density estimates from hydrodynamic simulations are used in the analysis. However, these are only fully applicable if the laser and target parameters are ideal. In contrast, after having identified the applicable model from the plasmon dispersion data (different slopes for a single condition as shown in Figure 3.4), each diagnostic (XRD pattern, plasmon spectrum, Compton spectrum)

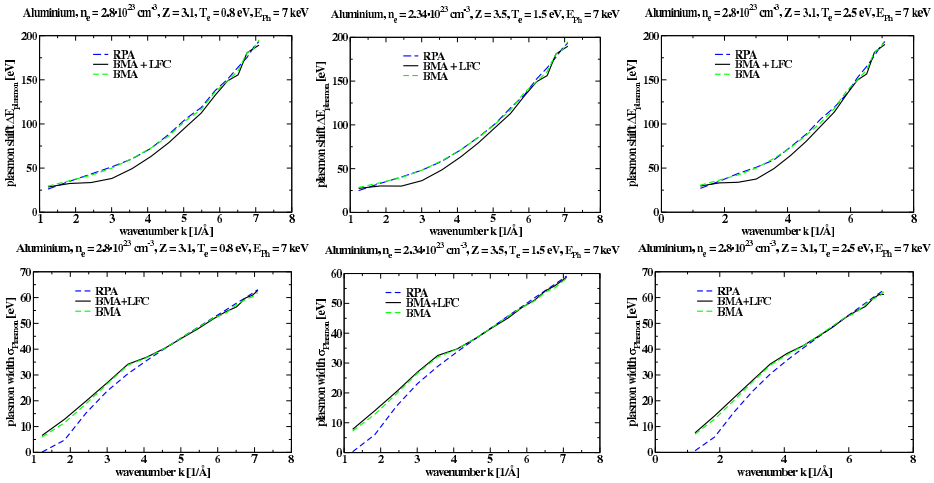

Figure 3.4: Plasmon dispersion $\Delta E_{\mathrm{plasmon}}/h = \omega$ (top row) and width (bottom row) for the proposed plasma conditions. The influence of LFC on the dispersion and of the plasma collisional damping on the width (RPA is collision-less) are obvious.

will yield an independent set of electron and/or mass density and temperature, averaged over the probed volume. Therefore, our experiment is independent of the exact predictions by hydrodynamic simulations. Importantly, we will demonstrate from VISAR data that, with our choice of ns laser focus and X-ray probe focus, the system is sufficiently homogeneous to be analysed. It has to be ensured that the anticipated target is thick enough to anneal perturbations induced by the phase plates, giving confidence in the actual states attained.

The laser compression setup will look as follows: A ns laser pulse launches a joint compression wave that propagate into a solid foil sample. The compression characteristic can span from shock compression to dynamic compression in order to assess different temperature–density regions in the EOS. At shock breakout, hydrodynamic simulations predict that the longitudinal density profile is about 30% homogeneous. The target will be coated with a CH ablator and an Al flash coating to prevent radiative preheating and flatten the shock front early on. The shock properties at the rear side are accessible by VISAR measurements. The setup is not sensitive to lateral spatial variations (imprinted by the phase plates) because it will utilize a 20 µm X-ray focus to probe on a uniform scale, but the target will not be heated by the X-rays.

For demonstration, hydrodynamics simulations have been benchmarked with previous experiments at the MEC instrument using their two ns drive laser beams. For our conditions, shock compression can reach temperatures of 1.5 eV, sufficient to melt initially crystalline targets and allow uniform plasma conditions. Concerning targets, we will concentrate on the low-Z elements aluminium and magnesium since they are

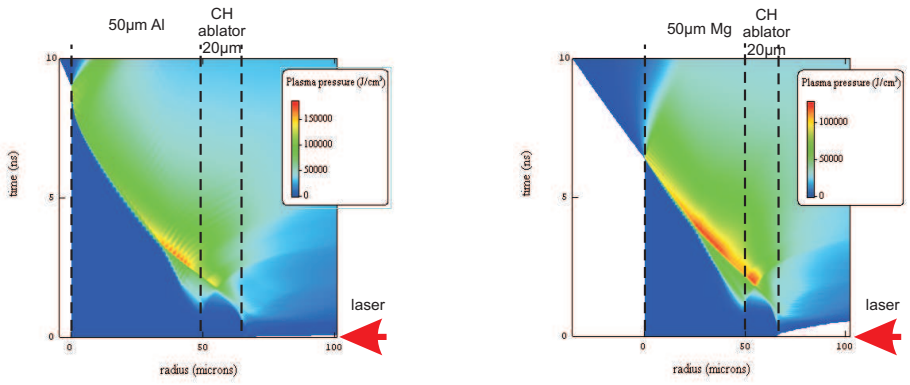

Figure 3.5: 1D hydrodynamics simulations of shock compression using the HELIOS code for aluminium (left) and magnesium (right) with 0.5 TW/cm^2 and 5 ns flat-top pulses. Shown is only the plasma pressure, which reaches 1 Mbar at shock breakout. The plasma temperature in the dense region is 0.9 eV for aluminium and 0.8 eV for magnesium.

well-studied prototypical systems (Al) and of astrophysical relevance (Mg). The wave number–resolved scattering provides the ion–ion structure factor and ion density for every single shot within the probed region.

The one-dimensional code HELIOS was employed, using the MEC laser parameters mentioned below, to investigate the conditions from shock-compressed matter in Al and Mg samples. Figure 3.5 shows the result of flat-top pulses impinging onto 50 µm metal foils (Al, Mg) coated with a thin CH ablator of 10–20 µm thickness. Laser parameters were modeled according to earlier MEC runs, which were benchmarked with VISAR campaigns. We observe that plasma pressures of 100 GPa are commonly achieved with moderate focusing: Here, a laser intensity of 5×10^{11} W/cm^2 has been assumed. The plasma temperature in the dense region is 0.9 eV for aluminium and 0.8 eV for magnesium.

Equipment needed:

- **X-ray spectrometers**
  Two crystal spectrometers with maximal efficiency at 1 eV spectral resolution. Mounted on vertical breadboard rails. Forward scattering spectrometer to cover lower possible angles to about 30° forward scattering, backward spectrometer at any angle 130–170°, not critical.

- **X-ray area detectors**
  Two ePix100 detectors for the spectrometers. Maximal number of in-vacuum gain-switching detectors (JUNGFRAU or ePix10k) to cover relevant $S(k)$ static

structure factor data, especially first and second order of ion–ion correlation peak.

- **ns drive laser**
  2ω laser with about 1–2 J/ns for ~ 5 ns, spot sizes 100 to 200 µm (with pump–probe laser). Temporal profile flat-top (high temperatures) to ramp (low temperatures). Variable electronic timing relative to X-ray pulse from -5 ns to +15 ns, maximal repetition rate is limited by ns laser cooling and target positioning.

- **VISAR**
  Yes.

- **European XFEL parameters**
  ~ 6–9 keV seeded X-rays, standard monochromator with same bandwidth to clean up seed spectrum to 1 eV bandwidth (FWHM). Maximal pulse energy and pulse length not critical. Focus 20 µm Gaussian.

- **Repetition rate**
  Up to 10 Hz, depending on target delivery and debris management.

If possible, harmonic rejection mirrors (HRM) will ensure clean XRD $S(k)$ data without third-harmonic contamination from high-order Bragg reflections.

3.6 Superionic water—a challenge

by U. Zastrau and P. Sperling

Superionic water was first studied by Cavazzoni [22] in 1999. In 2009, French, Mattsson, Nettelmann, et al. [50] presented quantum-MD simulations of water in the ultrahigh-pressure regime up to conditions typical for the deep interior of Jupiter and Saturn. In the ultradense superionic phase, characterized by mobile protons diffusing through an oxygen lattice, they found a continuous transition in the protonic structure. With rising density, the mobile protons stay with increasing probability at the octahedral sites while leaving the ice X positions unoccupied to the same degree. Water forms a fluid dense plasma at the conditions of Jupiter's core (i.e. 20 000 K, 5 TPa, and 11 g/cm^3), while it may be superionic in the core of Saturn. A substantial amount of superionic water is also expected inside Neptune.

Generating superionic water will be a challenge for dynamic laser compression. As can be seen from Figure 3.6, several Mbars of pressure have to be reached, while the temperature must stay below ~ 0.5 eV. Otherwise, the water will turn into a plasma

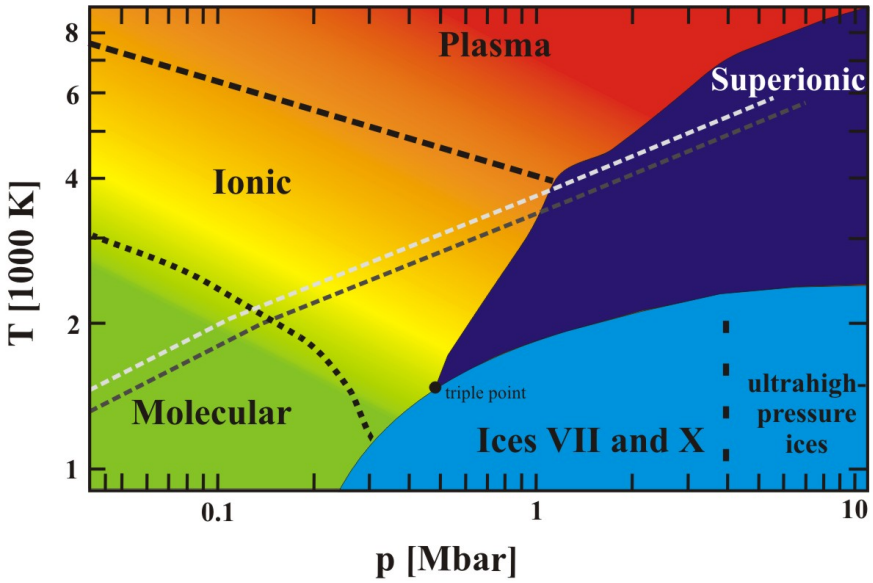

Figure 3.6: Phase diagram of water. The black and grey broken lines represent the isentropes of Neptune and Uranus, respectively. Figure reproduced from Redmer, Mattsson, Nettelmann, et al. [119].

state.

Using a liquid water sheet jet, up to 10 Hz continuous operation becomes possible. When the DiPOLE100X laser parameters (mainly the pulse shape) are controlled in a feedback loop using the laser performance operations model (LPOM) (from LLNL, see Section 4.2), VISAR online data can be used to iteratively optimize the material compression.

Equipment needed:

- **X-ray spectrometers**
  Four diced crystal analysers. These are spherically bent with 1 m bending radius and have about 30 meV spectral resolution in near-back reflection ($\sim 87°$) at about 7 keV. Mounted on the vertical breadboard rails. Three in forward scattering geometry at variable angles to observe ion-acoustic modes in collective scattering. One in backward spectrometer at any angle 130–170°, not critical, to observe symmetric broadening by Doppler motion of individual electrons.

- **X-ray area detectors**
  Two ePix100 detectors for the forward and backward analysers, close to target position. Maximal number of in-vacuum gain-switching detectors (JUNGFRAU or ePix10k) to cover relevant $S(k)$ static structure factor data, especially first and second order of ion–ion correlation peaks to determine plasma state and compression.

- **ns drive laser**
  2ω laser with optimized ramp profile (low temperatures). Variable electronic timing relative to X-ray pulse from -5 ns to +15 ns, maximal repetition rate is limited by ns laser cooling and target positioning.

- **VISAR**
  Yes.

- **European XFEL parameters**
  $\sim$ 7 keV seeded X-rays, high-resolution monochromator with few-10 meV bandwidth. Maximal pulse energy and pulse length not critical. Focus 20 µm Gaussian.

- **Repetition rate**
  Up to 10 Hz, depending on water jet stability after interaction with laser and resulting vacuum conditions.

4 Shock compression with CLF DiPOLE laser

4.1 DiPOLE100X laser setup and performance

by T. Butcher

Using funding obtained through grants from the UK's Engineering and Physical Sciences Research Council (EPSRC) and Science and Technology Facilities Council (STFC), STFC and Oxford University are providing the DiPOLE100X laser system for use at the HED instrument at European XFEL. The system has been designed and will be built and tested before shipping at STFC's Central Laser Facility (CLF), based at Rutherford Appleton Laboratory (RAL), UK. The system is similar to the DiPOLE100 system that the CLF has recently delivered to the HiLASE facility [74] in the Czech Republic, which is the first 100 J diode-pumped solid-state laser (DPSSL) system in the world. A full description can be found in [6]. Its success is based on a cryogenically cooled Yb:YAG amplifier architecture [98].

The DiPOLE100X seed source consists of an Yb-doped continuous-wave (CW) fibre oscillator generating a temperature-tunable narrow spectral linewidth (70 kHz) output centred around 1029.5 nm. An acousto-optic modulator (AOM) chops the CW output into 150 ns duration pulses at a repetition rate of 10 kHz. Following amplification, this is shaped by a dual-stage lithium niobate Mach–Zehnder electro-optic amplitude modulator (EOM), driven by an arbitrary waveform generator (AWG). The output of the seed source is a few-nJ, 2–15 ns pulse with arbitrary temporal-shaping capability. This is then fibre-coupled into an Yb:CaF_2 regenerative amplifier that reduces the repetition rate to 10 Hz and increases the pulse energy to a few mJ. A spatial-shaping stage converts the Gaussian beam to a square super-Gaussian and transports the beam to an Yb:YAG multipass amplifier, which further increases the energy to 100 mJ prior to injection into the first cryo-amplifier stage. The first Yb:YAG cryo-amplifier stage is based on the CLF's DiPOLE prototype system [5] and amplifies the pulse energy up to approximately 9 J. Within this amplifier stage, an adaptive optic (AO) is employed to ensure that the input wavefront to the final cryo-amplifier is near diffraction-limited. The final amplification stage, also based on cryogenic Yb:YAG architecture, amplifies the input pulse energy to 100 J. As in the previous stage, an AO is used to control the output wavefront.

4.1.1 System performance

Table 4.1 summarizes the main parameters, including energy, temporal, spectral, and spatial characteristics, planned for the DiPOLE100X system. More detail on specific parameters and experimental data from the HiLASE DiPOLE100 system are presented in the following sections.

4.1.1.1 Energy

Figure 4.1 shows the measured output energy from the DiPOLE100 system during commissioning experiments at RAL. The pulse used for this experimental run was a 10 ns linear ramp. In the event that a shorter pulse duration is required, the output energy will be reduced to prevent optical damage. At present, the energy at which the system has been successfully tested is 107 J for a 10 ns pulse duration with no laser-induced damage. The relationship between pulse length (t) and energy (E) in terms of laser-induced damage threshold (LIDT) is:

$$E = E_{\text{tested}}\sqrt{\frac{t}{t_{\text{tested}}}} \tag{4.1}$$

where E_{tested} and t_{tested} are the 107 J and 10 ns experimental results, respectively. From this, one can see that, for a 2 ns pulse duration, the energy should be limited to ~ 50 J.

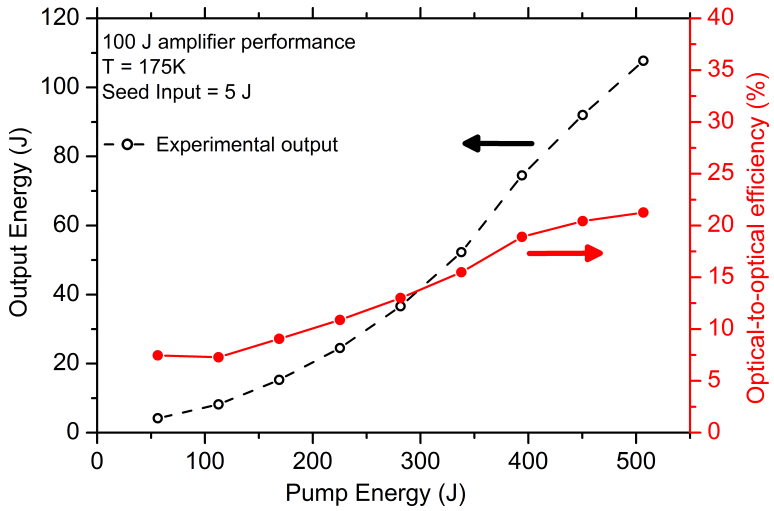

Figure 4.1: Main amplifier pulse energy and efficiency at 175 K for a pre-amplifier input energy of 5 J and a pulse duration of 10 ns at 1 Hz

Figure 4.2 shows the short-term energy stability of the DiPOLE100 system operating

Energy		
Maximum energy	100 J (@ 10 ns)	
Energy stability (shot-to-shot)	$\leq$ 5%	
Energy stability (RMS short-term)	$\leq$ 2.5%	Measured over 10 000 pulses
Energy stability (RMS long-term)	$\leq$ 5%	Measured over 4 h with temperature variations of $\pm 2^{\circ}$ C
Temporal		
Repetition rate	10, 5, 2, and 1 Hz operation	Single-shot availability during 1 Hz operation
Pulse duration	2–15 ns	Arbitrary pulse shaping (within safe operation parameters of the laser)
Temporal resolution	125 ps	Spacing between individually controllable elements of pulse shape, i.e. 80 elements for 10 ns pulse
Intensity fluctuations along pulse	$\leq$ 7.5%	
Rise/fall edges	< 200 ps	
Jitter	< 100 ps	
Pulse contrast to ASE	> 10 000	
Spectral		
Central wavelength	1029.5 nm	
Wavelength stability	$\pm$0.5 nm	
Bandwidth	70 kHz	Can be extended to $\sim$ 10 GHz using phase modulators, however this will impact on temporal intensity fluctuations
Spatial		
Output beam size	75 $\times$ 75 mm	
Beam shape	Square super-Gaussian	Order > 8
Beam quality factor M^2	3–7	
RMS modulation	< 5%	
Peak-to-valley (P-V) modulation	< 15%	
Pointing stability (shot-to-shot)	$\leq \pm$25 µrad	Measured over 1 h
Pointing stability (long-term)	$\leq \pm$40 µrad	Measured over 4 h
Wavefront quality	P-V < $\lambda/2$ and RMS < $\lambda/4$	

Table 4.1: Summary of requirements for the DiPOLE100X laser

at 107 J. The repetition rate was limited to 1 Hz during these experimental tests. This shows that an RMS stability of less than 2.5% is achievable, and it is expected that this stability will be improved further.

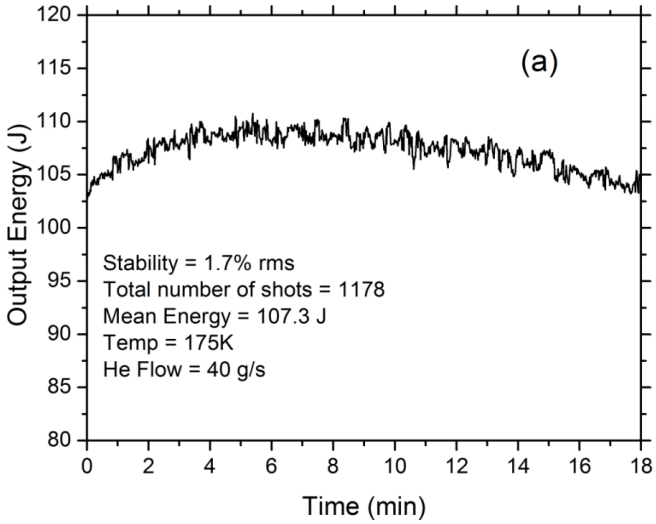

Figure 4.2: Short-term energy stability of the DiPOLE100 laser system operating at 107 J and 1 Hz

4.1.1.2 Spatial

The output beam size, at an image plane, from the DiPOLE100 system is 75 mm × 75 mm. This must be relay-imaged to the target chamber. During this beam transport, it is possible to adjust the beam size as required. The beam size was selected to maintain a maximum fluence of 2 J cm^{-2} throughout the amplifier in order to minimize the risk of laser-induced damage. Figure 4.3(a) shows the near-field (NF) profile recorded using the output diagnostics of the system. A burn pattern from the output was recorded using Kodak Linagraph1895 paper and a neutral density filter (OD = 1), placed directly in the beam. Figure 4.3(b) shows a photograph of the burn pattern captured at 107 J. The fringes seen in the camera image are not evident in the burn pattern, which suggests that the fringes are artefacts caused by either diffraction or interference effects within the diagnostic channel.

The focal spot (far-field) captured using the output diagnostics is displayed in Figure 4.4. The FWHM angular spread of the central maximum was 20 µrad (x-axis) and 17.5 µrad (y-axis), which corresponds to 1.6 and 1.4 times the diffraction limit expected for a square super-Gaussian beam, respectively. Further improvement in beam quality is expected optimizing the 100 J AO mirror parameters.

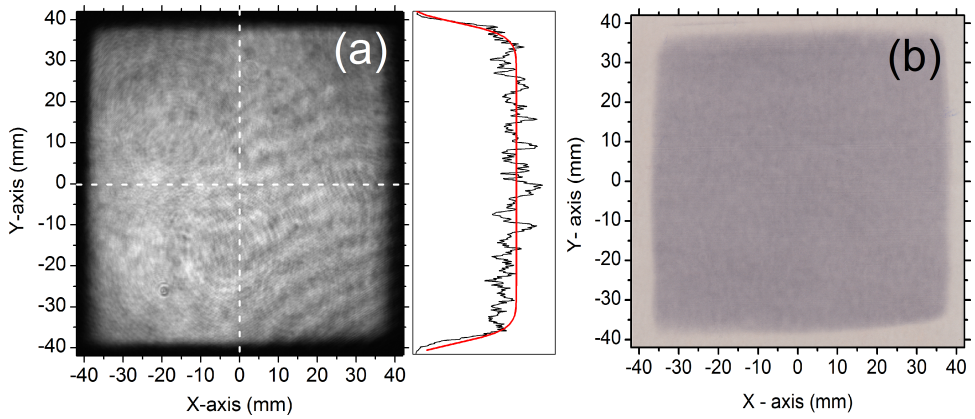

Figure 4.3: Spatial mode of the output beam taken at 107 J, on the output diagnostics (a) and on a burn paper (b). The red profile shows a super-Gaussian of order 10.

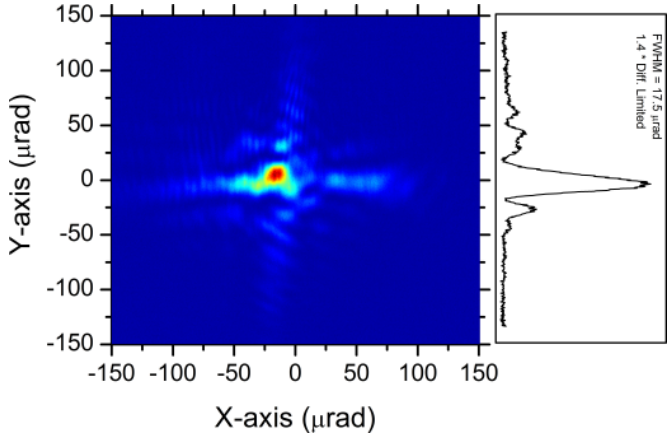

Figure 4.4: Far-field image of the output

The system was operated without active beam-pointing compensation during the beam-pointing test. The results of this run, shown in Figures 4.5 and 4.6, demonstrate that short-term beam pointing over 10 min is $< \pm 20\,\mu\text{rad}$. Application of the active beam steering system is expected to maintain this stability over longer periods.

4.1.1.3 Temporal

The temporal pulse shape for the DiPOLE100 laser is generated in the fibre-based seed source, as described in the opening paragraph of this section. This source is based on a dual-stage EOM that provides an extinction ratio of > 50 dB. The EOM is driven by a digital AWG that can generate an arbitrary waveform with a temporal resolution of 125 ps, i.e. there are 160 *temporal pixels* in a 20 ns pulse. The dynamic range of the AWG is 4096. However, in combination with the EOM, this is reduced to ~ 3700 within the current system.

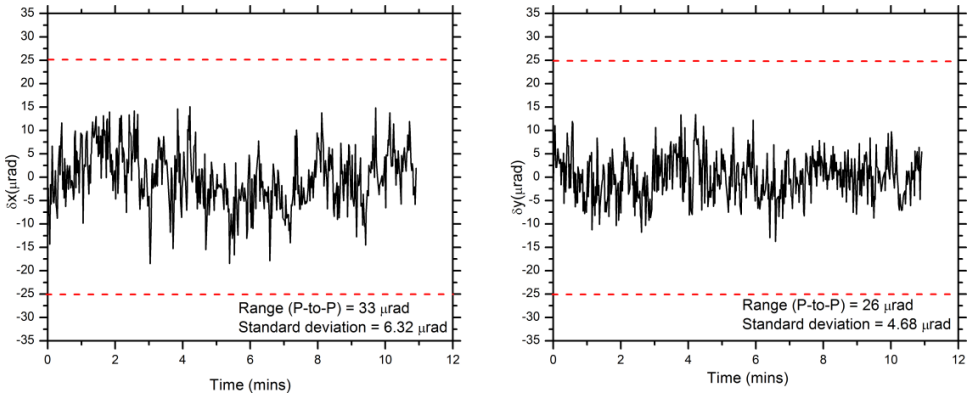

Figure 4.5: Short-term pointing stability δx and δy

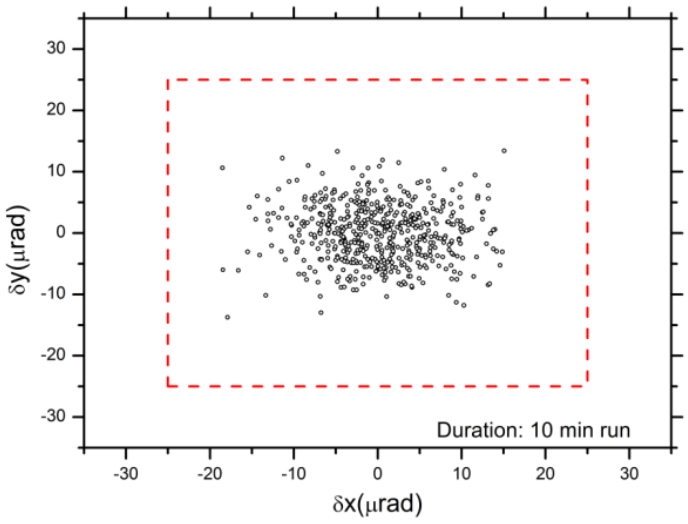

Figure 4.6: Short-term pointing stability δx against δy

Figure 4.7 shows the output pulse shape of the DiPOLE100 during the 107 J operational tests. No attempt was made to optimize the front-end pulse shape to generate a flat-top output profile during these experiments. The control system has the capability to individually address each *temporal pixel* in the pulse and adjust it in real time. It will therefore be possible, with this second-generation laser, to adjust the pulse shape during operation and hence improve the temporal profile, if required. This could be used to smooth out small intensity fluctuations, as seen in Figure 4.7, or to adjust the steepness of a ramp, for example.

CLF is developing the shaping capability further to include a closed-loop mode. The final goal of this work should allow a user to provide a desired curve for the output of the system. The software will calculate an *initial guess* for the input temporal profile,

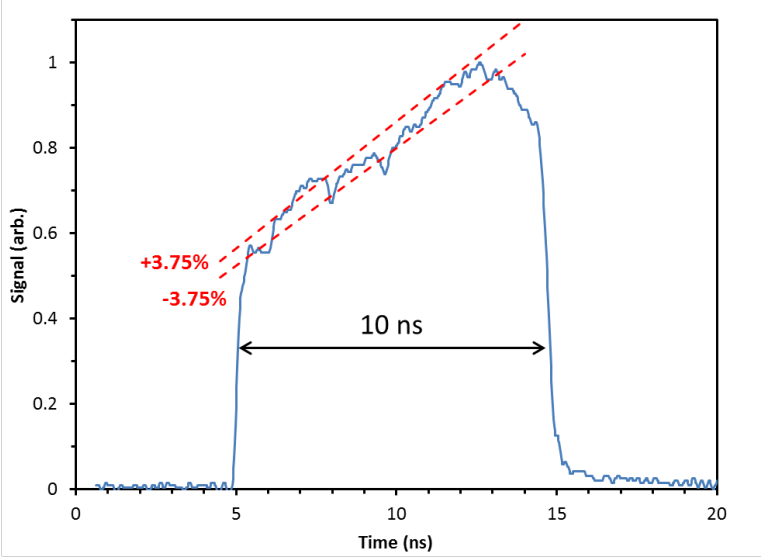

Figure 4.7: Temporal profile of 10 ns output pulse during 107 J operation

followed by a closed-loop correction of the output temporal profile until the *desired curve* is achieved. This shape can then be saved for later use. The control system will assess the input curves and apply *machine safety* limits to reduce the probability of damage to the laser.

4.1.2 Discussion

The final design of the DiPOLE100X laser system is not yet finalized. In general, the fluence on all optics will stay below 2 J/cm^2 in order not to damage any optics or gain media. The system was successfully tested at 100 J at 10 ns, but only at 50 J at 2 ns pulse duration. In a 15 ns pulse (the longest pulse possible, due to the length of the regenerative amplifier), it could potentially contain up to 120 J energy.

A good imaging plane is a plane just outside the amplifiers where the beams smooth out a bit. Which party will design and purchase the phase plates is still open—LLNL might provide these.

Currently, there is no optical isolator option at STFC; however, 2ω conversion could be one solution for optical isolation. An electro-optical switch for single pulses at 10 Hz should be an upgrade project—the current shutter can only pick single pulses with the laser system running at 1 Hz.

The best choice for frequency conversion is currently believed to be an LBO crystal of Type 1; however, obtaining it will be a challenge. SSD smoothing would require

changes in the laser chain. The DiPOLE100X system has two phase modulators at 2 and 4 GHz, respectively, but using these would result in temporal changes of up to 10%.

4.2 Dynamic compression pathways

by J. Eggert and D. Kraus

For materials experiments at the HED instrument, we estimate the pressure achievable with the DiPOLE100X laser described in Section 4.1. These rough estimates assume the diamond ablation pressure fit performed by Fratanduono, Boehly, Celliers, et al. [49] at the OMEGA laser facility (at the Laboratory for Laser Energetics (LLE) in Rochester, New York, USA) using 3ω light. Note that, for the 1ω DiPOLE100X laser, these pressures will drop by about a factor of two due to the ablation pressure wavelength scaling.

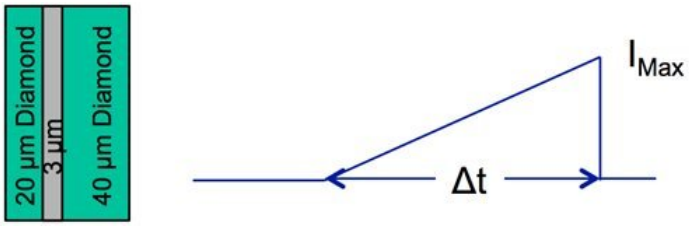

Figure 4.8: Simple pulse shape model to estimate the maximum achievable pressure for a given laser ramp compression drive

As shown in Figure 4.8, we assume a simple triangular pulse shape as a simple model; in reality, pulse shapes will require extensive hydrocode modeling. We have also assumed a simple target geometry developed for diffraction experiments at the OMEGA laser [125], using an ablator–sample–tamper geometry that allows a sample to be ramp-compressed to a high pressure and held at pressure while diffraction data is collected on a spatially and temporally uniform material state. Using this pulse shape and ablation pressure model, Figure 4.8 shows the maximum pressure reached for 5 and 10 ns long triangular pulses as a function of laser energy and laser spot radius. We see that, using the 1ω radiation from the DiPOLE100X laser, we should be able to generate planar compressions of 200 to 500 GPa (2 to 5 Mbar) for a 5 ns triangular drive, depending on the desired width of the planar region.

Laser pulse shapes can be designed to drive steady shocks in materials, allowing the use of a thicker sample and the elimination of the tamper in the target shown in Figure 4.8 [150]. However, compression pathways, such as those shown in Figure 4.10, that require a portion of the sample to be ramp-compressed need careful

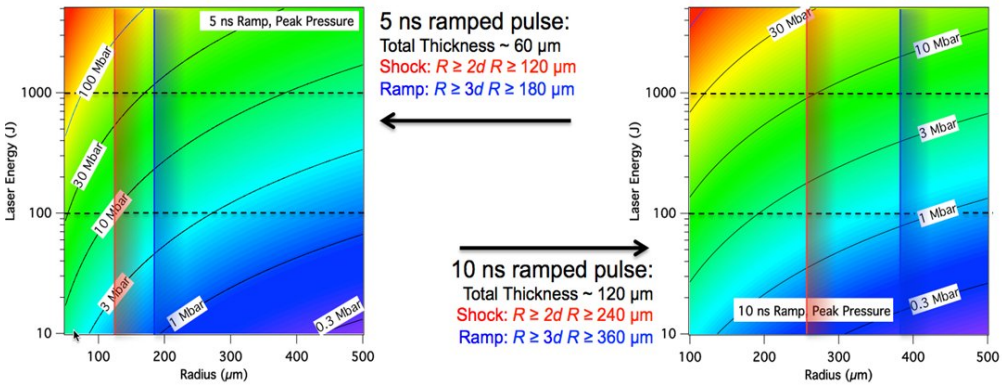

Figure 4.9: Maximum pressure achieved for ramp compression from the simple triangular laser pulse shown in Figure 4.8. Thickness is determined by the need to avoid shock formation within the diamond. The radii shown as red and blue lines show the needed spot size for the 0d and 2d planar region, respectively, at the tamper-free surface, assuming edge rarefactions intrude at an effective angle of 63°, in oder to compensate for effects discussed in [151]. These calculations assume 3ω laser light. For the 1ω DiPOLE100X laser, these pressures will drop by about a factor of two due to the ablation pressure wavelength scaling. Thus, for the HED instrument's DiPOLE100X, we can expect to achieve uniform pressures of 2 to 5 Mbar with a 5 ns pulse.

analysis using hydrocodes to determine the optimum laser pulse shapes.

Several experiments (a, b, and c) are proposed in Figure 4.10 and described in the following:

(a) Ramp compression through a solid–solid phase transition
Determination of the stress at which solid–solid phase transition occurs under ramp compression. This experiment requires the creation of a uniform P, V, T state everywhere within the sample at a variety of pressures. This type of experiment in now standard at the OMEGA and NIF lasers.

(b) Shock ramp or double shock compression and release through phase transition
The temperature of the sample can be raised with a small shock to the solid state followed by ramp compression to map out the dynamic phase diagram of materials. This pathway also shows a proposed experiment where the phase transition is studied under controlled release as well as compression. Measurement of such a hysteresis loop is the best way known at this point to attempt to gain an estimate of the equilibrium transition pressure. Comparison of such hysteresis loops under dynamic compression with similar loops studied under static

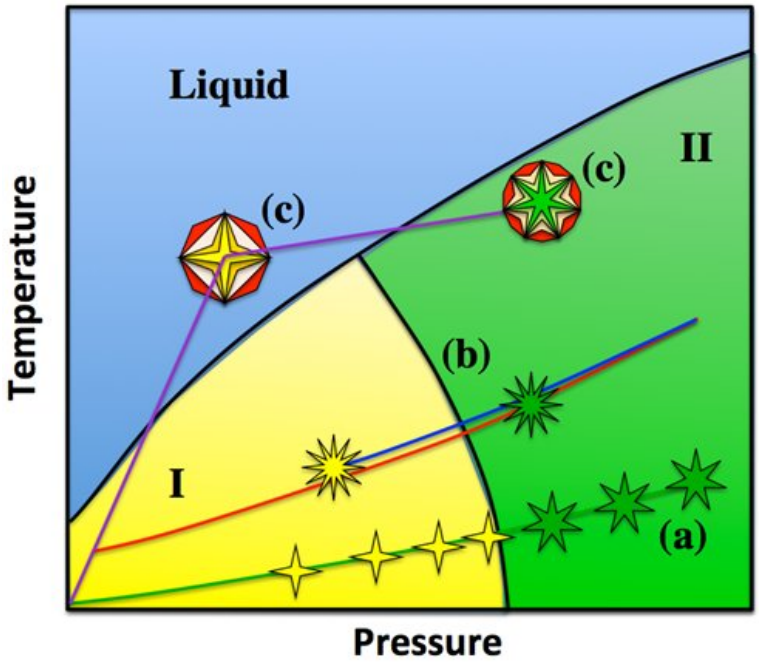

Figure 4.10: Various compression pathways through phase space. a) Ramp compression through a solid–solid phase transition. b) Shock ramp or double shock compression and release through a phase transition. c) Shock–melt–resolidification.

conditions offer an effective method to constrain the kinetics of a phase transition.

(c) Shock–melt–resolidification

It is also possible to shock any material into the liquid phase, which can be easily determined by diffraction. As long as the P, T state of the material can be determined accurately, excellent data concerning the dynamic melt line can be collected. Accurate liquid diffraction data can be analysed to extract accurate liquid density [40]. If the material state is sufficiently well defined and the data collected is of sufficiently high quality that accurate diffraction can be obtained from both the liquid and solid phases in equilibrium, then the volume discontinuity, the Clapeyron slope, and the latent heat will all be accessible experimentally. Finally, careful experimental design allows experiments involving shock melting and ramp resolidification to examine the melt line of materials at even higher pressures. Such experiments are currently being demonstrated on iron at the NIF laser [69].

For all of these proposed pathways and experiments, it is critical that a uniform material P, V, T state be obtained throughout the sample at the time of the X-ray pulse. In well-designed experiments, pressure can be accurately determined using VISAR, but careful experimental studies of sample heating due to radiation from the

ablation plasma and the European XFEL beam itself will need to be performed at the HED instrument before quantitative data and conclusions can be justified. It is important that hydrocode simulations be used only as a tool for experimental design, but that material state and properties be determined experimentally as much as possible. It should be a major goal of the HED instrument to eliminate hydrocode simulation from data analysis as much as possible.

4.3 Ramp compression and pulse shaping

by D. Kraus

Ramp compression can produce high pressures but lower temperatures than are achievable with shock compression. Shock states lie on the Hugoniot; ramp compression produces states that are off the Hugoniot. Ramp compression relies on coalescence of sound waves; initial conditions and more parameters must be measured compared to shock experiments. Ramp compression without forming unwanted shocks is particularly challenging for materials with very low sound velocities and those with sudden changes in sound velocity with pressure [151].

Ramp compression requires very reliable drive pulse shapes. For example, pulse shaping with a step profile could be achieved with two stacked pulses or with the shaping of a single pulse. Proper ramp compression requires the temporal shape of the desired pulse to be stable within a few per cent (%) or even better. Due to the low velocity of the initial sound or shock wave, typical ramp pulses are of relatively long duration and thus the stability requirement should particularly be fulfilled for pulses of 10 ns duration or longer. Pulse shaping on the fly with replenishing targets would be ideal for optimizing the experimental conditions. This could be a closed-loop system, or one could start with a best guess of 10 pulse shapes, apply those in a few minutes, subsequently analyse the result, and choose the best path to move forward.

At the HED instrument at the European XFEL, it is recommended that a number of flat-top pulses with lengths between 2 and 15 ns that result in steady shocks be saved in a database. We should also monitor each laser pulse with a fast digitizer and automatically save it in the European XFEL control and analysis software framework, Karabo (see Section 9.1). For a ramp, the pulse shape should be tunable using VISAR feedback. Depending on the science case, suitable pulse shapes can be very complex. Only qualified operators will be allowed to change pulse shapes, and the HIBEF UC will provide operation staff of a minimum of six people.

4.4 Frequency doubling

by R. Cauble

The DiPOLE100X long-pulse laser operates at a wavelength of 1029.5 nm (infrared), referred to as 1ω, similar to extant long-pulse glass lasers, which are generally operating at about 1053 nm. 1ω operation is sufficient for experiments where the primary long-pulse requirement is maximum energy. One such purpose might be to produce an intense, long-lived X-ray pulse as a probe, or a large plasma volume that itself can be examined or probed. However, the primary use of the DiPOLE100X laser at the European XFEL is to drive specified loading profiles in targets. The loading profile—e.g. a simple shock, a double or multiple shock, or a ramp with steadily increasing pressure—is dictated by the requested laser temporal pulse shape (see Section 4.2).

In these cases, the drive laser—DiPOLE100X—is in operation for several ns. The leading part of the few-ns laser pulse will ablate the target surface and produce a plasma; the trailing part of the pulse will interact with that plasma, not with the solid target. The single-wavelength laser may non-linearly interact with the charged particles in the plasma, resulting in the laser light being strongly scattered from the plasma. This is the field of laser–plasma interactions (LPIs). LPI can result in a loss of drive energy (and thus pressure). It also results in a fraction of the plasma electrons being accelerated to high energy, so-called *hot electrons*. These hot electrons can penetrate the target ahead of the pressure wave, irreproducibly heating and otherwise modifying the target, leading to experimental errors that are difficult to quantify.

It has long been known that the shorter the laser wavelength, the less intense this non-linear coupling. Experience has shown that a laser wavelength of about 1000 nm is too long; the resulting LPI leads to preheated targets and unsteady pressure waves. The usual practice is to change the wavelength by producing a harmonic, typically the second one by frequency doubling (2ω) or even the third by frequency tripling (3ω). Frequency doubling an intense infrared laser into the visible is sufficient to offset most deleterious LPI effects. There is an energy cost in conversion, which is higher for 3ω than for 2ω. Conversion to 3ω has been found to be necessary for some inertial confinement fusion experiments, but is not considered necessary for applications at the HED beamline. Frequency doubling is sufficient.

The harmonic is produced by relaying the laser beam through a thin crystal—potassium dihydrogen phosphate (KDP) is a common crystal. The 1ω laser

light reacts non-linearly with the crystal, producing a 2ω beam. Other than crystal quality, harmonic production is governed by the crystal lattice arrangement and thus geometry. Laser energy is lost in conversion from 1ω to 2ω; efficiencies can be 50–70% for high-quality crystals.

Frequency doubling can be accomplished simply by inserting the crystal in the 1ω laser beamline with minimal optics. It is not yet known what the effects of a high repetition rate are on the crystal, although they are expected to be manageable.

The community also stated that frequency tripling is only necessary for hohlraum physics because of the amount of dense gas and ablated material in this geometry. In our case, frequency doubling for planar geometries should be sufficient. It should be noted that active cooling will likely be necessary during frequency doubling at 10 Hz, as well as dumping of residual 1ω energy.

4.5 Timing and jitter between long-pulse laser and X-ray laser

by Z. Konôpková and G. Priebe

One important aspect of the timing system is the distribution of clocks and event triggers, which allows numerous subsystems within the European XFEL to work synchronously with respect to the electron bunches or photon pulses. A 1.3 GHz reference clock was chosen as the time standard at the European XFEL facility. This reference clock, as well as various derived lower frequencies and event trigger signals, are distributed within the facility (see Ref. [115] for more details).

The European XFEL timing system will be used for the synchronization of the spectrally and temporally controlled laser pulses of the DiPOLE100X laser [5]. The laser system starts with an Yb-doped CW fibre oscillator, which is chopped by an AOM into 100–150 ns flat-top pulses at a repetition rate of 10 kHz, further amplified in a multistage fibre amplifier, and finally an EOM controlled by an AWG shapes the output pulses to the desired temporal profile. The output from the fibre frontend seeds a Yb:CaF_2 regenerative amplifier. A Pockels cell within the amplifier is used to select a pulse from the 10 kHz seed train at 10 Hz, or lower. The output is passed on into the multipass booster amplifier and the final multislab cryogenic gas cooled amplifier.

The 10 kHz event trigger for the AOM will be delivered with an accuracy of ~ 20 ps. All other event triggers used in the laser system will be generated by an interior timing system using the 81.25 MHz clock provided by the European XFEL timing system. For a shot on demand, a laser shutter capable of switching in less than 100 ms is employed.

5 Optical shock diagnostics

5.1 VISAR and SOP setup at HED

by E. Brambrink and Z. Konôpková

5.1.1 Sample characterization with VISAR

Laser-driven shocks and ramp compression require a dedicated diagnostic to determine the fundamental thermodynamic parameters: pressure, density, and temperature. In the last few decades, the combination of a velocity interferometer system for any reflector (VISAR) [23, 7] and a streaked optical pyrometer (SOP) has become a standard diagnostic for these parameters, especially on high-energy laser systems [141, 73, 10, 77]. The VISAR and SOP installation at the HED instrument will allow users to control the hydrodynamic parameters of compressed matter probed by the European XFEL. In addition, it allows results to be compared directly with numerous experiments done at high-energy laser facilities.

An important point of VISAR and SOP is the ability to measure the spatial and temporal evolution of hydrodynamic parameters. This ability enables the compression history of the complete sample to be measured in a single shot, while the X-ray diagnostics provided by the European XFEL measure a single point in time and space and thus require scanning in space and time. Thus, VISAR and SOP are indispensable to control the spatial homogeneity and the reproducibility of the compression, which is fundamental for interpreting results from repetitive experiments.

Pressure and density in a shock can be deduced from the shock velocity c_s and particle velocity u_p using the Rankine–Hugoniot equations. In the case of ramp compression, the same is possible by measuring the sound speed and particle velocity assuming an isentropic compression. Sound/shock speeds and particle velocities for pressures available with the DiPOLE100X laser at HED will be in the range of a few 100 m/s up to 15 km/s. The transient character and the small size of laser-driven compression samples require temporal resolutions up to 10 ps and spatial resolutions around 10 µm.

A VISAR measures the velocity of a reflecting surface. Depending on the type of sample, a VISAR can measure either particle velocity, shock (sound) speed, or both.

Depending on the pressure range and sample, the VISAR can measure the free surface velocity of a reflecting sample, the interface velocity between a reflecting sample, or the shock speed of a reflecting moving shock front. It can also measure the transit time through a layer, which can be related to an average shock speed.

The VISAR also measures the intensity of the reflected light. With proper calibration, this can be used to measure the absolute reflectivity of the sample at a single wavelength. This is of particular interest for the SOP measurement, as relating the measured emission to a temperature requires knowing the reflectivity.

The SOP collects the visible light emitted by the sample in a known spectral range. Assuming a grey body, this emission can be related to a temperature if the reflectivity is known or measured. As for the VISAR, the SOP can also measure average shock speeds, as the emission changes at each interface of a layered sample.

These techniques are well established in the shock physics community and widely used. They allow, in combination with hydrodynamic simulations, the determination of the pressure and density conditions in the compressed sample probed by the X-ray FEL.

5.1.2 VISAR working principle

A VISAR is based on an interferometer, where one arm exhibits a temporal delay compared to the other. Thus, it superposes the phase $\phi(t)$ and $\phi(t + \Delta t)$, which is directly related to the velocity of the reflecting surface. The delay is normally introduced by displacing the mirror in the arm and adding a glass block (etalon) to compensate for the beam shift. A VISAR needs a light source with a coherence length longer than the delay introduced in the delayed arm and a detector with a temporal resolution high enough to resolve the observed phenomena.

For the HED instrument, a so-called line VISAR is planned, which will allow a velocity profile along a straight line across the sample to be measured. The detector is a streak camera, offering 1D spatial and temporal resolution. The raw data output of the streak camera is an image of the temporal evolution of the fringe shift, like the one shown in Figure 5.1, which is directly related to the phase shift. The velocity can be calculated from the phase shift using the formula:

$$v(t) = \frac{\lambda}{2\tau(1+\delta)} \times \phi(t) \tag{5.1}$$

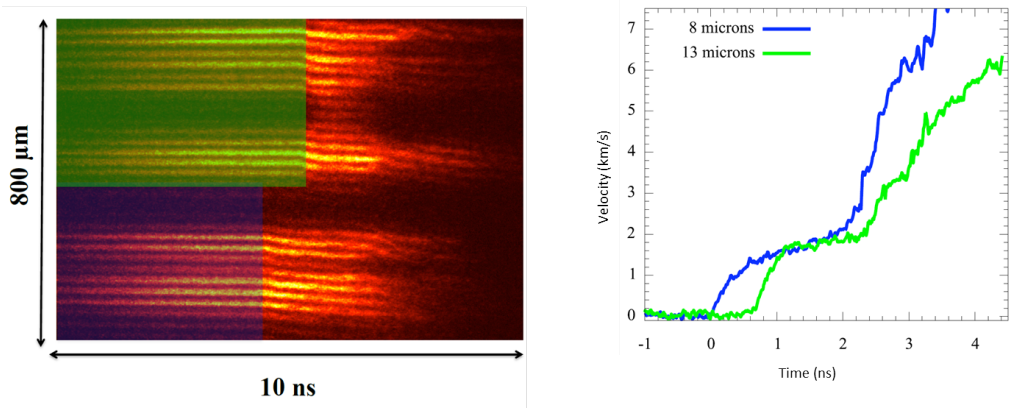

Figure 5.1: *Left:* Raw data of a line VISAR for the free surface velocity of a step target. *Right:* Extracted velocities.

where λ is the wavelength of the probe laser, τ the temporal delay between the arms, and $\delta = \frac{n_0}{n_0^2-1}\lambda\frac{dn}{d\lambda}$ a correction for the Doppler-shift-induced change of the refractive index of the etalon. In the case of a discontinuity (shock), the phase jump is unknown by $n \times 2\pi$, as a shift of one fringe leads to the same fringe pattern. To overcome this ambiguity, two VISARs with different delays between the arms are used in parallel.

5.1.3 SOP working principle

The SOP consists of a streak camera and an optical system, which images the sample to the entrance of the streak camera. For determining the intensity, the solid angle, magnification, and spectral transmission of the imaging system must be characterized. It is also important to filter out possible other light sources such as the drive laser or the probe laser, which is typically done with an interference filter. A cross calibration with a known temperature standard is necessary to verify the performance of the system.

5.1.4 Implementation at HED

The current proposal is that the VISAR system will be implemented on an optical table close to the interaction area IA1, together with the SOP. We will use two floors of a 2.4 m $\times$ 0.8 m optical table stacked one above the other. The upper floor will be occupied by the VISAR system, while the lower floor is reserved for the SOP and beam transport. A layout of the table is given in Figure 5.2.

The tables should be vibration-decoupled and damped, as stability is crucial for the

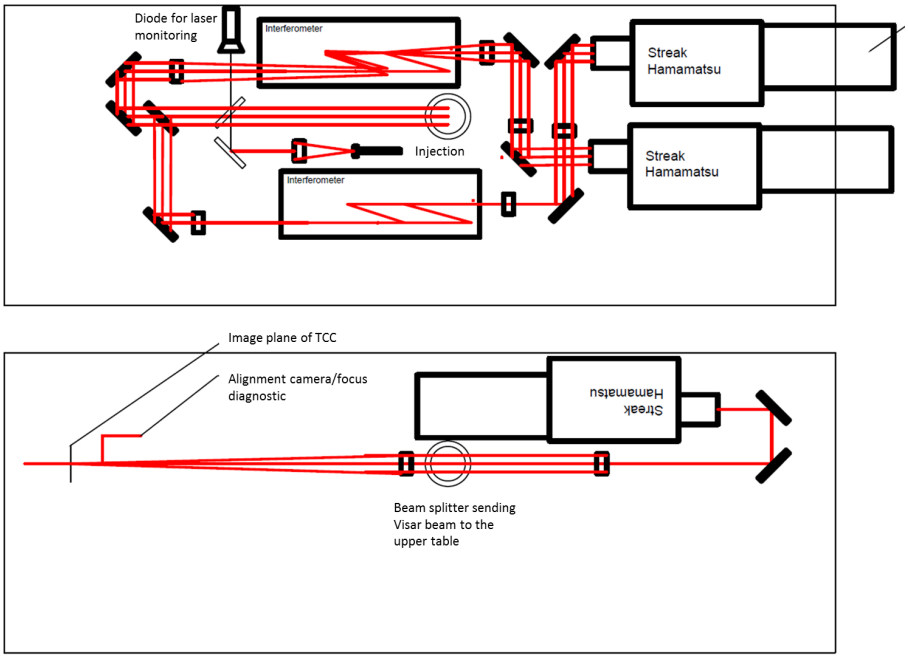

Figure 5.2: Preliminary layout of the VISAR table and the SOP table. The size of the table in the drawing is 2.4 m $\times$ 0.9 m.

interferometers.

5.1.4.1 Probe laser

As mentioned above, the probe laser must have a coherence length greater than the delay between the two interferometer arms. Ideally, the coherence length is as long as the laser pulse (longitudinal mono-mode laser / injected cavity). The pulse length of the probe laser defines the maximum observation time of the system and should be longer than the drive laser. In the HED case, this requires a 30 ns laser pulse. A frequency-doubled Nd:YAG laser at a wavelength of 532 nm is recommended, as it is a standard laser system that fits the sensitivity of the proposed streak camera well. The required pulse energy is 5 mJ. The laser will be injected into a fibre of 1 mm core diameter and then transported to the VISAR table. Such a transport over 50 m is possible without significant loss of energy. On the VISAR table, a beam monitoring system will measure the laser power, which is necessary for measuring the reflectivity.

5.1.4.2 Interferometers

A Mach–Zehnder interferometer is used for each VISAR. Figure 5.3 shows the schematic including the etalon for the delay of one arm. The mirror displacement of M2 must be motorized with µm precision. Depending on the etalon used, a displacement of up to 35 mm is necessary. M1 and BS2 are used during the experiment to change the interfringe distance and the fringe contrast. Both optics should be motorized.

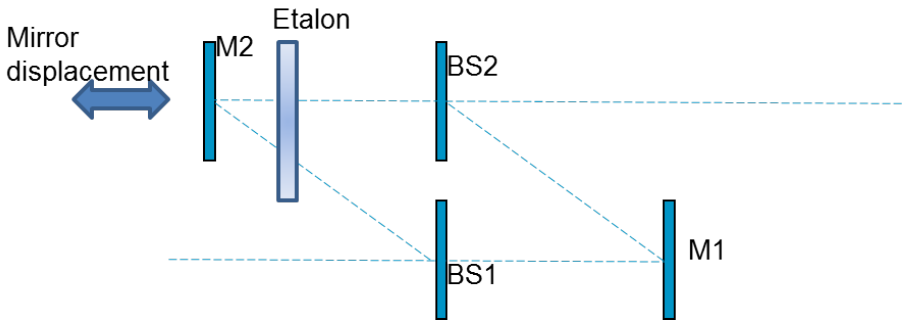

Figure 5.3: Schematic of the interferometers used in the VISAR (M = mirror, BS = beam splitter)

The thickness of the etalon varies from 100 to 2 mm, which corresponds to sensitivities of 0.5 and 25 km/s/fringe.

5.1.4.3 Beam transport and optical system

The optical system is based on three image planes conjugated to the target plane: a first image plane on the SOP table for alignment and target verification, a second on the beam splitter in the interferometer, and a third on the streak camera. The magnification between these three image planes is low, between 1 and 2. The beam transport between these three image planes remains unchanged. The imaging system from the target to the first plane on the SOP table depends on the experiment chamber, the irradiation geometry, and the required field of view / spatial resolution. Magnifications between 10 and 20 with $f/4$–$f/2$ optics are typically used in laser facilities.

5.1.4.4 Detector

A streak camera with a S20 photocathode will be used for each VISAR arm and the SOP. A S20 cathode is preferred due to its high sensitivity for visible light. The best

temporal resolution should be 10 ps and the longest time window at least 25 ns. A narrow band pass filter (1 nm width) blocks scattered light from the drive laser for the VISAR. In the case of the SOP, a combination of interference filters and notch filters will remove light from both drive and VISAR laser. The spectral range has to be adapted for the sample type and pressure range.

5.1.5 Discussion

During the workshop in September 2016, the user community recommended that VISAR and SOP could be combined, but this is not a requirement. There is also a pyrometer planned by a German Federal Ministry of Education and Research (BMBF) project (Winkler et al., Goethe University Frankfurt, Germany, in collaboration with GSI Helmholtzzentrum für Schwerionenforschung in Darmstadt, Germany). The current design has two levels, SOP below and VISAR on top. The VISAR laser could be placed 15–20 m away and be fibre-coupled to the VISAR table. The VISAR itself should be enclosed to protect it from TW-laser electromagnetic pulses (EMPs) and for temporal stabilization of the Mach–Zehnder interferometers. In the experiment hutch, the VISAR could sit elsewhere (not necessarily next to the target chamber), with a periscope steering the beam up. This beam transport could be in air. A constraint is that easy access for alignment and etalon change on the VISAR breadboard needs to be ensured. A 1ω option for the VISAR (using the non-frequency-doubled VISAR laser) sometimes gives better reflectivity where green light would not nicely reflect. Also, the HED group should consider other streak cameras—Hamamatsu e.g. has a good dynamic range; other streak cameras may have a better streak tube design that can offer good time resolution without narrow entrance slit.

5.2 Experience from VISAR analysis at MEC at LCLS

5.2.1 Shot-to-shot repetition rate and thermal lensing effects

by L. Fletcher

5.2.1.1 Introduction

The MEC instrument at LCLS provides a range of laser capabilities through two distinct laser systems: a 30 J, 527 nm, ns-system and a 1 J, 800 nm, fs-system [55]. Most of the experiments that require high-energy drivers are typically performed using the 30 J ns-laser. Such a system will deposit a significant amount of thermal

energy into the optical components, thus requiring a delay between shots. Due to the economic and scientific value of X-ray beam time at LCLS, considerable efforts have been invested into quantifying the minimum time between pulses that can be delivered on a target without thermal instabilities affecting the optimal spatial and temporal behaviour of the laser system [106]. The current specifications relating to the cooldown time of the large-diameter glass amplifiers have been determined to be ~ 7 min (3.5 min for one beam interleaved). Recent experiments using a VISAR (see Section 5.1) as a diagnostic platform to characterize the on-target shock properties have demonstrated prefocusing, as a result of thermal lensing, for pulse repetition rates of 7 min/shot. Furthermore, thermal accumulation is likely to persist well beyond a 7 min interval. The study presented in this report suggests that an adequate repetition rate, to minimize heat accumulation and reduce the possible effects of thermal lensing, should be at least 10 min/shot.

5.2.1.2 Thermal lensing

When optical elements are used to transmit or reflect high-power laser radiation, there will be some localized increment of heat absorbed that will alter the refractive index and shape of the optical elements. As the absorption of heat changes, so will the focal point and the spot size [8]. When inadequate water or air cooling is supplied to the optical system for a specified shot-to-shot rate, or if the shot-to-shot rate is too fast to fully allow thermal dissipation, a temperature gradient will build up on the optical components. The induced temperature gradient can change the material's refractive index (dn/dT) as well as slightly alter the expansion dl of the optics with temperature (dl$/dT$), resulting in thermal lensing. The focal length shift for a thin lens is given approximately by the quasi-statistical formula [101]:

$$-\Delta f = \left(\frac{2APf^2}{\pi j D_{\mathrm{L}}^2} \right) \frac{dn}{dT} \tag{5.2}$$

where Δf is the change in focal length (%), A is the absorptivity of the lens material (m^{-1}), P is the power incident on the lens (W), n is the refractive index of the lens material (dimensionless), k is the thermal conductivity of the lens (W/mK), D_{L} is the incident beam diameter on the lens (m), and T is the temperature (K). While thermal lensing is typically discussed in the context of heating within a gain medium, the basic principle applies to all transmitting optical components where heat effects are allowed to accumulate.

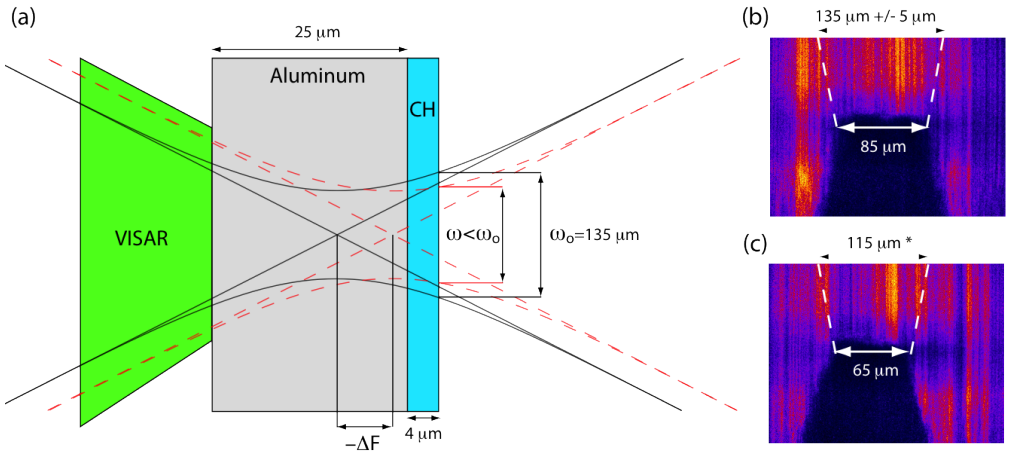

Figure 5.4: (a) Experimental configuration demonstrating the effect of thermal lensing on the spot size of the irradiated region. (b) VISAR streak images of the shock breakout for the first shot of the experiment. (c) VISAR streak images of the shock breakout for shot Number 13 of the experiment using a repetition rate of 7 min/shot. The dashed lines illustrate lateral edge effects from the laser spot consistent with a release angle of $\Phi \sim 45°$.

5.2.1.3 Experiment

Gaussian beams allow for a sensitive measurement of thermal lensing, as slight deviations in the focus position will have a significant affect on the laser spot size due to the relatively small Rayleigh range along the optical axis. Additionally, using a VISAR as a diagnostic to measure the on-target conditions (via spatially resolved breakout conditions) will allow for a precise method to monitor the shot-to-shot changes in the laser focus. The setup for this study can be seen in Figure 5.4. The targets consisted of 25 µm thick aluminium foils with 4 µm thick CH ablators. The targets were irradiated with a 135 µm unfocused Gaussian beam delivering 3 J of energy over a 3 ns time duration. The focusing conditions for the experiment are shown in Figure 5.5. The energy delivered per pulse was regulated by a waveplate placed before the final focusing optic. Because this study was only interested in resolving the shock velocity and the planarity of the shock at the rear surface of the target, the VISAR system was set up without etalons in order to increase the spatial and temporal resolution of the shock at the breakout.

A comparison between Figures 5.4(b) and 5.4(c) shows a 20 µm decrease in the planar diameter (at the breakout of the rear surface) of the shock after a 13 shot period (7 min/shot). The initial decrease of approximately 50 µm in the size of the shock as it transits the sample is consistent with the expected shock erosion due to side waves originating from the edge of the spot (assuming $\Phi = 45°$ release angle) [151]. Using the geometric dependence of the fields of a Gaussian beam for

a given wavelength λ along the optical axis (Figure 5.5), it is possible to calculate a reduction in the initial spot from 135 µm to 115 µm after 13 successive shots on target, assuming the same-side release wave behaviour between samples is similar for every target. The results from Figure 5.6 demonstrate a systematic decrease in the focal spot size as a function of shot number. At a constant shot repetition rate of 7 min/shot, the spot size at the shock breakout reduces in diameter to approximately 0.75% of the spot size of the first shot after 1.5 h of operation.

After a 30 min cooldown period, the measurements were continued, resulting in a return to the initial shock conditions. Increasing the shot repetition rate to 10 min/shot results in a constant breakout diameter suggesting a stable laser system devoid of thermal lensing. The results show that a shot-to-shot measurement may not be enough to monitor focal changes, as the planarity region for each successive shot is within the measuring error, but the accumulation of shots over a 1 h period and a 30 min period demonstrates a decrease in the spot size.

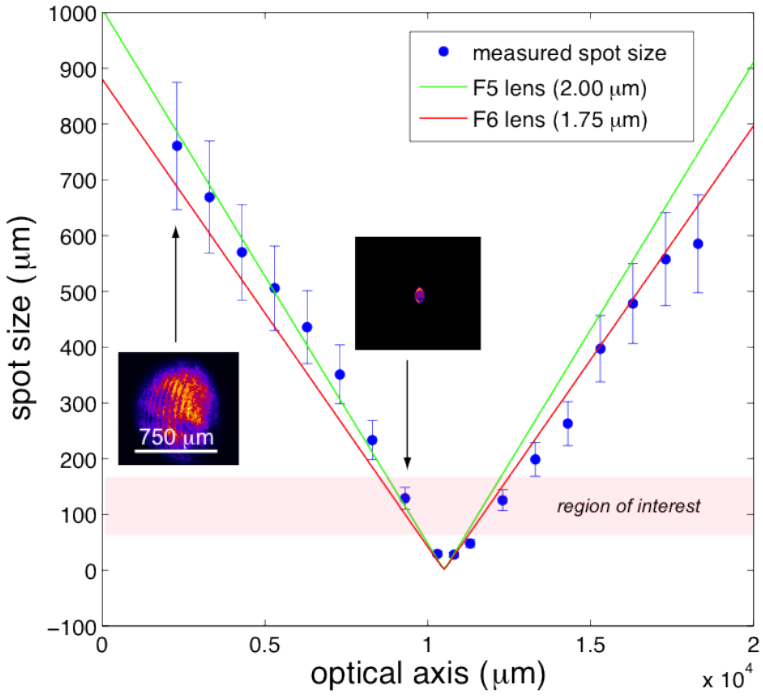

Figure 5.5: Measurements of the average spot size diameter at the target chamber centre as a function of focal distance along the optical axis. Solid lines: theoretical calculations of the beam waist using the geometric dependence of the fields of a Gaussian beam calculated with an *f*/5 and *f*/6 lens.

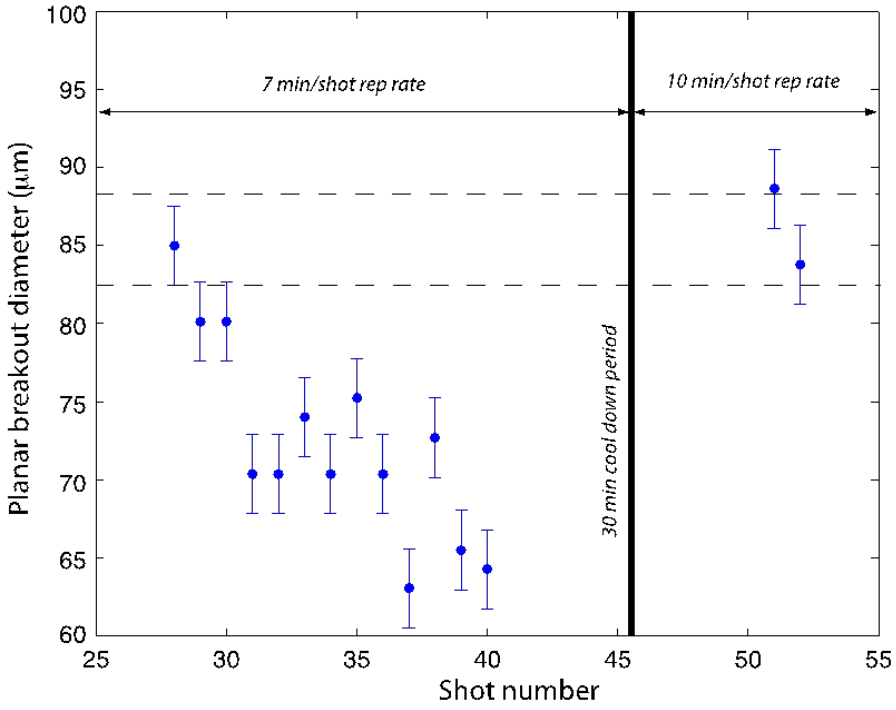

Figure 5.6: Planar-region diameter at shock breakout measured from VISAR images as a function of shot number. The measurements are made for two shot-to-shot repetition rates of 7 min/shot and 10 min/shot with a 30 min cooldown period separating the two shot series. Dashed line: mean diameter +/- the standard deviation of the first and last two shots of the experiment.

5.2.1.4 Summary

A reduction in the focal spot diameter of 20 µm would require a change in the focal distance, given by Figure 5.5, of 200 µm. A focal change of 200 µm is likely caused by the cumulative thermal effects of the optical components in the ns-laser system, as the amount of heat absorption in one optic (assuming fused silica glass) of 10 mm thickness would be above the melting temperature. Such a temperature can be calculated from geometrical expansion considerations and the simple lens formula for the focal length change. Many experiments at MEC use hybrid phase plates for driving shocks into samples. The beams are typically focused with 250 mm focal-length singlet lenses (5 mm unfocused beam) and hybrid phase plates for focal spots of 100 µm, 150 µm, 250 µm, and 500 µm. Phase plates are the preferred method for planar shock formation and will have a significantly larger Rayleigh range than unfocused Gaussian beams.

It should be noted that this report has not measured the effect that thermal lensing has on the spot characteristics when using phase plates, as a 200 µm focal change

could be minimal. While such a configuration is not as sensitive for exacting focusing conditions, the spatial profile of the shock and the intensity fluctuations in the focal area can be highly susceptible to the numerical aperture of the optical system. Here, we show that VISAR together with Gaussian beam focusing allows one the opportunity to minimize thermal lensing and optimize the performance of a high-energy laser system. Incorporating a feedback shock monitor (such as a VISAR or an equivalent plane imaging diagnostic) can be used as a novel method to minimize thermal instabilities within such a laser system.

5.2.2 Lessons learned from MEC and OMEGA

by R. Smith

Pressure determination by VISAR bears some challenges due to changes/loss of reflectivity, and different results are obtained when working with or without LiF window. Results from samples with LiF windows are preferred.

At the OMEGA laser (LLE), the best pulse shape for producing a steady shock (constant pressure drive) has been found to be a square pulse with slightly rising top, somewhat similar to the pulse shape shown in Figure 4.7. As a result of the laser–plasma interactions discussed in Section 4.4, the intensity of the drive laser needs to increase at later times in the laser pulse in order to produce a steady shock because of the plasma expansion. Producing and maintaining a steady shock was very sensitive to the pulse shape.

At the MEC instrument (LCLS), the delivered flat-top pulse has, in general, not been satisfactory and has varied a lot in both intensity and profile. These variations are very apparent in the measured VISAR data.

A laser intensity vs. pressure relationship (using a CH ablator) has been compiled for MEC and OMEGA. In general, there is a dependence on ablator material and laser wavelength.

The value for the rarefaction wave angle inside the target is not well established, but could be up to 60°. This imposes limitations on small spot sizes in combination with thick targets. At MEC, Gaussian defocused spots without a phase plate fluctuated and were non-symmetric. These variations were reflected in the VISAR signal, showing different velocities at different areas of the spot. With phase plates, there is more stability but a high-frequency spikiness. In general, the phase plates in use at MEC are too large in diameter for their laser diameter, and only a few elements are

illuminated.

An increase in ablator thickness smoothens out inhomogeneities. However, too-thick targets are not possible due to release waves coming in. In some targets with an Al flash coating between target and LiF window, the VISAR shows the X-ray FEL impact due to loss of reflectivity, which is a handy diagnostic for spatial and temporal overlap.

At MEC, Gaussian defocused laser drive spots obtained without a phase plate have large intensity fluctuations and were non-symmetric. These variations were clearly reflected in the VISAR signal, which showed different velocities at different areas of the drive spot. With phase plates, there is much more stability but a high-frequency spikiness—with one spike in the exact centre of the focal spot! In general, the phase plates in use at MEC are too large in diameter for the laser diameter, and the number of illuminated elements is too few. While an increased ablator thickness can be used to smooth out the inhomogeneities, the targets cannot be made too thick, otherwise release waves cause problems. In some targets with an Al flash coating between target and LiF window, the VISAR shows the loss of reflectivity due to the LCLS X-ray pulse, which is a handy diagnostic for determining spatial and temporal overlap.

Reliable VISAR operation needs a planar drive; otherwise, there is loss of reflectivity and fringes move differently. Flexible real-time online VISAR analysis will be very beneficial.

6 X-ray beam requirements and expected scattering power

6.1 Bunch structure of the European XFEL

by K. Appel

The European XFEL will be operated at a repetition rate of 10 Hz. The number of electron bunches per 10 Hz pulse can be varied, within certain limitations, according to the experimental requirements. The maximum number of pulses per train is 2700, the minimum number is 0. The pulse length of the bunches depends on operation conditions such as bunch charge, electron energy, etc. and varies between a few and 100 fs (several 100 fs during the ramp-up phase of the facility). The microbunches are separated by 220 ns. With a full filling of bunches per train, 2700 bunches will cover a time span of 0.6 ms. The separation between bunch trains is then 99.4 ms (see Figure 6.1). Taking into account the maximum repetition rate of the optical long-pulse laser that will be used for dynamic compression experiments, a bunch filling in the facility of 1 bunch per pulse train is reasonable. The number of photons per pulse is on the order of 10^{12}. Compared to conditions at modern third-generation light sources, this is a typical number of photons per second (see Figure 6.2).

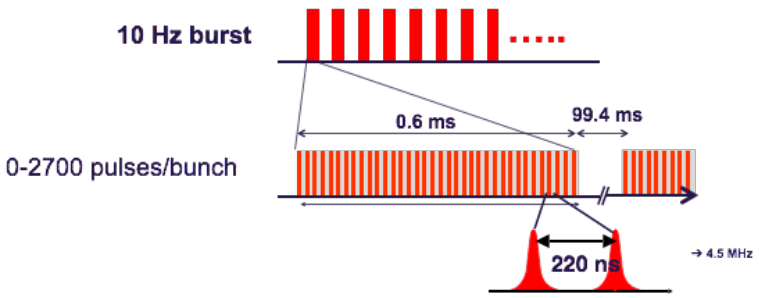

Figure 6.1: Bunch structure of the European XFEL. The facility will be run at 10 Hz. With a bunch filling of up to 2700 at maximum, a repetition rate of 4.5 MHz can be reached. It has to be noted that the bunch train takes 0.6 ms and is followed by a gap of 99.4 ms.

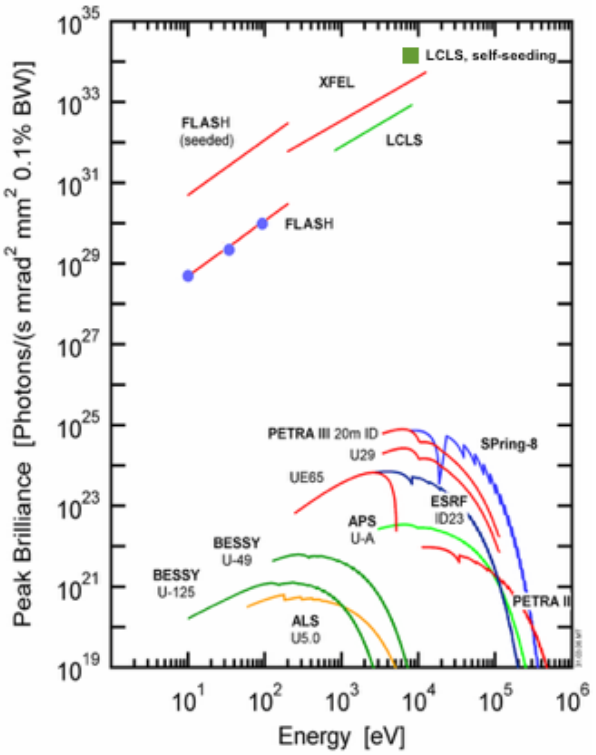

Figure 6.2: Peak brilliance vs. photon energy of modern third- and fourth-generation sources

6.2 CRL focusing provided by HED

by K. Appel

The focusing concept at the HED instrument has been described in detail in the technical design report (TDR) of the European XFEL. Here, we summarize the most important features relevant for dynamic compression experiments.

The focusing scheme at HED is based on Be compound refractive lenses (CRLs). Three different focal sizes in the following ranges will be available at the sample positions (972 m and 977 m from the source) at HED: 200 µm, 20 µm, and 2 µm. This will be achieved by three different CRL lens changers positioned at 229 m, 857 m, and 962 m from the source (see Figure 6.3). The CRL lens changers are equipped with 10 lens cassettes, each holding up to 10 lenses per cassette. The optics concept was designed in such a way that the flux at the sample position is maximized. The minimum transmission of the European XFEL through the CRL lenses is 0.9 for the entire energy range. Since Be lenses are chromatic, a different choice of lenses has to be made per energy. Focusing will be achieved for the energy range of 5–25 keV at both interaction regions. At the moment, focusing to the range of 2 µm above 22 keV

is not foreseen for Interaction Area 1 (IA1) but can be achieved by implementing 10 additional lenses into the CRL3 holder. Focusing to beam sizes below 1–2 µm FWHM is not possible with the envisaged scheme due to the large focal distance of about 10 m for the last CRL holder and the high coherence of the European XFEL beam: this is below the diffraction limit of this setup but can be achieved by placing an additional lens set closer to the sample.

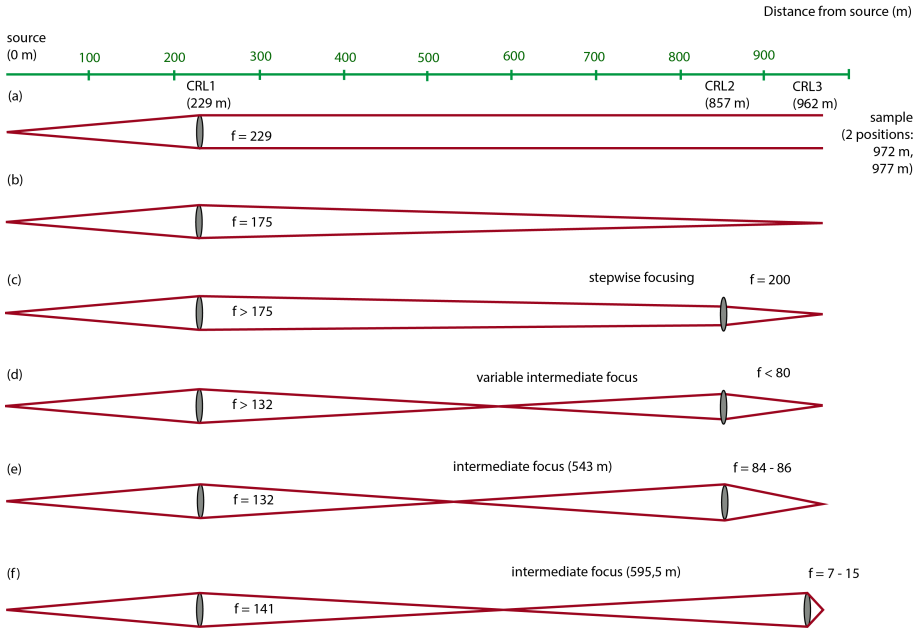

Figure 6.3: Schematic of options for the collimation and focusing scheme at the HED instrument

6.3 Nanofocusing

by A. Schropp

We aim to implement a nanofocusing setup for high-resolution X-ray microscopy and for creating extreme conditions in matter. The setup will be based on Be CRLs, which can stand the full intensity of an X-ray FEL pulse and have been employed as focusing optics in various experiments at LCLS [130, 132, 131].

6.3.1 Beryllium compound refractive lenses

Parabolic CRLs are common X-ray optics used in a variety of scientific fields for focusing applications 6.4 . Since their invention in 1996 [142], the lenses have proven their performance in full-field microscopy, magnified imaging [92], and focusing [129].

They have been widely employed as beamline optics at PETRA III, ESRF, and in recent years at LCLS as well. In full-field imaging, a spatial resolution of about 100 nm has been reached [128]. In focusing experiments, diffraction limits well below 100 nm are expected. The smallest beam size achieved so far is about 100 nm FWHM, at the MEC instrument at LCLS [106].

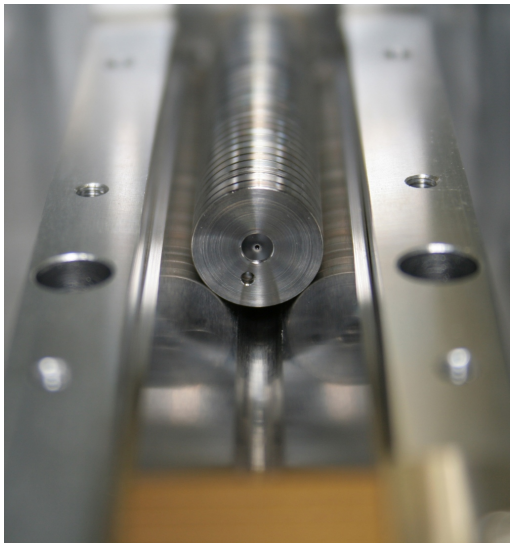

Figure 6.4: Be lenses in holder

E [keV]	f [mm]	N	NA [mrad]	d_t [nm]	wd [mm]	T_p [%]	Gain
8.0	100	52	0.91	64	71	15	3.1×10^6
	200	24	0.58	100	187	35	2.9×10^6
	300	16	0.42	137	288	47	2.1×10^6
	400	12	0.33	174	388	56	1.5×10^6
12.0	200	56	0.59	65	168	37	6.4×10^6
	300	36	0.43	91	281	51	4.5×10^6
	400	27	0.34	116	383	59	3.2×10^6
18.0	200	138	0.55	48	119	27	7.8×10^6
	300	84	0.41	63	252	42	6.3×10^6
	400	61	0.32	80	368	52	4.7×10^6
25.0	300	173	0.37	51	202	28	5.4×10^6
	400	122	0.30	62	331	38	4.6×10^6
	500	95	0.25	75	449	46	3.7×10^6

Table 6.1: Imaging parameters for a stack of N Be CRLs with a radius of curvature $R = 50\,\mu\text{m}$ and a geometric aperture $2R_0 = 300\,\mu\text{m}$ at different X-ray energies between 8 keV and 25 keV

In Table 6.1, various imaging parameters for different configurations of Be CRLs and X-ray energies are summarized. Here, a single lens has a radius of curvature of $R = 50\,\mu m$ and a geometric aperture of $2R_0 = 300\,\mu m$. Further parameters are the focal length f, the number of lenses N, the numerical aperture NA, the diffraction-limited spot size d_t, the working distance after the lens stack wd, the X-ray transmission T_p of the whole lens stack, and the effective gain as compared to the unfocused beam. A single lens has a thickness of $d = 1.1\,mm$ and a thickness of the material at the apex of $d = 30\,\mu m$. With these lens stacks, the X-ray FEL beam can be focused with a high gain in X-ray photon density to a size of about 50 nm (FWHM) at working distances of around 100 mm. The lenses will be mounted on a set of linear stages and a hexapod to align the optics with at least five degrees of freedom (three linear axes and two rotations). Depending on the X-ray energy and the desired focus size, the working distance between the lens and the focus varies between 50 mm and more than about 500 mm (see Table 6.1). Both interaction areas (IA1 and IA2) can provide the space to set up this instrument.

6.4 Cleanup slits

by K. Appel and H.-P. Liermann

Cleanup slits are required to prevent unwanted scattering from either uncompressed parts of the sample or the sample holder. They should be placed after the last scattering element in the beamline and, depending on the beam size, at different positions with respect to the sample. Here, we describe the cleanup slits for dynamic compression experiments using an optical long-pulse laser, but also for dynamic diamond anvil cell (dDAC) experiments in order to show possible synergies.

Cleanup slits can also be used to efficiently chop off third-harmonic (non-focused) beam while leaving the almost-focused fundamental untouched. This becomes possible given the large focal lengths at the HED instrument, where the fundamental beam will be tightly focused at the position of the cleanup slits, whereas the third harmonic is almost unfocused.

6.4.1 Requirements

6.4.1.1 For dynamic compression experiments using an optical long-pulse laser

Assuming that the laser-shocked area is 150–300 µm (depending on the pressure to be reached), one may want to focus the X-rays down to 20–50 µm in order to avoid any side effects. While a cleanup slit for this CRL-focused beam might not be essential for all experiments (in contrast to the DAC experiments), it is a desirable feature, i.e. a cleanup slit will reduce the exposure of the un-shocked and less-shocked area by the tails of the beam. It is essential though for SAXS experiments. For a 20–50 µm focused X-ray beam, one might use a 40–100 µm cleanup slit. The distance to the sample is not so critical and one might choose a distance of 100–200 mm from the sample. This distance has to be larger when the shock laser beam is coming from upstream, since it might collide with the cleanup slit. The details of the possible pinhole-to-sample positions still have to be worked out for the different geometries.

Optical laser beam size [FWHM, µm]	**Focused X-ray beam size** [FWHM, µm]	**Cleanup slit size** [FWHM, µm]
150	20	40
300	50	100

Table 6.2: Proposed cleanup slit sizes for different optical laser beam sizes and proposed X-ray beam sizes

6.4.1.2 For dynamic DAC experiments

Cleanup slits as close to the sample as possible are an essential feature for any DAC experiments. The reason is that the tails of the focused X-ray beam will hit the Re gasket surrounding the sample, making it very often impossible to see the weakly scattering sample. Even if the beam is cleaned with a slit far away from the sample, it might still create Re gasket scattering because of diffuse scattering that escapes the cleanup slit and that expands radially from the slit. Thus, in many high-pressure DAC beamlines, the cleanup slit has to be as close to the sample as possible. For the double-stage DAC (dsDAC), we propose a 1 µm^2 beam (FWHM) that would require a pinhole (cleanup) with a diameter of 7.5 µm positioned as closely as possible to the sample (directly on the back side of the diamond anvil). For dynamic DAC (dDAC) experiments, the beam size and the sample requirements relax to 10–40 µm^2 (FWHM) and thus require only a radius of the pinhole of 40–80 µm. The location of the pinhole with respect to the sample is also relaxed, i.e. it can be as much as 150 mm away.

This is also true for all laser-heated experiments, because the laser has to be guided to the sample at an angle and therefore it requires some additional space.

Sample size [FWHM, µm]	**Focused X-ray beam size** [FWHM, µm]	**Cleanup slit size** [FWHM, µm]
1	1	7.5
20	20	40
40	40	80

Table 6.3: Proposed cleanup slit sizes for different DAC sample sizes and proposed X-ray beam sizes

Especially the very small size of the cleanup silt and the closeness to the sample required for the DAC setup make it extremely difficult to design an adequate cleanup slit system. In the following, we describe the basic cleanup slits already foreseen for the HED instrument and the proposed cleanup system close to the sample.

6.4.2 Implementation

6.4.2.1 HED cleanup slit system

A high-power slit system is planned at the entrance of the optics hutch of the HED instrument. This slit system is water-cooled and consists of 5 mm TaC blades with a 75 mm layer of B_4C deposited on their upstream side. Here, the B_4C acts as an absorber of the incoming beam and the TaC as a blocking device. This slit system can cope with the full repetition rate of 4.5 MHz and half a bunch train of the European XFEL. However, it cannot be fully closed during the entire bunch train and thus is only meant to slit down fractions of the incident beam at high-repetition-rate experiments (for low-repetition-rate experiments and shot-on-demand, the requirements are somewhat relaxed).

The European XFEL beam is further shaped in the optics hutch by CRL lenses and then potentially interacts with attenuator foils, a diamond grating, a timing tool, and a spectrometer. All these devices create parasitic scattering. In order to clean the beam from this parasitic scattering, a second slit system is foreseen, 2 m in front of the sample in IA1 and 4 m from IA2. This slit system consists of two components, a low-Z slit system and a subsequent high-Z slit system. Because sharp edges are known to cause significant scattering, the low-Z slit system will consist of a *soft edge* realized by means of a rod made of Si_3N_4 with a diameter of 3 mm mounted on a 2 mm Ta blade. This results in a gradual change of the transmission of the beam (see

Figure 6.5). Directly downstream, a high-Z slit system will be installed, consisting of 4 mm thick TaC blades protected by a 6 mm thick B_4C layer mounted on the upstream side. The B_4C layer is about one tenth of the thickness of the high-power slit system: assuming that only 10% of the incoming beam are scattered at this slit system, this is considered sufficient.

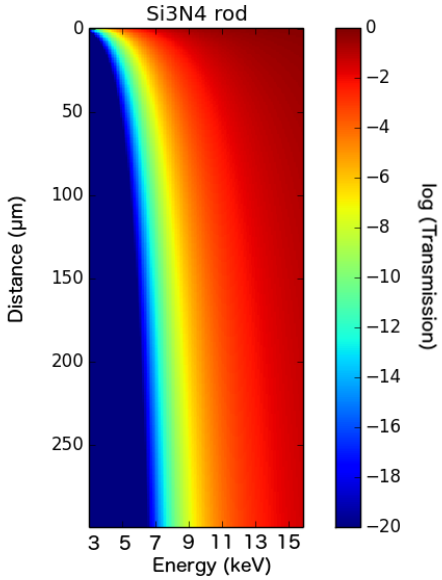

Figure 6.5: Transmission of the first 300 µm of a Si_3N_4 rod blade mounted on a 2 mm thick Ta blade. The rod has a diameter of 3 mm.

6.4.2.2 Specific cleanup slits for DAC and dynamic compression

Because of the large amount of heat that will be deposited into the cleanup slit (pinhole) when cutting the tails of the beam, we agreed for the moment on the following design of the cleanup slit: The pinhole will consist of a layer of B_4C that is bonded to a foil of TaC. Because pinholes of 7.5 µm can only be laser-cut into a 1 mm thick assembly, the thickness of TaC will be 0.4 mm and that of B_4C 0.6 mm. This will result in a factor 10 more absorption than necessary according to the absorption length of TaC at 25 keV (see Figure 6.6). Because it is likely that the pinholes will be damaged after a series of experiments, we are planning to place multiple pinholes on a grid in a 5 cm $\times$ 5 cm large piece of the sandwich.

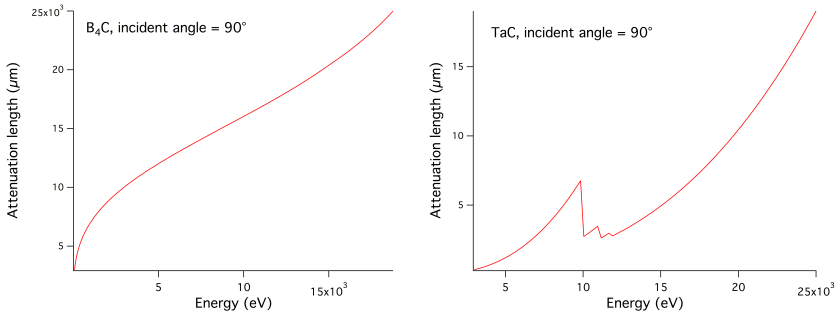

Figure 6.6: Attenuation length for B_4C (left) and TaC (right). At 10^{12} photons per pulse, we need twice the attenuation length to reduce the transmitted photons to a manageable amount. This means we would need at least a 40 µm thick foil of TaC with a 20 mm B_4C layer.

6.5 X-ray double pulses

Recently, X-ray FELs have become capable of delivering two subsequent pulses with a defined delay. This can be achieved by two different methods.

6.5.1 X-ray split and delay line

by K. Appel and U. Zastrau

Split and delay lines (SDLs) [162, 122] split a single X-ray pulse, transport the two parts on two paths of different length, and recombine them before they are both focused onto the target. These devices offer delays of up to several 10 ps with a small temporal jitter of only a few fs. The challenge when using an SDL for any experiment is to distinguish the measured signature from the pump pulse from the contribution of the probe pulse, since they are collinear and have the same photon energy.

Using the FLASH facility at DESY in Hamburg (Germany), a first plasma physics experiment using two XUV pulses was performed: the energy exchange rate between the electronic subsystem and H_2 molecules in a liquid-density hydrogen plasma was studied . Using two time-delayed XUV pulses, the scattering amplitude from the probe pulse increased by a factor of 5 within 1 ps because the H_2 molecules undergo dissociation due to heat [169].

Two different photon energies (so-called two-colour mode) in combination with SDLs can be achieved by spectrally filtering the two paths differently. In general, the ~ 1% third-harmonic content of the European XFEL could be used together with the

fundamental photon energy.

The SDL for the HED instrument has been described in detail in the TDR of the European XFEL and also in [121]. Here, we repeat the most important features relevant for dynamic compression experiments.

The SDL delays one part of the European XFEL beam with respect to a second part. This is achieved using a sharp mirror, which is moved into a part of the beam (BS: beam splitter; see Figure 6.7). One part of the beam remains unchanged while the other part is reflected. After this splitting, the two beams travel along different paths that both include two mirrors. The delay between the two beams is achieved by moving these mirrors such that their incident angle with respect to the X-ray beam is kept constant while the path length is changed. Recombination of the two beams is achieved by a recombination mirror (RC), which reflects only one part to the last mirror while the other beam impinges directly on the last mirror. The achievable delays are summarized in Table 6.4. All optical devices of the SDL are multilayer mirrors. Two different coatings have been selected to achieve a high reflectivity over the total energy range of 5 to 20 keV. Each mirror will have two coating stripes besides each other. By translation of the entire SDL, it is possible to change between the coatings. The multilayer mirrors are not cooled. Therefore, the SDL allows the shot-on-demand modus.

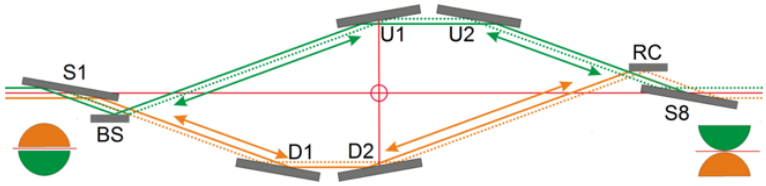

Figure 6.7: Geometry and beam path of the split and delay line

As a special operation mode of the SDL, two-colour operation will be tested. In this mode, the third harmonic is delayed relative to the first harmonic. This mode requires special tuning of the accelerator and the SASE2 undulator of the European XFEL to enhance the generation of fundamental and third-harmonic FEL radiation, and tuning of the beam transport mirrors to propagate both photon energies. For the SDL, it is required that the S1 mirror reflects both photon energies at high efficiency, while the four mirrors in the two arms need to reflect only one photon energy. The two beams will not be recombined at the SDL, but rather leave the device with a vertical offset, as shown in Figure 6.8. This offset is 7.47 mm for 20 keV and 6.7 and 10.33 mm for 15 and 5 keV, respectively. The corresponding delays between first and third harmonic are 250 fs and 445 fs, respectively.

The offset can be compensated by a tilt of the RC mirror such that the two beams

Photon energy [keV]	**Multilayer top material**	**Angle** [°]	**Maximum delay** [ps]	**Total transmission**
5	Ni(W)	3.66	23	0.23
6	Ni(W)	3.07	16	0.33
8	Ni(W)	2.3	9	0.47
10	Ni(W)	1.83	6	0.21
10	Mo	2.28	9	0.29
12	Mo	1.9	6	0.35
15	Mo	1.52	4	0.41
18	Mo	1.27	3	0.43
20	Mo	1.14	2	0.23

Table 6.4: Delays achievable using the split and delay line

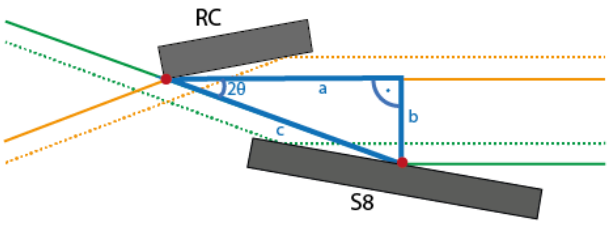

Figure 6.8: Geometry of two-colour operation of the SDL. The RC mirror is rotated such that the orange part of the beam does not hit S8, but leaves the SDL parallel to the green part of the beam.

overlap on the sample 100 m downstream of the SDL. A tilt angle of only 0.06 mrad and 0.08 mrad is sufficient for 20 keV and 15 keV, respectively, and is clearly within the acceptance angle of the multilayer (ML) mirrors. This design, however, has the disadvantage that the two beams pass a different number of mirrors in the SDL, making the transport of the two beams asymmetric. Likewise, the change of delay becomes much more complex and it would be preferable to insert an additional mirror in the path of the third-harmonic beam.

Furthermore, both the vertical offset and the different photon energies restrict the use of downstream optical elements, such as monochromator, CRL2, and CRL3. An initial idea to use the existing monochromator in the probe beam for higher spectral resolution appears not feasible any longer. Most realistic at present is a scheme where both beams are transported parallel into the HED optics hutch, in which a special optics setup based on multilayer mirrors is used to recombine and focus the two beams. This setup requires further design and can be achieved as a future extension of the HED instrument.

6.5.2 Two-pulse and two-colour schemes

by U. Zastrau

A two-pulse mode can also be established already within the European XFEL undulators [94, 95], with delays of up to a few 100 fs. At the SASE2 undulator, a maximum delay of 400 fs will be available initially. Here, the pulse energy is typically lower than in the regular operation mode. As a more sophisticated option, a maximum photon energy difference of $\sim$ 1% (typically within the SASE bandwidth) between the two pulses can be achieved.

In a non-standard operation mode, consecutive radio frequency (RF) bucket filling of the superconducting accelerator at 1.3 GHz yields subsequent X-ray pulses with 770 ps time delay. Multiples of this value seem very interesting for studying the temporal evolution of shocked samples.

6.6 Monochromators

by K. Appel

The natural energy bandwidth of the SASE radiation is 10^{-3}. Several methods require a smaller bandwidth, such as 10^{-4} for diffraction experiments and $< 10^{-5}$ for

inelastic X-ray scattering experiments. One way to reduce the energy bandwidth is the use of monochromators. Due to heat load constraints, it is good practice to reduce the bandwidth by a factor of 10 at most with one monochromator. At HED, a generic Si_{111} monochromator is foreseen, which will reduce the bandwidth to 10^{-4}. This monochromator can be used as a pre-monochromator for a downstream high-resolution monochromator. Except for the CRL1 unit, which can also be used to collimate the beam, all focusing elements are positioned downstream of the monochromators (see Figure 6.9). This will allow a better monochromaticity of the beam to be achieved than when letting a divergent beam pass the monochromator.

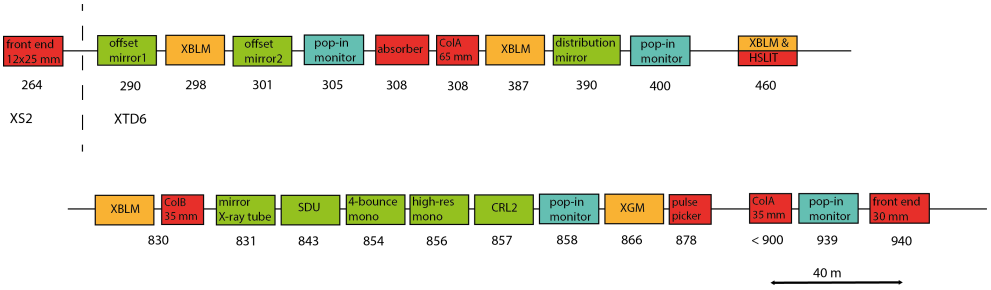

Figure 6.9: Positions of devices in the HED beamline. The generic monochromator is planned to be placed at 854 m from the source, the high-resolution monochromator is foreseen to be positioned at 856 m from the source. This is roughly 116 m upstream of the experiment.

6.6.1 Generic Si_{111} monochromator

The generic Si_{111} monochromator will cover an energy range of 5–25 keV. For stability reasons, it is designed as a channel-cut monochromator. The geometry of the crystals has been designed such that it allows 6σ of the European XFEL beam to pass. The offset of the channel-cut crystal is energy-dependent and varies between 10 and 11 mm. It will be compensated to zero by a second channel-cut monochromator reflecting in the opposite direction (see Figure 6.10). This facilitates the operation of the optical components and the experiment downstream of the monochromator and also the change between monochromatic and SASE beam. The second part of the four-bounce monochromator can be removed, so that the first part of the monochromator can serve as a pre-monochromator for the downstream high-resolution monochromator. The generic four-bounce monochromator is cryogenically cooled and thus allows pulse train operation.

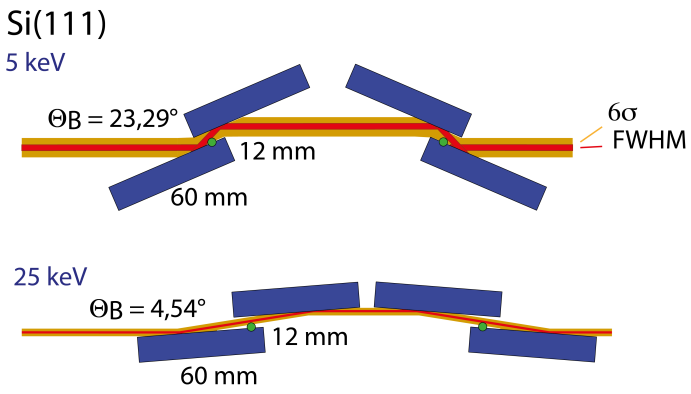

Figure 6.10: Concept of the Si_{111} monochromator. The second channel-cut crystal can be removed from the beam to allow the offset beam from the first channel-cut crystal to enter the backscattering monochromator.

6.6.2 High-resolution monochromator

To achieve an energy resolution of 10^{-6}, an additional channel-cut monochromator is planned at HED. The monochromator has not been designed yet but the concept is quite evolved already. The concept is to have a higher-order cut of Si operated in backscattering geometry that will give a sufficient reduction of energy bandwidth.

It is planned to operate this monochromator downstream of the generic Si_{111} monochromator for two reasons:

- Reduce the heat load on the high-resolution monochromator
- Compensate for the offset of the backscattering monochromator

The offset of the backscattering monochromator depends on the operation angle (which should be close to 90°), the *d* value of the reflection, and the length of the monochromator. By choosing an appropriate length, it can compensate the offset of the first part of the generic monochromator to zero. In this configuration, the zero offset and pre-monochromatization can be kept with the fewest reflections (see Figure 6.11). Thus, the flux of the monochromatic X-ray FEL is maximized. Due to the selection of a special Si reflection, the high-resolution monochromator can be operated at restricted energy points only. The current concept foresees to use Si_{335} at about 87°. This corresponds to a photon energy of 7.5 keV at a bandwidth of about 5×10^{-6}. The envisaged repetition rate is 10–20 Hz. No cooling is required at this repetition rate and bandwidth reduction. For the moment, a placeholder is foreseen in the XTD6 photon distribution tunnel for the high-resolution monochromator.

Recently, the HED group bought four diced Si analysers from ESRF with a (533) cut

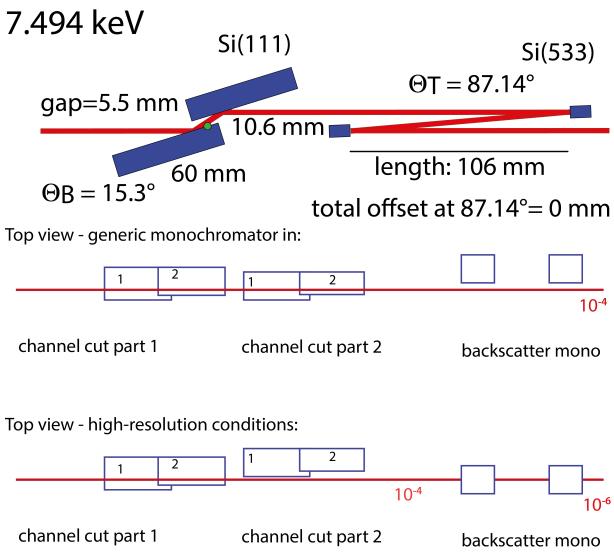

Figure 6.11: Concept of Si_{111} and backscattering monochromator (top) for a Si_{444} reflection as an example. Zero offset can be obtained for matched reflections and crystal distances, i.e. for one specific energy. The second part of the four-bounce monochromator is moved to the side, allowing the monochromatic beam to pass and enter the total-reflection monochromator at an offset (resulting from the offset of the first channel-cut crystal; bottom).

that are designed for operation at a photon energy of 7.494 keV. The advantage of the (533) reflection is that there is no lower-order reflection that would reflect few-keV thermal bremsstrahlung from shock-compressed matter. Hence, this diagnostic is background-free. Currently, it is envisaged to install an equivalent (533) channel-cut crystal in the high-resolution monochromator. It will be equipped with temperature diagnostics to study heating of the first reflection by the X-ray pulses. A similar setup at ESRF (ID 25) operated successfully only after a temperature stabilization of 10^{-5} °C was established. Experience with this initial system will eventually lead to an improved upgrade of the inelastic scattering setup at HED in 2019–2020.

6.7 Scattering power

by H.-P. Liermann

The estimation of the scattering power of the un-shocked and shocked target is essential in order to carefully plan an experiment, i.e. to determine what incident beam flux is necessary to create enough scattered photons to be detected on the different detectors. We used the theory of Blome, Tschentscher, Davaasambuu, et al. [15] to estimate the scattering power of iron with different target thicknesses. The details of the calculations are listed in Appendix A. In Table 6.5, we show that each pixel of a detector with a 0.2 mm pixel size that is exposed to the centre of the (110) reflection of an iron foil (25 or 100 µm thick) will receive about 10^4 to 10^5 photons per pulse assuming an incident flux of 10^{11} to 10^{12} at 25 keV, respectively.

The PerkinElmer detector (one of the detectors considered for these X-ray experiments, see sec.

Another point to discuss is the question of what effects the coherence of the beam has on the diffraction image. This issue has been discussed, and it was found that it will play only a minor role because, at 25 keV, coherence is significantly reduced in comparison to 8 keV, and diffraction experiments at the MEC instrument at LCLS [106] indicate that diffraction experiments at 8 keV still yield decent diffraction images [58].

Scenario	N_0 [ph/pulse]	T	$N_{I,exteff}$ [ph/pulse]	A [µm^2]	h [µm]	V [µm^3]	$\lvert F^2 \rvert$	$\Theta_{(110)}$ [°]	N_{110}	$N_\mathbf{p}$
25 keV	10^{12}	0.78	6.4×10^{11}	20	25	10 000	141.9	7.027	5×10^5	2×10^5
$(\Delta E/E = 10^{-3} BW)_{\text{vac}}$										
		0.35		20	100	40 000	141.9	7.027	9×10^5	4×10^5
25 keV	10^{11}	0.35	6.4×10^{10}	20	100	40 000	141.9	7.027	9×10^4	4×10^4
$(\Delta E/E = 10^{-4} BW)_{\text{vac}}$										

Table 6.5: Calculations for $N_\mathbf{p}$ (photons per pixel) for (110) reflection of an iron foil with different thickness based on [15] for a wavelength of 25 keV. Details of the calculations are shown in Appendix A.

7 Analytical X-ray methods

7.1 X-ray scattering

by M. McMahon, R. Briggs, and H.-P. Liermann

X-ray scattering may be subdivided in scattering from crystalline materials and from non-crystalline materials, such as glasses and melts. Both of these techniques have important implications for shock compression experiments, which we discuss below.

7.2 X-ray diffraction (XRD)

The positions of Bragg X-ray diffraction peaks from powders and single crystals may be used to determine the size and symmetry of the unit cell, while the atomic arrangement in the unit cell may be inferred from the intensity of the diffraction peaks. By studying these atomic parameters as a function of *intensive* thermodynamic variables such as pressure, temperature and, in this particular case, strain rate, we are able to deduce information on the compression, thermal expansion, and plasticity of the material, respectively. In order to describe the compression behaviour of the unit cell, one may use an equation of state (EOS) that e.g. models the change in volume as a function of pressure (PV-EOS). On the other hand, the intensity variation of diffraction peaks has been used to observe changes in bond lengths and angles between the atoms in the unit cell as a function of pressure and/or temperature, in order to learn more about the atomistic response of a structure to these intensive variables and investigate why a change from one structure to another may occur. Both sets of information help us to systematically understand phase changes as a function of pressure, temperature, and strain rate. Finally, these data may be used in geophysics to model the composition, structure, and dynamics of planetary bodies such as the Earth [39, 152, 31].

However, while single-crystal diffraction has been used in conjunction with X-ray back lighters to identify phase changes in materials under dynamic compression, it is only with the recent advent of X-ray FELs, with their ultrahigh-brightness, high-energy X-ray beams, that high-precision lattice parameter information has become available from powder diffraction measurements. X-ray FELs will also enable the measurement of accurate peak intensities from powders, enabling the determination of atomic positions within the unit cell.

While X-ray diffraction (XRD) measurements in the recent past have focused on EOS measurements under shock compression, we expect that the increasing use of X-ray FELs will lead to a much broader range of information being measured, particularly on materials of geophysical and materials science interest. Below, we give some examples that describe the actual use of diffraction data obtained at extreme conditions, and the critical issues that one should be aware of when collecting these data.

XRD requires the collection of large areas of the Debye–Scherrer pattern, which calls for large-area detectors. The detectors should be motorized but have very well defined locations, so that setup time is efficient and data are integrated accurately. The measurement of accurate peak intensities is absolutely vital, and so large detectors with constant gains and backgrounds, and only small dead areas, are essential. The suppression of the higher harmonics of the X-ray FEL beam is also important for XRD, as otherwise additional diffraction peaks will appear in the data. However, since the HED beamline mirrors start cutting the spectrum above ~ 23 keV, higher harmonics will not be present at fundamental photon energies in excess of 12 keV.

Pre-characterization of targets, in particular of textured targets, will be very important. The thickness of the targets should be optimized to maximize the XRD signal, as the sample could be crystalline but also non-crystalline such as a glass or (dense plasma) fluid. The thickness of the targets used will also depend on the drive laser pulse length.

As discussed in Section 2.5.1, the temperature measurement, particularly of off-Hugoniot states, has been a long-standing challenge in the field of dynamic laser compression. The Debye–Waller factor leads to an enhanced decrease in the intensity of high-angle Bragg peaks, and the sample temperature might therefore be obtained directly from the diffraction pattern. However, careful experiment design and data analysis will be required in order to separate out the effects of temperature from other effects (such as sample texture and detector effects) that will affect the diffraction intensities.

7.2.1 High-P high-T EOS studies

From the powder and single-crystal diffraction pattern, we are able to extract the parameters of the unit cell and thus determine its volume as a function of pressure, temperature, and strain rate. Isothermal equations of state are used to describe the pressure–volume (P–V) change. The concept of applying an EOS to solids was

originally used by Murnaghan [103, 104] and further modified by Birch [12] and relates the volume/pressure slope to the *bulk modulus*, which is the inverse of the compressibility and is defined as the second derivative of the lattice energy with respect to volume (e.g. [56]). Over the years, different types of EOS have been suggested [1, 45, 2] to fit both compression and thermal expansion data and relate the P–V–T EOS to physical and thermodynamic properties such as bulk modulus, Grüneisen parameter, thermal expansion, etc. (for a detailed review see [1, 45, 76, 2, 145]). These data can then be used e.g. to help interpret seismic profiles, such as in the case of the Preliminary Reference Earth Model (PREM) [39, 127, 126, 43]. While the approach mentioned above is widely used in the static high-pressure research community, extracting such data from shock-compressed matter will be a key goal. The pressure achieved in dynamic laser-compression experiments is not as high as that achieved in the DAC or the multi-anvil press. This is mostly because the shocked materials are typically highly strained. A good indicator of the presence of these non-hydrostatic conditions is the differential shift of the different diffraction peaks, and peak broadening in single crystals such as quartz [36, 3]. In powders, on the other hand, macro-stresses produce strain that causes the diffraction lines to shift differentially, depending on their Miller index, whereas the strains produced by micro-stresses result in diffraction line broadening [134]. In powders of materials with cubic symmetry, one can infer the macro-stresses by calculating the uniaxial stress component [135, 137, 136]. In single crystals, one can analyse the evolution of the measured Eulerian strain tensor to determine if the hydrostatic character of the experiment is changing (e.g. [2, 52, 79]) or look directly at the deviatory stress (e.g. [36, 171]).

7.2.2 Phase stability studies

Studies on phase stability and phase transitions (solid–solid and solid–liquid) at simultaneous high pressure and high temperatures have been a long standing topic of interest in the field of extreme-conditions research. In principle, one defines a phase boundary by approaching it from both higher and lower pressures and temperatures, and records the onset of the transition as its limit. In the case of shock compression, one can only approach the phase boundary from the low-pressure/temperature side, although collection of data on release has also been used to identify phase boundaries, including the melting curve.

One of the most interesting phase transitions studied using shock compression has been the transition in diamond to the supposed BC8 phase at ~ 1 TPa (see Section 2.1.2). Despite considerable effort, the location of the transition is not yet determined. However, when the transition to the metallic or semi-metallic BC8

phase is found, a refinement of the full crystal structure will provide a stern test of our abilities to determine such structures at extreme pressures and temperatures. Another example of an important transition is the onset of melting as a function of pressure and temperature. There has been much work on this subject in the last 30 years, but despite this there is still vigorous debate as to what diffraction features—e.g. the disappearance of diffraction peaks or the appearance of diffuse scattering from a melt, or both—are indicative of melting. The melting curve of Fe at ultrahigh pressures is of particular interest, as it is important for planetary modeling.

7.2.3 Plastic–elastic behaviour of mantle minerals

The study of the plastic–elastic properties of minerals at high pressures is a relative new subject, not only to static high-pressure diffraction work but also to shock/ramp compression. In the case of shock/ramp compression experiments, this is mostly because to date no one has been able to collect reproducible intensity data. Nevertheless, the plastic–elastic properties of materials have significant implications for both geophysics and materials science (see Section 2.2) since they are vital to understanding flow behaviours in planetary interiors, as well as deformation pathways and strain rate dependencies. Because most oxides and silicates become ductile at 15–20 GPa and deform under the application of uniaxial stress by the shock laser, one may infer likely deformation mechanisms by interpreting preferred orientation patterns (texture). This technique, termed *radial diffraction*, originated in the DAC community and allows the study of texture development during the compression experiment using Rietveld refinement and the extraction of the orientation distribution function (with specialized software such as MAUD). Diffraction data from deformed polycrystals, combined with polycrystal plasticity models, have emerged as a powerful tool for inferring microscopic deformation mechanisms such as active slip systems. An extensive review on the subject from the static compression side can be found in Wenk, Lonardelli, Merkel, et al. [159].

7.2.4 Diffraction on nanocrystalline powders, amorphous solids, and liquids: Use of total scattering function in DAC

Using the total scattering intensity function to study the local structure of amorphous compounds and melts has been a fast-growing field of research at X-ray FELs because of the increased flux available in a very short time. As such studies benefit greatly from the use of high-energy X-rays in order to increase the Q-range over which the data are collected, the European XFEL is the ideal X-ray source. More recently, the application of total scattering methods to the study of nanocrystalline

materials, and the analysis of its pair distribution function (PDF) to interpret the diffuse scattering part of the peak (tails), has significantly advanced the structural analysis of nanocrystalline materials, which are mostly present during the very fast compression through a laser shock.

The study of the total scattering function at simultaneous high pressure and temperatures is a rather new subject in the field of extreme-conditions research, but has become of significant importance for understanding the dynamics of the interior of the Earth and other planetary bodies (see reviews by Duffy [38] and Duffy [37]). In particular, the study of the structure of glasses as analogues for melts, or the study of melts themselves at high pressure, can help us to understand the chemical differentiation of planetary bodies (such as the Earth) over time (e.g. [90, 82]). We thereby gain information on how Earth-like planetary bodies evolved from a potentially homogeneous molten magma ocean to the segregated structure that we see today (crust, mantle, and core). Of particular interest for these studies are changes of the glass/melt structure as a function of pressure and temperature, and the correlated changes in basic thermodynamic and transport properties such as density and viscosity, respectively. Structural changes of the glasses and melts can be studied by looking at the first strong diffraction peak (FSDP), which is related to the inter-polyhedral linkages, as well as the long-range oscillations correlated to the nearest-neighbour (tetrahedral) packing (see review by Wilding, Wilson, and McMillan [161]).

Measurements of the total scattering function of nanocrystalline materials at higher pressures and the analysis of its Fourier transform, the PDF, is an even newer subject in extreme-conditions research (see introduction by Parise, Ehm, and Michel [111]). The aim is to complement structural analysis of Bragg diffraction patterns by looking at the change in atomic arrangement in a nanocrystalline material, which leads to diffuse scattering and thus to significant broadening of the diffraction peaks [41]. The ultimate goal is to better understand why nanomaterials behave so differently at high pressure from their bulk counterpart, e.g. the phase transition in the nanocrystalline material occurs at much higher pressure compared to its bulk crystalline counterpart (e.g. [41, 156]). While studies such as this one are now actively undertaken in the static high-pressure research community, to our knowledge, they are not yet convincing in the field of shock compression, again mostly because the diffraction intensities of the X-ray FEL have been to unreliably to actually retrieve quantitative information. However, we know from recent X-ray diffraction studies at LCLS that diffraction peaks are very broad in shock-compressed materials, suggesting particle sizes of only ~ 20 nm in the compressed material. Collecting total scattering data from such materials would provide significant new information on the local disorder of the materials during shock compression, a completely new field of research.

7.3 X-ray phase contrast imaging (PCI)

by A. Schropp

The nanofocusing setup will allow us to carry out high-resolution X-ray imaging experiments as well as to create extreme states of matter. The first scenario is based on X-ray phase contrast imaging (PCI) and requires to focus the European XFEL beam closely in front of a sample (see Figure 7.1 a). The divergent X-ray beam then hits the sample at a certain distance x_s after the focus, and the illuminated area is then imaged by a high-resolution X-ray detector much further downstream. For typical distance values of about x_s = 100 mm between focus and sample and x_d = 5 m between sample and detector, a magnification of $M \approx 50$ can be obtained. By using a high-resolution X-ray detector with a pixel size of p = 2.25 µm, this yields an effective pixel size in the phase contrast image of p_{eff} = 45 nm with a field of view of about 100 µm.

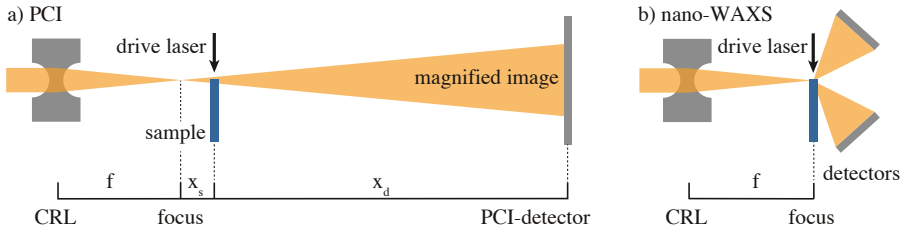

Figure 7.1: a) Schematic outline of the setup used for magnified inline PCI experiments. b) Nanodiffraction geometry.

The method will enable us to image fast dynamical processes in matter, providing detailed information about the shock speed and the compression of a material [131]. By moving the sample into the focal plane of the optics (see Figure 7.1 b), local structural information about the sample can be obtained by large-angle X-ray scattering. In this way, phase transformations, which often occur in highly compressed materials, can be investigated with a high spatial resolution. An example of a propagating elastic wave in diamond is shown in Figure 7.2 [131].

A prototype setup was built for the MEC instrument at LCLS and will be redesigned within HIBEF. The setup will provide all degrees of freedom to align Be CRLs and the sample. A pinhole and a beam block are used to clean the X-ray beam from X-ray scattering background and to protect the detector from damage, respectively. The setup will allow us to characterize the nanobeam by ptychography and pursue PCI experiments without the need to exchange technical components.

Results from the LCLS show that the illumination function and non-perfect lens

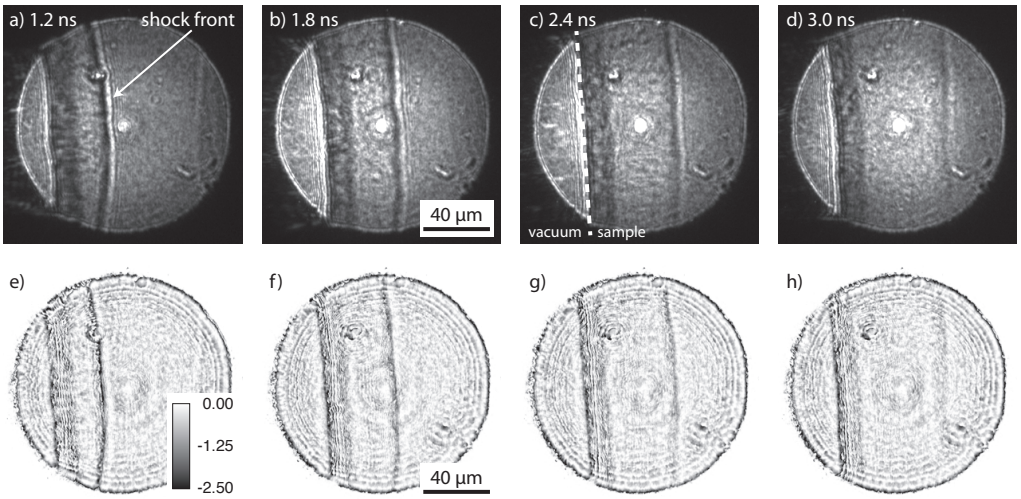

Figure 7.2: a)–d) Phase contrast images measured by a high-resolution X-ray detector at a distance of 4.2 m behind the diamond sample. Specific time delays are indicated in each image. e)–h) Corresponding phase maps obtained by iterative phase retrieval from the images above.

performance can be accounted for when using ptychography to characterize the X-ray optics. PCI can then resolve 1% lattice compression and achieve a spatial resolution of a few 100 nm with SASE beam. In transverse shock geometry, this technique can be combined with *zoom-in* into single phases in the compression and get XRD patterns from a selected phase only.

Correction lenses made from phase plates for all the Be lenses can be manufactured, which correct tiny shape errors in the Be. This optimization can be used with different photon energies.

7.4 X-ray absorption spectroscopy (XAS)

7.4.1 Science requirements

by M. Harmand

One interesting aspects of matter under extreme conditions is the strong coupling of electronic and atomic effects. The interplay between electrons and ions infers directly on the transport properties and is at the origin of exotic properties of matter. For example, bond hardening, ultrafast transparency, complex and metastable crystallographic phases, or even inversion of the melting curve have been observed [62, 61].

Some of the most striking processes that have been evidenced experimentally are the bond weakening in covalent materials leading to non-thermal melting [148, 124, 138], insulator–metal transitions [21] or, on the contrary, the *bond hardening* in transition metals [160, 116] leading to an increased melting temperature. Indeed, in some materials such as Al, the loss of crystalline structure is observed to occur on a ps time scale that is understood as a thermal phase transition [97, 35]. The heated electrons transfer their energy to the ions, and solid–liquid transition occurs when the ionic temperature exceeds the melting temperature. In some materials such as Au, the melting transition occurs within longer time scales (a few ps), indicating increased lattice stability (bond hardening) in non-equilibrium conditions [116, 160]. This was explained by the excitation of 5d electrons that would decrease the screening, leading to a few eV shift of the 5d band energy, as well as the increase of the effective ion–ion potential [118]. These observations demonstrate a strong correlation between electronic structure and lattice bonding, whose dynamics is still poorly understood.

Also, anomalous melting behaviour at ambient temperature and high pressure has been observed at 118 GPa / 300 K for Na and 50 GPa / 190 K for Li. It has been interpreted as the reorganization of the electronic structure at high pressure (orbital hybridization), inducing a change in the atomic structure [61].

Changes in orbital hybridization are also expected to occur during Fe melting, questioning its potential effect on the melting processes but allowing its detection to be related to the appearance of melting. This diagnostic has been used recently at LCLS to detect liquid Fe and further constrain the melting curve of Fe [66]. Because this effect is directly related to the change in the electronic density of state, it might occur at lower temperature than the ion reorganization, which would require more

energy to be damped in the system. This could imply a variation of the detected melting curve compared with the apparition of the X-ray diffuse scattering [81]. Further ultrafast studies at X-ray FELs using XAS could disentangle the electronic and atomic effects.

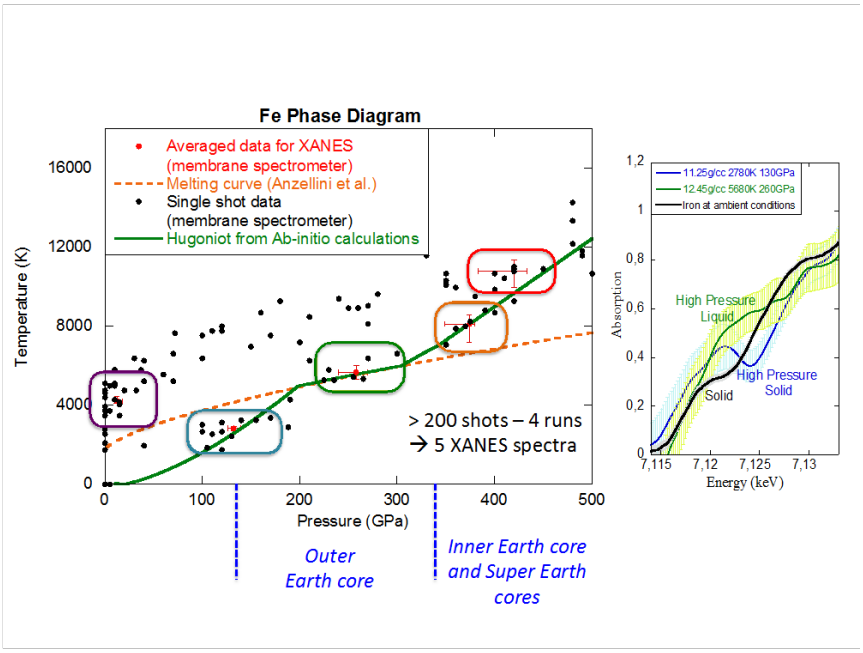

Figure 7.3: Experimental results from the L755 experiment at LCLS for pure Fe. *Left:* XANES spectra at solid ambient conditions (black line), compressed hexagonal close-packed (hcp) at 130 GPa (blue line), and compressed liquid at 260 GPa (green line). The accumulation of single shots is 6 and 13 shots for 130 GPa and 260 GPa, respectively. The error bar corresponds to the photon number statistic. *Right:* Fe phase diagram showing all the experimental data obtained and the one used for XANES accumulation.

In addition, the timescales involved in extreme-conditions physics ($<$ 100 ps for certain phase transitions, few ps for ultrafast melting, and tens of fs for changes in the electronic structures) necessitate using ultrafast time-resolved XAS (TR-XAS), with X-ray FEL sources being among the obvious best sources to produce the required keV, fs, bright X-ray pulses. Indeed, at synchrotron facilities, the shortest available X-ray beam pulse has a duration of $\sim$ 100 ps (synchrotron single-bunch pulse duration) and cannot distinguish faster processes. However, at these synchrotron sources, the fs-slicing technique provides a low photon number to achieve good-quality XANES measurements without long accumulation. More recently, the existing laser-plasma-based X-ray sources have demonstrated the ability to measure few-ps timescale XANES and EXAFS spectra [35, 97]. Nevertheless, these X-ray sources are limited to ps pulse duration and do not easily allow measurements at

K-edges above a few keV [64]. Betatron sources are promising sources but limited in providing a high photon number at several tens of keV. On the other hand, the LCLS provides both a very high single-shot photon number and fs time resolution, thus enabling the investigation of the mechanisms driving ultrafast non-equilibrium dynamics [19, 91]. However, while high-sensitivity XANES measurements have been well established at the X-ray Pump–Probe (XPP) instrument at LCLS and have seen many applications in the study of photoexcited transient states based on scanning an upstream monochromator, typically many thousand to hundreds of thousand pulses were averaged in order to obtain sufficient statistics. This renders the methodology impractical for studying non-reversible processes and *rare events* that can only be generated at a low repetition rate. Recently, we have optimized the acquisition procedure and the European XFEL operation mode to enable single-shot XANES with 1% signal-to-noise ratio and to perform EXAFS within a few single shots [67].

Because XAS allows the local atomic arrangement to be related (using EXAFS but also XANES) to the fine valence electronic state (XANES), it is currently one of the best diagnostics for characterizing these kinds of processes. In addition, TR-XAS allows one to follow step-by-step the intrication between electrons and atoms. At X-ray FELs, the achieved time resolutions are typically on the order of 10 fs [65], opening up fascinating perspectives to follow electron dynamics at extreme pressures and temperatures.

While X-ray absorption spectroscopy (XANES and EXAFS) is currently commonly performed at synchrotron facilities, its implementation at X-ray FEL facilities requires specific experimental developments [91, 53, 66]. This is especially true when studying irreversible processes, such as extreme-conditions studies where the shot-to-shot fluctuations are important and significant data accumulation or wavelength scans are limited. For example, shock-compressed matter or ultrafast laser irradiation as foreseen at the HED instrument are systematically destructive experiments, and their reproducibility is extremely sensitive to laser parameters and stability, sample quality, or even alignment procedure. These types of experiments demand single-shot dispersive XANES collection. Such an important effort has been made for example at laser facilities where ps X-ray sources have been used as backlighter to perform XANES on low energy edges (Al [9, 35] and Si [33]). More recently, XANES measurements on the Fe K-edge at LCLS were obtained by accumulating over several single shots [66]. Figure 7.3 shows five XANES spectra accumulated over 5 to 10 single shots over similar pressure and temperature conditions. The large shot-to-shot spectral fluctuations of the typical X-ray FEL make these measurements extremely difficult and call for specific X-ray FEL operating modes, acquisition procedures, and analysis.

The experience gained during three successive LCLS experimental campaigns has allowed the identification of the following requirements to perform single-shot XANES with a few-percent signal-to-noise ratio:

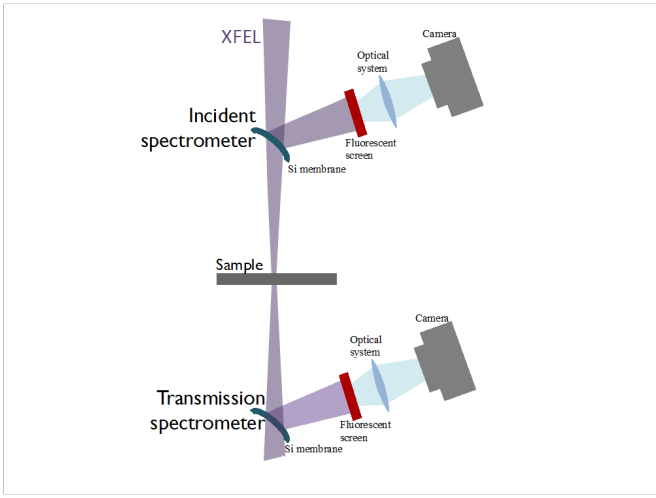

Figure 7.4: Experimental setup as used at LCLS, comprising two spectrometers before and after the studied sample

- Dispersive XANES consists of using a dispersive element to detect the XANES spectra without any scanning of the energy [112]. The use of dispersive XANES has been extended to X-ray FELs using single thick crystals [53], a grating [165], or two thin Si crystal membranes [172, 66].

- Measurements of the single-shot incident X-ray FEL spectra (I_0) and the alignment procedure can be done using two identical high-transmission spectrometers [66, 172] placed before and after the sample (see Figure 7.4). This design allows the use of a focused beam. These measurements can also be performed by taking advantage of the spectrometer spatial resolution [53] or by splitting the X-ray FEL beam [165]. When using two identical spectrometers placed before and after the sample, the alignment procedure is critical as the two spectrometers must be perfectly aligned and detect the exact same spectra. The feasibility of the alignment procedure must be ensured with adequate translation and rotation of the spectrometers (crystals and detectors). If using only one spectrometer and taking advantage of the spatial resolution coupled with an unfocused beam [53], one must ensure a minimum spatial spectral chirp along the X-ray FEL beam profile to obtain perfectly matched incident and transmission spectra.

- X-ray FEL operating mode: An important limitation for single-shot XANES

measurements is due to the SASE process, which prevents broad and smooth spectra. A recent experiment at LCLS allowed single-shot XANES to be reached with a signal-to-noise ratio of a few percent and over a 60 eV spectral range (preliminary analysis) by using an overcompressed and dechirped X-ray FEL beam. Specific tuning has to be optimized for XAS, requiring a strong implication from the machine experts.

- Optimization of the photon counting statistics by selecting an appropriate detector and to ensure around 10^6 ph/eV. Contrary to synchrotrons, this is less critical as X-ray FELs deliver high photon flux.

- A spectrometer with spatial resolution is required for the use of masks or with unfocused X-ray FEL beam. Indeed, spatial defects can be observed along the beamline or even be induced by the target itself. This last point is critical for laser-compressed/heated samples where spatial inhomogeneities might occur. In that case, masks can be used during the analysis process to minimize such effects or even select specific areas of the sample (pumped or un-pumped region for example if using an unfocused X-ray FEL beam).

- Mechanical stability of the spectrometer must be ensured to produce reliable reference measurements.

- Spectral resolution must be around 0.2 eV to detect the fine spectral features of XANES spectra.

- Spectral range must be of several hundred eV to cover XANES and EXAFS spectra if requested.

- Acquisition procedure consists in recording single-shot incident X-ray FEL spectra but also in acquiring a reference spectrum before the main shot and without the sample. This reference spectrum is obtained by averaging over several hundred shots beforehand with no sample, in addition to account for the shot-to-shot fluctuations of the X-ray FEL spectra on the sample. The signal-to-noise ratio is significantly improved by using such advanced analysis [53].

- An adequate analysis procedure must ensure that the incident and transmission spectra measured before and after the sample, respectively, are perfectly matched. The transfer function to match the incident and transmission spectra is defined with single shots without a sample and taken before the laser-pumped shot. The analysis procedure also includes the identification of the region of interest if needed.

- Accumulating shots and EXAFS measurements: We have demonstrated that accumulating ~ 5 single-shot measurements is enough to reach ~ 10% signal-to-noise ratio and to prevent effects from SASE spike fluctuations. Accumulating measurements over 10 to 20 shots allows a few-percent signal-to-noise ratio to be reached. In addition, EXAFS measurements can be performed by slightly varying the X-ray FEL energy to cover a larger spectral range. For that purpose, the X-ray FEL facility must provide a quick shift of the energy. The latter could be achieved by the vernier tool available at the LCLS.

SASE operation poses a challenge for XANES at X-ray FELs. At LCLS, the X-ray FEL was tuned (by electron bunch modifications) to avoid spiky features.

Accumulations (of order 300) on cold targets gave reliable spectra with two bent-crystal spectrometers. During the experiment, due to jittering laser parameters, the experimentalists needed to log P and T from VISAR data and later bin together similar target conditions. Ideally, XANES should be coupled to XRD to properly interpret the data. In addition, XANES needs reliable and homogeneous targets.

In a recent method development campaign at LCLS, Harmand et al. further optimized the setup and also tested a focusing setup (at the XPP beamline). A vertical dispersion direction was chosen to optimize the chirp of the LCLS X-ray FEL. Success depends on a complete alignment of the two spectrometers until the signal from the second crystal is gone. In few-µm focusing geometry, the second spectrometer needed to be flipped (detector pointing downwards). One could detect the Fe K-edge in single shots and obtain a high-quality spectrum after 30 shots. It became clear that control over the X-ray FEL focus is very important since you don't see what you probe and need to rely on hitting and probing the right spot.

7.4.2 Betatron radiation for XANES

by U. Zastrau

Betatron radiation could be an alternative approach for XANES studies in the future. This would require the HIBEF TW laser to be operational. The information from this short paragraph stems mainly from an oral discussion between Ulf Zastrau and Félicie Albert (LLNL).

A similar programme has meanwhile started at the Extreme Light Infrastructure (ELI) Beamlines facility in the Czech Republic, with first betatron results in 2016.

The expected photon number from a betatron source is comparable to the one of synchrotron sources in slicing mode, but with the added benefits that the betatron source is broadband and has short pulse duration.

The setup is realized by focusing an intense TW pulse with a long focal-length parabola into a gas-filled cell. The laser is typically focused using an off-axis parabola (OAP) with an *f*-number larger than *f*/7. In general, the focal length should be as long as possible (more than 30 cm from the gas cell is realized at the MEC instrument at LCLS).

As gas, commonly a mixture of 90% He and a few percent of N_2 is used (so-called ionization injection regime). A permanent magnet installed behind the gas cell can be used to monitor accelerated electrons, which typically have several 100 MeV kinetic energies.

Experimenters typically use an ellipsoidal grazing mirror to refocus the betatron radiation. The mirror is Ni-coated and operates at 3° incidence angle to the mirror surface. The spot of refocused betatron radiation had dimensions of 30×100 µm^2 FWHM, 16% RMS intensity, and no pointing jitter. The optical laser jitter to the X-ray FEL pulse is about 100 fs at MEC (LCLS).

A 200 TW laser with a few Hz repetition rate capability will reach betatron radiation with few keV photon energies. With this, one could extend XANES to lower photon energies than 5 keV, which is the limit when using the European XFEL for XANES.

7.4.3 Single-shot X-ray spectrometers at HED

by B. Chen and K. Appel

The high spectral resolution single-shot spectrometer (SSP) that will be used at the HED instrument is an online monitor for single-shot spectral diagnostics. The location of the SSP will be at the end of the HED optics (HED-OPT) hutch, just before the I_0 monitor, as shown in Figure 7.5. The spectrometer is based on ultrathin bent crystals. A defocusing geometry using convex crystals is used to gain high resolution. The actual design is compatible with the use of a diamond grating at the entrance of the optics hutch about 5 m upstream. In this concept, the direct beam passes to the experiment and the first- order beam will be used for the spectrometer. The grating can be implemented in the future and will be especially useful for the low energy range since it reduces the heat load on the spectrometer crystal and increases the transmission of the spectrometer. This is especially important for operation at more

than 10 Hz. Another ideally identical and symmetric spectrometer is also planned in the future that will be equidistant to the sample at the end of the HED experiment (HED-EXP) hutch.

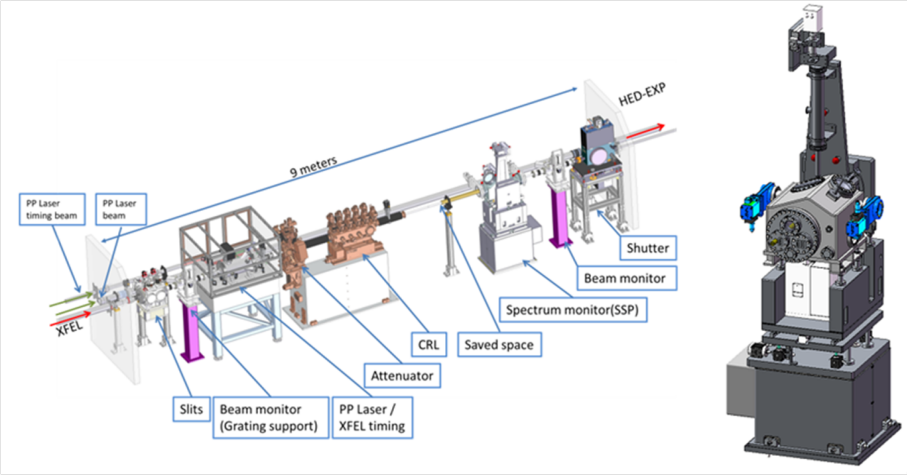

Figure 7.5: Overview of the HED-OPT hutch and 3D sketch of the SSP

For the design of the spectrometer, we need to satisfy the requirements of energy range, spectral coverage, and spectral resolution. The transmission should also be high so that most of the flux can arrive at the sample. The Bragg angles are set to vary in a small range for different crystals in order to keep the spectrometer compact. Four different cuts of ultrathin silicon crystals are needed to cover the whole photon energy range from 3 to 25 keV, as shown in Table 7.1.

Crystal	$2d$ [Å]	Energy [eV]	Bragg [°]	Transmission [%]
Si(111)	6.27	3.0–5.5	41.23–21.07	3–30
Si(220)	3.84	5.4–9.0	36.72–21.02	48–75
Si(400)	2.72	8.85–11.9	31.06–22.56	$>$ 80
Si(444)	1.57	11.7–25.0	42.53–18.44	$>$ 80

Table 7.1: Crystal orientations selected in the present design and respective approximate energy ranges and transmission

The spectral coverage depends on the beam size H on the bent silicon crystal, the curvature R of the crystal, and its lattice constant according to $\Delta E/E = \cot\Theta \times H/R \sin\Theta$. Since the spectral resolution will also be influenced by the radius of curvature (RoC) R of the crystal, the RoC is set to the small value of 200 mm. The spectral coverage is shown in Figure 7.6 for the spot size resulting from a focused beam and collimated with CRL1 (see Table 7.2). The crystals can be substituted by crystals with smaller RoC if larger spectral coverage is demanded in

Energy [keV]	Collimated with CRL1 [FWHM]		Focused with CRL1 [FWHM]	
	Spot size at 965 m [µm]	Divergence [µrad]	Spot size at 965 m [µm]	Divergence [µrad]
3	1285	3.652	275	1.350
4	1112	3.207	251	1.157
5	965	2.795	231	0.992
6	842	2.479	220	0.839
7	750	2.125	206	0.734
8	679	1.859	205	0.639
9	621	1.653	199	0.570
10	574	1.488	194	0.513
11	534	1.352	189	0.466
12	501	1.240	185	0.426
13	472	1.144	182	0.391
14	446	1.063	178	0.361
15	424	0.992	175	0.335
16	404	0.930	172	0.312
17	386	0.875	170	0.291
18	369	0.826	167	0.273
19	355	0.783	165	0.256
20	341	0.744	163	0.241
21	329	0.708	161	0.227
22	318	0.676	159	0.214
23	307	0.647	157	0.202
24	298	0.620	156	0.192
25	289	0.595	154	0.182

Table 7.2: Diffraction-limited spot size resulting from collimation or focusing with CRL1 at the location of the spectrometer

the future.

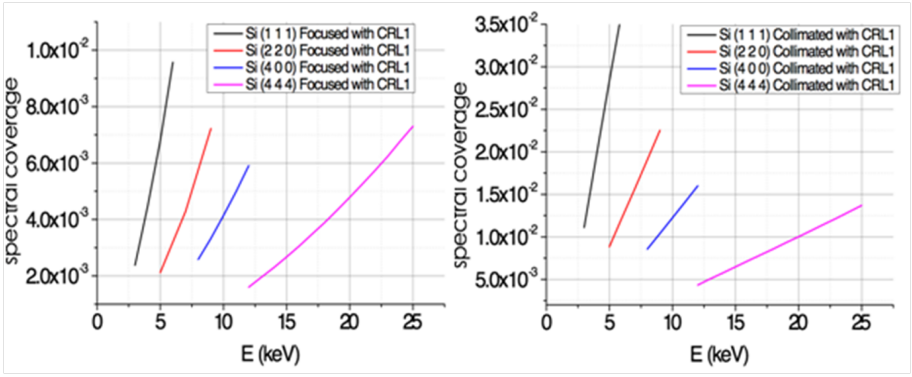

Figure 7.6: Spectral coverage of the spectrometer based on the chosen geometry. Left: Spectral coverage for a spot size focused with CRL1. Right: Spectral coverage for a spot size collimated with CRL1.

The spectral resolution of the spectrometer is determined by the geometry of the spectrometer and the diffraction-limited resolution of the crystal. The detector-limited resolution is influenced by the distance between detector and crystal and the pixel size of the detector. The pixel size of the detector is set to no more than 25 µm by using a Gotthard-II detector. The distance between detector and crystal is set to 850 mm. The diffraction-limited resolution depends on the curvature of the crystal and the lattice constant. The convolution of the detector-limited resolution with the diffraction-limited resolution results in the spectral resolution of the spectrometer as shown in Figure 7.7.

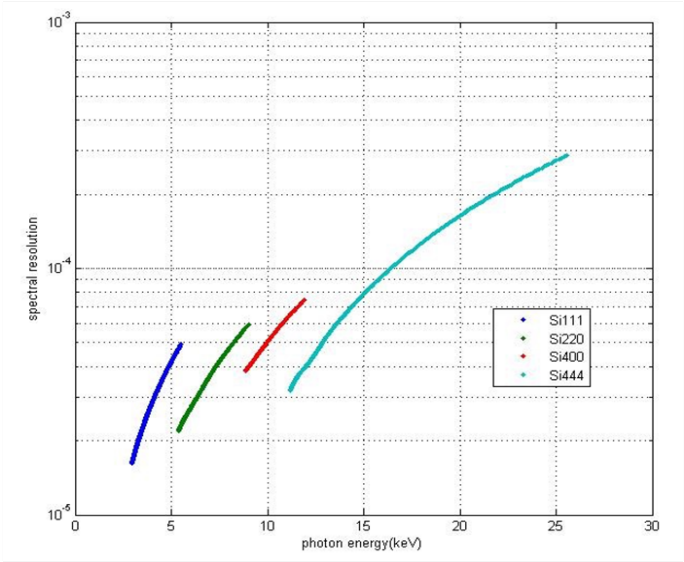

Figure 7.7: Estimated spectral resolution of the spectrometer in the present design

For the photon energy range from 3 to 10 keV, the spectral resolution of the spectrometer can be better than 5×10^{-5}. The spectral resolution is mainly limited

by the diffraction-limited resolution for the higher photon energy range. The spectral resolution of the system gets worse for high photon energies, especially for photon energies larger than 15 keV.

Two kinds of detectors will be mounted outside the UHV chamber on a rotating fixture coupled to a rotation stage. The Gotthard-II line detector, developed by Paul Scherrer Institute (PSI) in Villigen, Switzerland, with a pitch of 25 µm will be used for high repetition rates. It can be operated at up to 4.5 MHz. An optical 2D charge-coupled device (CCD) is planned to be used for low repetition rates. It will also serve to align the spectrometer to the Gotthard-II detector. The optical CCD consists of an YAG(Ce) scintillator, an optical lens, and a Hamamatsu ORCA FLASH4.0V2 camera. Two-dimensional spectra can be obtained using the optical CCD. Both the Gotthard-II detector and the CCD are mounted on a linear motorized stage on the rotation arm in order to easily allow either the Gotthard-II detector or the CCD to be selected for measurements.

Since the spectrometer is an online monitor, the X-ray beam will transmitted through the crystal and then propagate to the sample in the HED-EXP area. Attenuation and thus crystal thickness should be minimized. Silicon crystals with 10 µm thickness have been selected for the current configuration. However, even when using thin crystals, the transmission is very low in the low photon energy range. Additional problems are caused by the strong absorption of the X-ray FEL beam in the crystal and the related high heat load. One solution is to combine the spectrometer with a transmission grating. The grating unit is to be designed and mounted on the position monitor in the front of the HED-OPT hutch, which is about 5 m away from the spectrometer. In this concept, the direct beam passes to the experiment and the first-order beam will be used for the spectrometer. Diamond gratings with different pitches of 150, 200, and 250 nm are being considered, and the mechanical design of SSP has the capability to move in the x-direction (horizontally perpendicular to the X-ray beam) in a motorized way by at least 15 mm. A 150 nm pitch diamond grating will provide a first-order X-ray FEL beam at a distance of 4 to 13 mm between the first-order and direct X-ray FEL beam for the energy range of 10–3 keV, respectively. In this way, the SSP can be used to measure either the direct X-ray beam or the first-order diffraction beam.

7.5 X-ray emission spectroscopy (XES)

by K. Appel, K. Falk, and U. Zastrau

7.5.1 Science requirements

Even compressed solids are still optically undercritical and X-rays penetrate the bulk volume. Here, defined atomic transitions can be selectively excited by linear photoionization due to the X-ray FEL's monochromaticity and tuneability.

With the start of user operation at LCLS, the ionization of the K-shell in aluminium and neighbouring elements (1–2 keV photon energy) came into reach. Here, the lifetimes of K-holes are about an order of magnitude shorter (typically a few fs) than in the XUV-excited L-shell. They recombine by Auger and radiative decay. The corresponding characteristic emission spectrum from the latter process as a function of exciting photon energy is rich in information.

It was shown in Al at solid density at electron temperatures on the order of 100 eV (or 1 million K) that the electronic subsystem equilibrates on ultrashort timescales of a few 10 fs due to very high collision rates [157], establishing a local thermal equilibrium even within the typical X-ray FEL pulse duration. However, these states do not thermally emit any characteristic K-radiation since the K-electrons are much tighter bound (1.5 keV in Al). When irradiating similar states (plasma temperature $\ll$ K-shell binding energy), an X-ray FEL can be the perfect probe, since the signature of temperature is present in the modified screening, in the ionization potential of these levels, and in the altered population of the weaker bound outer shells [28, 27].

X-ray characteristic fluorescence is strong enough that spherically or toroidally bent perfect crystal optics can be used to image the plasma emission and allow experiments with few-µm spatial resolution. Imaging X-ray scattering has been demonstrated at large-scale laser facilities [51] and at LCLS [167]. However, the low scattering cross section can be overcome by using characteristic fluorescence instead [96]. Low-Z targets such as carbon could be doped by heavier elements, either homogeneously or arranged as tracer layers.

7.5.2 Proposed instruments

Using emission spectroscopy, one can determine temperature, ionization, and density through modeling of lines with atomic codes. Usually, bent perfect crystals in Bragg geometry (or Laue for high photon energies) are used. These offer improved spatial and spectral resolution compared to flat crystals but are more demanding with respect to alignment.

Thomson scattering spectroscopy suffers from a small cross section, therefore usually mosaic crystals are chosen. Here, one needs to take care that mosaic focusing is present (dimensions and distances must be correct). For crystals, highly oriented pyrolytic graphite (HOPG) and highly annealed pyrolytic graphite (HAPG) are good candidates. They can be either flat crystal, or bent one in von-Hámos geometry to improve the signal-to-noise ration.

The following X-ray methods require different choices of crystals:

- For low-resolution ($\Delta E \sim$ 6–10 eV), photon-hungry applications, mosaic spectrometers described in Section 7.7.4 can be employed. These are already planned to be fully implemented.

- Perfect flat crystals can be installed on a post and coupled to ePIX100 detectors in a flexible manner.

- High spectral resolution ($\Delta E <$ 1 eV) and/or spatially imaging crystals of cylindrical (Johann), spherical, and toroidal geometry can be installed on demand [155, 168, 167].

Time information might be lacking for integrating measurements. For slowly evolving plasmas, self-emission spectroscopy can gain from using temporal gating detectors. Recently, Sandia National Laboratories announced a fast framing camera with 2 ns per frame (UXI, [29]). This camera, called *Hippogriff*, is sensitive to both optical photons and soft X-rays up to $\sim$ 6 keV. When imaging X-ray scattering with perfect toroidal crystals is realized, a target that moves a few 10 µm over ns time scales (due to the ablation pressure) allows *streaking* of the X-ray scattering signal over time (different position of emission signal on stationary detector).

7.6 X-ray non-collective inelastic scattering (non-collectove IXS)

by U. Zastrau

A highly annealed pyrolytic graphite (HAPG) X-ray spectrometer in backscattering geometry will allow access to non-collective Compton scattering and recording of Compton profiles with few-eV spectral resolution. The moderate $\sim 5\,\mathrm{eV}$ spectral resolution allows the electron temperature and density to be inferred from Compton profiles.

7.7 X-ray collective inelastic scattering (collective IXS)

by U. Zastrau

Access to a variety of electron plasma parameters, ultimately to the dielectric function, is possible through the excitation of collective dynamics in the electronic subsystem [54]: in inelastic X-ray scattering, momentum transfer will couple to a free-electron plasma wave (rather than to individual electrons) when the probed length scale is larger than the Debye screening length. Here, the observed spectral feature is a red-shifted plasmon, whose shape gives access to the dielectric function, which comprises all transport properties such as collision strengths and rates, and conductivity. The spectral separation of the plasmon with respect to the elastic scattering is a direct measure of the free-electron density via the electron plasma frequency ω_{pe}. In particular, if further ionization does not not take place (next ionization energy $\gg$ target temperature), this can be a direct mass density measurement.

All measured X-ray scattering is completely characterized by the time-dependent (dynamic) structure factor, $S(k,\omega)$. Following Chihara's approach [25, 26] for simple metals, the total dynamic structure factor can be decomposed into contributions that describe near-elastic and inelastic scattering contributions separately:

$$Z_{\mathrm{A}} \cdot S(k,\omega) = \overbrace{|f(k)+q(k)|^2 \cdot S_{ii}(k,\omega)}^{\text{bound electrons}} + \overbrace{Z_{\mathrm{free}} S^0_{ee} \cdot (k,\omega)}^{\text{free electrons}} \underbrace{+ Z_{\mathrm{bound}} \int \mathrm{d}\omega' S_c(k,\omega) S_s(k,\omega-\omega')}_{\text{bound-free transitions (Raman)}} . \tag{7.1}$$

7.7.1 Plasmons

Here, the details of the second term in Eq. (7.1) are discussed. In a scattering event, momentum $\vec{p} = \hbar\vec{k}$ and energy $E = \hbar\omega = (\hbar k)^2/2m_\mathrm{e}$ are transferred to free electrons, which react with an oscillating motion. When thermal motion of the electrons is ignored, a displaced electron will oscillate with its plasma frequency

$$\omega_\mathrm{pe} = \sqrt{\frac{n_\mathrm{e} e^2}{m_\mathrm{e}\varepsilon_0}} \propto \sqrt{n_\mathrm{e}}. \tag{7.2}$$

In ambient aluminium ($Z = 13$), the plasma frequency is equivalent to an energy of $\hbar\omega_\mathrm{pe} = 15\,\mathrm{eV}$.

In a free-electron gas with temperature T_e, the electrons have a thermal speed of $v_\mathrm{th,e} = \sqrt{k_\mathrm{B} T_\mathrm{e}/m_\mathrm{e}}$, which generates internal pressure and thus a restoring force. Hence, the plasma oscillations with frequency ω and propagate with wave number k related by the **longitudinal Langmuir wave**:

$$\omega^2 = \omega_\mathrm{pe}^2 + 3k^2 v_\mathrm{th,e}^2 = \frac{n_\mathrm{e} e^2}{m_\mathrm{e}\varepsilon_0} + 3k^2 \frac{k_\mathrm{B} T_\mathrm{e}}{m_\mathrm{e}}\ , \tag{7.3}$$

called the **Bohm–Gross dispersion relation**. A plasmon is a quasi-particle that discretizes the Langmuir wave. Modes of this collective oscillation may be excited when the probed length scale $\lambda^* \sim 1/k$ is larger than the scale length λ_D for screening of electric fields, which can be expressed by the condition $(k\lambda_\mathrm{D})^{-1} \sim \lambda^*/\lambda_\mathrm{D} = \alpha > 1$.

In the collision-less **random phase approximation** (RPA), the plasmon shift is expressed by taking the expansion to the lowest order in the wave vector **k**:

$$\hbar\omega(\mathbf{k}) = \hbar\omega_\mathrm{pe} + \frac{\hbar^2}{m_\mathrm{e}}\alpha'\mathbf{k}^2 \tag{7.4}$$

where α' is the dimensionless dispersion constant with an RPA value of $\frac{3}{5}\epsilon_F/\hbar\omega_\mathrm{pe}$. Because of effects beyond the RPA, including inter-band transitions and many-body interactions, α' is often taken as a fitting parameter to experimental dispersion data.

7.7.2 Relation to WDM and dielectric function

In warm dense matter, the dynamic structure factor contains, as the spectral function of the electron–electron density fluctuations, further important information on the correlated many-particle system. The density fluctuations in the plasma, described by the dynamic structure factor, are related to the dissipation of energy, described by the imaginary part of the dielectric function $\varepsilon(k,\omega)$,

$$S(k,\omega) = \frac{\varepsilon_0 \hbar k^2}{\pi e^2 n_\mathrm{e}} \frac{1}{1 - e^{\hbar\omega/k_\mathrm{B}T_\mathrm{e}}} \operatorname{Im} \varepsilon^{-1}(k,\omega). \tag{7.5}$$

This quantity is, therefore, of paramount importance for the development of a consistent quantum statistical theory for strongly correlated systems. We note that the plasmon frequency shift $\Delta E_\mathrm{Plasmon}/\hbar = \omega$ can be approximated for small values of k using an inversion of Fermi integrals that results in a modified Bohm–Gross dispersion relation [54]:

$$\omega^2(\mathbf{k}) = \omega_\mathrm{pe}^2 + 3\mathbf{k}^2 \underbrace{v_\mathrm{th,e}^2}_{k_\mathrm{B}T_\mathrm{e}/m_\mathrm{e}} \left(1 + 0.088 n_\mathrm{e}\Lambda_\mathrm{e}^3\right) + \left(\frac{\hbar k^2}{2m_\mathrm{e}}\right)^2, \tag{7.6}$$

where $\Lambda_\mathrm{e} = h/\sqrt{2\pi m_\mathrm{e} k_\mathrm{B} T_\mathrm{e}}$ is the thermal wavelength. In Equation (7.6), the first term is a result of electron oscillations in the plasma, the second term represents the effect on propagation of the oscillation from thermal pressure. The third term includes degeneracy effects from Fermi pressure, and the last term is the quantum shift. The quantum shift and the electron oscillation terms are temperature-independent, and, for the partially degenerate plasmas of interest here, the thermal pressure is weakly dependent on T_e. Therefore, for small temperatures, no accurate knowledge of the temperature is required, and the plasmon energy shift provides a sensitive measure of the plasma electron density.

If the plasma is sufficiently hot (on of order of 10 eV and above), the scattered light can also gain energy $+\hbar\omega$ from an already populated plasmon mode. For an electronic system in thermal equilibrium, the balance of the up- and downshifted plasmon, $S_{ee}^0(\mathbf{k}, +\omega)$ and $S_{ee}^0(-\mathbf{k}, -\omega)$, are related via a Boltzmann factor:

$$\frac{S_{ee}^0(\mathbf{k},\omega)}{S_{ee}^0(-\mathbf{k},-\omega)} = e^{-\hbar\omega/k_\mathrm{B}T_\mathrm{e}}. \tag{7.7}$$

Damping. Generally, collisions will shorten the lifetime of the plasmon, yielding a broadened resonance frequency. Therefore, the plasmon *width* can be used to determine the plasma conductivity. This enters via conductivity models that are beyond the collision-less RPA. Weak collisions are treated in the Born–Mermin approximation, and other models can include local field effects and strong collisions.

Plasmons in semiconductors and insulators. Plasmons are also present in semiconductors and insulators. Electrons in a filled valence band may collectively oscillate by crossing into available states in the conduction band. The energy separation between the bands introduces an additional mode that couples to the longitudinal electron oscillation.

For a material with an initially empty conduction band, the plasmon will be centred at an energy shift of

$$\hbar^2\omega_p^2 = \hbar^2\omega_b^2 + \hbar^2\omega_{\mathrm{Penn}}^2 - \hbar^2\Gamma^2/4\ , \qquad \textit{with}\quad \omega_b^2 = \frac{N_b e^2}{m\epsilon_0} \tag{7.8}$$

with ω_b defined as the plasma frequency of the valence electrons. For example, for diamond at ambient conditions, $\hbar\omega_b$ = 31.1 eV, $\hbar\omega_{\mathrm{Penn}}$ = 13.8 eV, and $\hbar\Gamma$ is on the order of 10 eV [120]. This yields a plasmon energy of $\hbar\omega_p$ = 33.6 eV.

7.7.3 Requirements

7.7.3.1 Photon requirements

Experiments that entail observations of the complete plasmon spectrum in a single shot require powerful light sources. This requirement can be derived from the Thomson scattering cross section of $\sigma = 8\pi/3r_0^2 = 0.665\times10^{24}\,\mathrm{cm}^2$, with $r_0 = 2.8\times10^{15}\,\mathrm{m}$ being the classical electron radius. With about 1 mJ of X-ray energy and 10^{12} X-ray photons, using a scattering fraction of $n_e\sigma l = (1+\alpha^2) = 0.01$ yields 10^{10} scattered X-ray photons. There is no requirement for gating, and detectors with over 50% efficiency can be used, resulting in a comparable photon estimate of 10^4–10^5 photons. Distributed over, say, 10 spectral bins, the expected signal-to-noise ratio due to photon statistics will be 50–100, which is excellent. At X-ray FELs, these measurements can be performed with the additional advantages of greatly improved temporal, spectral, and wavenumber resolution. Such an experiment allows the electron temperature and density as well as the dielectric function to be measured, potentially in a single shot, which is essential for transient WDM samples prepared by high-energy lasers [47].

7.7.3.2 Probing the collective regime

In order to measure plasmons, several conditions have to be satisfied. In the target, the free-electron density yields a typical screening length. For ideal plasmas (hot and dilute), this is the Debye screening length $\sqrt{\frac{\epsilon_0 k_B T}{\rho e^2}} = \lambda_D$, on which the electrical potential from a local excess charge is screened to $1/e$. In an isotropic plasma, it is interpreted as a **Debye radius**. The Thomas–Fermi approximation is valid at constant chemical potential and low temperatures. Here, electrons act like the quantum-mechanical model of a free-electron gas, and $\lambda_{TF} = \sqrt{\frac{2\epsilon_0 E_F}{3e^2\rho}}$ is the Fermi–Thomas screening length. Since in a free-electron gas, the electrons are assumed to be non-interacting, the Thomas–Fermi approximation may be used only for low electron density, causing weak particle interactions.

In any case, this screening length has to be smaller than the probed length scale $\lambda^* = 2\pi/k$, where k is the momentum transfer in the scattering process. k itself depends on the X-ray photon energy E_0 and the scattering angle Θ by

$$k = \frac{4\pi}{hc} \cdot E_0 \sin\frac{\Theta}{2} = 1.013 \frac{E_0[\mathrm{keV}]}{\text{Å}} \sin\frac{\Theta}{2}. \tag{7.9}$$

Hence, if k becomes too large (high photon energies and/or large scattering angles), α will become smaller than unity and scattering will no longer be collective. A general impression of this range of temperature and densities is given in Figure 7.8.

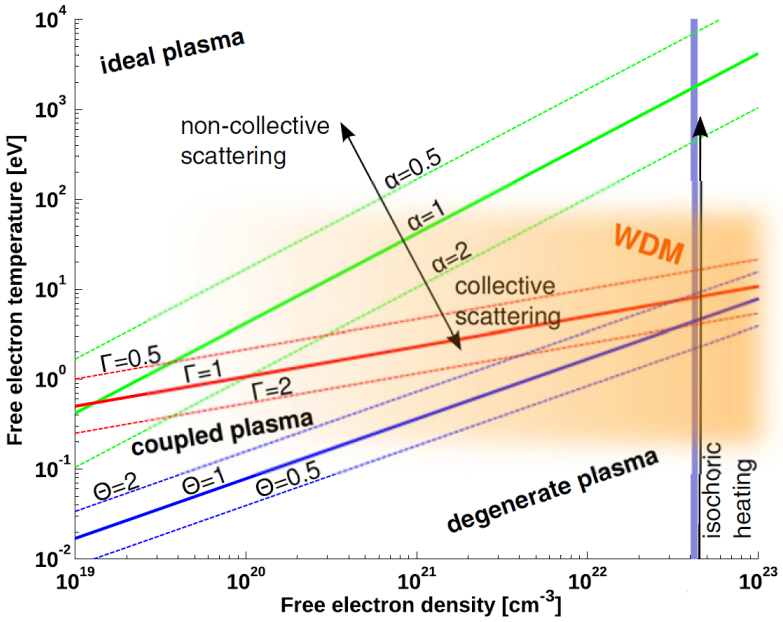

Figure 7.8: Phase space representation for the electron density n_e and the temperature T_e. Lines for the scattering parameter α, the coupling parameter Γ, and the degeneracy parameter Θ have been calculated according to Höll, Bornath, et al. [75]. The coupling parameter Γ is defined as the ratio of the Coulomb energy between two charged particles and the thermal energy. It divides the phase space between ideal ($\Gamma \ll 1$) or weakly coupled ($\Gamma \leq 1$) plasmas and strongly coupled ($\Gamma \gg 1$) plasmas. The degeneracy parameter Θ, which is the ratio of thermal energy and Fermi energy, divides the phase space into areas where quantum effects are of importance ($\Theta < 1$, degenerated plasmas) and areas where the role of quantum effects decreases ($\Theta > 1$). The densities of liquid hydrogen and the WDM regime are indicated. Through isochoric heating and the isentropic expansion, mainly the phase space in the collective scattering regime is accessible. Figure reproduced from Toleikis, Fäustlin, et al. [153].

For solid-density aluminium samples (3×-ionized metal), collective scattering has been studied using 8 keV photons at scattering angles ranging between 8° and 25°.

7.7.3.3 Spectral resolution requirements

For solid-density plasma conditions encountered in warm dense matter, Equation 7.6 results in energy shifts in the range of 15–50 eV, consequently requiring a high-energy X-ray source of $E > 3$ keV and $\Delta E/E = 10^{-3}$–10^{-4} to both penetrate through the dense plasma and resolve the plasmon frequency shift. Until recently, X-ray scattering experiments at X-ray FELs were only possible in SASE mode, having a spectral bandwidth of $\sim 3\%$, e.g. ~ 20 eV at 8 keV photon energy. It is evident that this performance will not allow the plasmon position and its shape to be resolved. It should be noted that simultaneous energy resolution of $\Delta E/E = 10^{-4}$ and wave number resolution of $\Delta k/k < 10^{-1}$ will be needed to resolve the plasmon broadening determined by damping processes in the plasma.

The European XFEL beam at the HED instrument, in seeded operation mode, will deliver approximately 10^{12} X-ray photons in a micrometre-scale focal spot, allowing measurements with a high spectral resolution of $\Delta E/E = 10^{-4}$, high wave number resolution of $\Delta k/k = 10^{-2}$, and high temporal resolution of 20–50 fs. Consequently, by employing highly efficient bent-crystal spectrometers [166] with 7–9 eV spectral resolution at 6–8 keV, the plasmon spectrum can be observed and resolved in a single X-ray pulse.

Regarding crystal spectrometers, mosaic spread leads to extraordinary integrated reflectivity as compared to perfect crystals. When the distances from the source and the detector to the crystal are equal, mosaic focusing ensures high resolving power [133]. Pyrolytic graphite crystals are easily manufactured to any shape. Nevertheless, the mismatch of the crystal substrate to the Rowland circle, focal aberrations, crystal inhomogeneities, and broadening due to deeply penetrating X-rays put these advantages into perspective [166]. HAPG, which has reduced mosaic spread compared to HOPG, has the benefit of higher resolution and aberration-less focusing when employed in X-ray optics. This material became popular among the community of high-energy density physics at both laser facilities and X-ray FELs [59, 44, 109].

Using the LCLS X-ray FEL operated in seeded mode, HAPG crystals [170] have been shown to enable plasmon scattering [46], but their energy resolution of $\Delta E = 9$ eV is still an order of magnitude worse than the seeded LCLS bandwidth (see Figure 7.9). A crystal with a matching energy resolution of ≤ 1 eV at 8 keV would allow the determination of the plasmon width and hence the collisionality through plasmon damping [107, 34]. Instead of using mosaic crystals, the use of perfect crystals would allow these energy resolutions to be achieved.

Recently, we presented a cylindrically curved GaAs X-ray spectrometer [154] with energy resolution $\Delta E/E = 1.1 \times 10^{-4}$ and wave number resolution $\Delta k/k = 3 \times 10^{-3}$, allowing plasmon scattering at the resolution limits of seeded X-ray FELs. It spans scattering wave numbers from 3.6 to 5.2/Å in 100 separate bins, with only 0.34% wave number blurring. The proposed spectrometer is superior to a mosaic HAPG spectrometer when the energy resolution needs to be comparable to the seeded bandwidth of 1 eV and a significant range of wave numbers must be covered in one exposure.

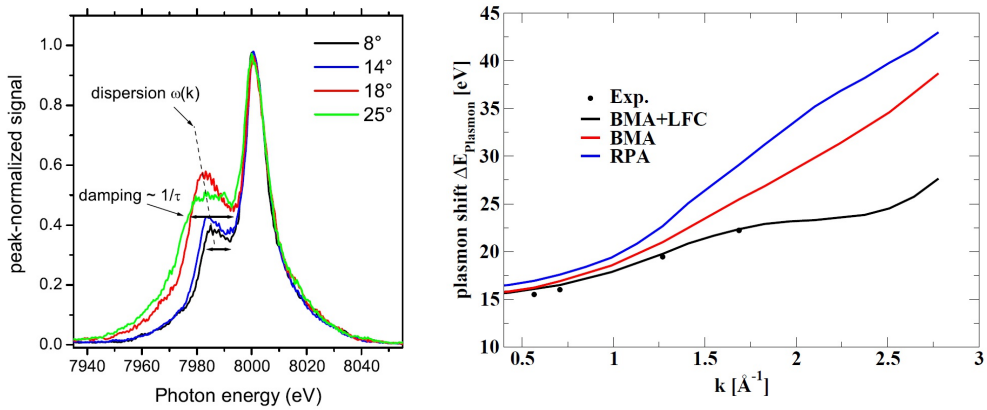

Figure 7.9: *Left:* Forward scattering data on cold aluminium resolves plasmons when using a seeded LCLS X-ray beam and a HAPG crystal. *Right:* Measured plasmon shifts (from central graph) together with the predictions based on different models (Exp: experiment, BMA: Born–Mermin approximation, LFC: local field corrections, RPA: random phase approximation). Courtesy Ph. Sperling.

In the context of high-repetition-rate and hence high-resolution plasmon scattering, it will now become possible to **distinguish between different models for the structure factor**. While the random phase approximation is a collision-less model, the Born–Mermin approximation accounts at least for weak collisions. The plasmon dispersion $\omega(k)$ is sensitive to local field corrections, but not to collisions. However, the plasmon width depends on collisional damping and can thus distinguish between collisional models. By measuring both the plasmon dispersion and width, we can select the appropriate model and hence precisely determine the collision rate and the local field effects.

7.7.4 Slim-HAPG von Hámos spectrometer

by U. Zastrau

At the MEC instrument at LCLS, the so-called XRTS spectrometers are used for inelastic X-ray scattering measurements. They were initially equipped with ~ 4°-mosaic HOPG crystals with about 7 cm width. It was found that this width leads to significant wave-vector blurring. While for SASE radiation its resolution is well adapted, it was not able to resolve plasmons. These require seeded beams (~ 1 eV bandwidth) and spectrometers made from ~ 1°-mosaic HAPG (resolution ~ 7–9 eV at 7–9 keV), which was demonstrated in 2013 [46].

In 2015, slim-XRTS spectrometers were successfully used in complex setups with spatial constraints. This design, while simple, worked well.

Figure 7.10 shows the details of the spectrometer design. A 50 µm thick HAPG crystal of dimensions 30 mm × 32 mm and with a radius of curvature (RoC) of 77.5 mm is used to focus the scattered X-ray signal in the non-dispersive direction onto a Cornell–SLAC hybrid pixel array detector (CSPAD), oriented in a von Hámos geometry to increase the collection efficiency. The 2015 spectrometer design was a fixed mono-angle spectrometer with an adjustable rail that can be moved, covering X-ray energies from 7 keV (280 mm focal length) to 4 keV (150 mm focal length). The spectral dispersion follows directly from the geometry and is calculated to be ~ 12.2 eV/mm at 5.5 keV.

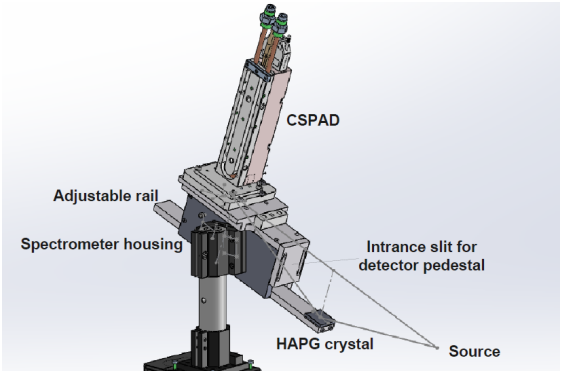

Figure 7.10: CAD model of the entire slim-XRTS spectrometer setup and configuration

Figure 7.11 shows a section cut of a further update of the spectrometer, implemented at LCLS. For the version to be implemented at HED at European XFEL, a spacer will allow the use of crystals with 50 mm RoC and 77.5 mm RoC. This allows the target–crystal distances for harder (7–12 keV) and softer (4–7 keV) X-rays to be kept in practical ranges of 100–300 mm, respectively. Also, flat mosaic or perfect crystals

could be installed later. The crystal should have a parylene blast shield towards the sample to prevent damage to the crystal by debris. Furthermore, the rail that defines the crystal–detector distance should be motorized. This changes the effective Bragg angle and hence allows the photon energy to be adjusted or changed during the experiment.

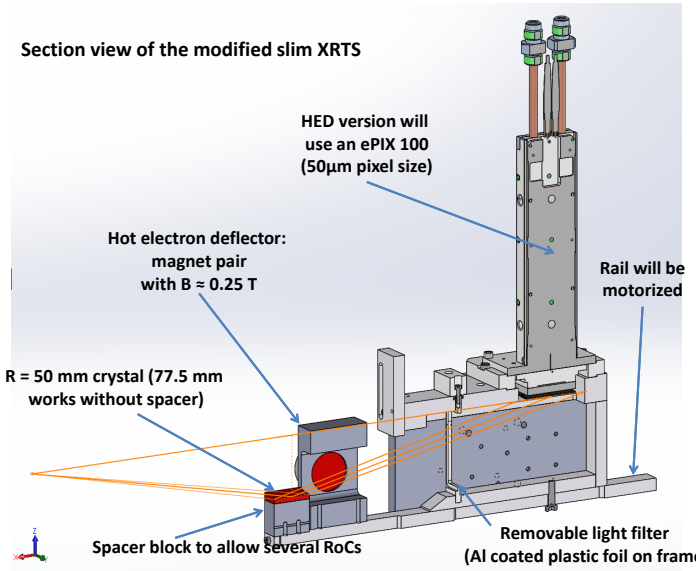

Figure 7.11: Cut through a proposed improved slim-XRTS spectrometer. Motorization not yet shown.

The spectrometer body will be weight-optimized and mounted in a high-precision laser mirror mount to allow its cylinder axis to be adjusted towards the interaction point. The body will be able to translate inside the mirror mount towards the target and parallel to the cylinder axis of the von Hámos crystal. The entire spectrometer will then be mounted in vacuum on the circular rails of IC1 (see Section 8.2). Discussion of these rails can be found in Section 7.8. This will allow scattering angles to be scanned in a reliable and automatized manner. After the design of the crystal mount has been optimized, it will be possible to reach scattering angles of a few degrees only, which is important for collective scattering (for details, see Section 7.7).

7.8 High-resolution inelastic scattering spectroscopy (hrIXS)

by K. Appel

It is planned to include an inelastic X-ray scattering setup at the HED instrument, that allows for measurements at an overall instrument resolution of approximately 25–100 meV. This setup will allow the ionic feature to be measured, which is especially interesting in warm dense matter states. These can be produced at HED with the help of the high-energy laser. The signal reduction of this technique is on the order of 10^{-6}. This tremendous reduction can in part be compensated by the use of a self-seeded X-ray FEL beam with a reduced energy bandwidth of 10^{-5}. Self-seeding is foreseen for an early stage of operation of HED, so the IXS setup can become operative from the beginning of HED operation. The envisaged repetition rate for the experiments is 10–20 Hz.

The aim for the energy resolution of the spectrometer is 25 meV. This is in accordance with the use of a high-resolution monochromator with an energy bandwidth of 10^{-6}. The monochromator has the functionality to reduce the bandwidth of the incoming beam by a factor of 10. To realize the IXS setup at such a high energy resolution, special specifications concerning sample geometry, analyser, and detector have to be considered.

7.8.1 Geometry in IC1

The geometry of the sample–analyser–detector arrangement in Interaction Chamber 1 (IC1) is planned to be a Rowland circle with a 1 m radius (RoC). To exploit the higher scattering in the vertical direction, when compared to the horizontal direction, the Rowland geometry will be realized in vertical geometry. In this geometry, the detector has to be placed in the plane of the sample in order to achieve maximum energy resolution. Two angular ranges for the analyser crystals are foreseen: The first position is in the forward direction at angles between 5° and 20° (see Figure 7.12). This angular range is planned to be motorized to enable changes without breaking the vacuum in the interaction chamber between the different scattering directions. The second position is planned for backward scattering, at about 140° (± 10°). This angle is not motorized, as the scattering changes only by 5% between 140° and 160°. So fine-tuning is not significant; we only want to measure the difference between the high- and low-theta angles.

It is planned to realize this geometry by mounting the analyser crystals on the vertical

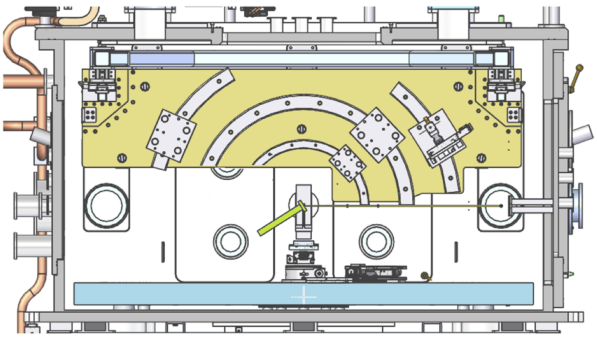

Figure 7.12: Sketch of IC1 in side view. The vertical breadboard (yellow, top) will be equipped with circular rails with three different diameters. The outer circular rail will hold the analyser crystals for the IXS setup. Two positions are foreseen: either in forward scattering geometry at angles between 5° and 20°, or in backscattering geometry at 140°. Up to two detectors (green) will be placed close to the sample.

breadboard on curved rails, which facilitate motorization and the realization of a distance of 1 m between sample and analyser (Figure 7.13).

To simultaneously measure forward- and backscattering, two detectors are required. The detectors need to be placed close to the sample (5 cm for an energy resolution of 25 meV) and thus be very compact. If it is not possible to have the two detectors close to the sample, the detector recording the backscattered signal should be the one placed farther away from the sample because the resolution at this geometry can be reduced compared to the forward scattering. The detector recording the forward scattering signal should be closest to the sample to achieve the best resolution.

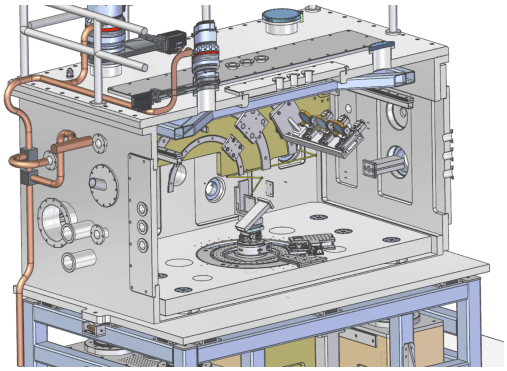

Figure 7.13: Sketch of IC1 in bird's eye view

7.8.2 Analyser

The choice of analyser crystal has been made already. The Si_{553} reflection was identified to be superior to the family of Si_{111} reflections because of several unwanted contributions in case that the Si_{111} is used. This problem was observed at an LCLS experiment where the fluorescence radiation from the sample and the bremsstrahlung were both transmitted by the crystal. Since the detector has no energy resolution, this noise adds on top of the signal of interest. Therefore, a dedicated reflection was selected.

7.8.3 Sample

Due to geometric constraints, the sample position cannot be changed in the horizontal direction. It will therefore be changed in the vertical direction only. This can be achieved with the generic sample holder. The possibility of 10 Hz operation with the fast sample changer requires a rather bulky sample stage environment.

7.8.4 Detector

The pixel size of the detector directly contributes to the overall energy resolution of the setup, which is given by the resolution of the monochromator, the analyser crystals, the detector pixel size, and the geometric arrangement of the spectrometer. Small pixels are advantageous, but the detector needs to be positioned at an appropriate distance to the sample so that one can profit fully from the small pixel size. Using Si_{444} and a pixel size of 50 µm, the detector can be placed at 100–200 mm from the sample in order to keep the energy resolution of Si_{444} of 60 meV in backscattering geometry. When using Si_{555} with the same detector, the detector has to be as close as 50 mm from the sample, to reach the minimum energy resolution of 25 meV.

To realize these constraints, the pixel size should be 50 µm and the detector should be mounted on a motorized translation stage, which allows for adjusting the distance to the sample and changing between different energy resolutions. The choice of detector is not finalized at the moment. Several detectors are under discussion for the HED instrument. The most promising for this application is the ePix detector with 50 µm pixel size, because of the small size of the pixels and the outstanding low noise level. The dynamic range of 100 was estimated to be sufficient for the application.

7.9 Planned detectors at HED/HIBEF

7.9.1 Detectors of HED baseline inside IC1

by S. Göde

The large interaction vacuum chamber (IC1) of the HED instrument provides sufficient space to host samples, large-aperture optics, X-ray diagnostics, and detectors. This offers a high flexibility to realize different experimental configurations but also to adapt the spatial resolution and angular coverage of the diagnostics, e.g. spectrometers and large-area detectors, to user needs. Any potential X-ray photon detector has to satisfy the key parameters given by the individual scientific scopes (some of them are discussed in this CDR) and the X-ray beam properties of the SASE2 beamline of the European XFEL. The overarching majority of experiments investigate dynamics processes following optical laser excitation, e.g. shock-compression and/or isochoric heating. The high-energy (HE) and high-intensity (HI) laser systems operate at 10 Hz. Many detection schemes, however, will make use of the unique bunch train structure of the European XFEL, which provides bursts of X-ray pulses at 10 Hz with an intra-bunch repetition rate of 4.5 MHz.

7.9.2 Description of the detector systems

The primary X-ray diagnostics and their detector requirements are listed in Table 7.3. Due to the relatively broad spectrum of possible detection schemes, multiple X-ray detectors need to be be employed, each having unique properties. In this respect, we may assign two detector categories: a) high dynamic range detectors and b) high spatial resolution detectors.

(a) For X-ray scattering experiments, the distance of the detector to the sample can vary between one metre and a few centimetres. Hence, medium-sized pixels of about 75 µm are considered to be optimal. Distant detector positions provide high q-resolution (SAXS, ptychography) while a position close to the sample provides large q-range coverage (XRD). The X-ray photon energies at SASE2 can be tuned between 3 and 25 keV. In particular for X-ray diffraction, the range between 9 and 25 keV is of high interest, for which the detector has to provide sufficiently high quantum efficiencies and good X-ray hardness. One of the key requirements for all scattering techniques is a large dynamic range greater than 10^3. The fact that some diagnostic schemes, such as SAXS and XRD, would profit from a central hole (for X-ray clearance) favours the buildup of large-area detectors from

multiple tiles/modules, allowing arrangements with (variable) gaps to be set up. Some scientific tasks, e.g. resolving shifts of individual diffraction lines, need the smallest possible pixel size. The question how many detector modules can/will be combined and in which geometrical arrangements is addressed in Section 7.9.3.

(b) For X-ray spectroscopy techniques (XAS, XES), smaller pixel sizes are more advantageous and single-photon sensitivity (low noise) for photon energies down to a few keV would be beneficial. In order to resolve inelastic features or a broadening of the elastic scattering (IXS), a high dynamic range and a high spectral resolution are needed at the same time. Depending on the spectrometer type, 2D area detectors as well as 1D strip detectors can be used.

The current detector plan foresees to provide a set of four different X-ray detectors, summarized in Table 7.4. All of them are state-of-the-art hybrid pixel detectors and each comes with unique specifications and capabilities. The concept at the HED instrument is to interchange and share single detector modules between different diagnostics or to combine multiple modules to large multi-megapixel area detectors of various sizes and geometries. In the following, each detector is introduced with its key specification parameters and capabilities.

The **ePix** detector series is currently being developed for LCLS and LCLS-II experiments by the detector department of SLAC in the USA. The detector family consists of two models, both of which have complementary characteristics. **ePix100** features a small pixel size of 50 m and a high signal-to-noise ratio with an equivalent noise charge (e.n.c.) of 290 e^- (RMS). This allows single-photon detection down to energies of about 2 keV. **ePix10k**, in contrast, provides a switchable gain and a high dynamic range (10^4 at 8 keV photon energy) at pixel sizes of 100 µm. The photosensitive area consists of silicon with 300 µm and 500 µm thickness for the **ePix100** and **ePix10k**, respectively. Whereas the **ePix100** is more suitable for spectroscopy (XES, IXS), the **ePix10k** will be used as an area detector for high dynamic range applications such as XRD and SAXS. The first **ePix100** detector modules have been tested and employed in first user experiments at LCLS [20, 14, 13] and will be available at the HED instrument starting from Day 1. Completion of a first full-frame prototype of the **ePix10k** is scheduled for the end of 2016. Depending on the detector performance, it might be available at the end of 2017 at the HED instrument of the European XFEL.

As a second high dynamic range detector, we plan to provide the **JUNGFRAU** (adJUstiNg Gain detector FoR the Aramis User station) detector, developed for the SwissFEL at the Paul Scherrer Institute (PSI) in Switzerland. **JUNGFRAU** is a hybrid pixel detector built for photon science applications at free-electron lasers

	Angular resolution [µrad]	**Pixel**	**Dynamic range**	**Central hole**	**Comments**
XRD (forward)	~ 500	$\geq 10^6$	High $\geq 10^4$	Yes	Single experiments could require all types (Bragg, powder, and non-crystalline scattering) because their requirements are different. In the Bragg case, the beam intensity needs to be reduced.
XRD (large q)	1000	$\geq 10^5$	Medium $\geq 10^3$	No	Diffraction at large angles (e.g. parts of powder rings), detectors close to sample.
SAXS	20–50	10^6	High $\geq 10^4$	Yes	Forward scattering inside vacuum.
XI	20–50	10^6	High $\geq 10^4$	No	Similar to SAXS requirements, but without central hole.
Spectroscopy	50–100	$\geq 10^5$	Medium $\geq 10^3$	No	Various types for different spectrometers. Using 1D detector enables fast readout.

Table 7.3: Table of detector requirements arising from scientific applications

and synchrotron light sources. It features a high dynamic range of 10^4 12 keV photons via a threefold automatic gain switching function. The sensor thickness of 320 µm thick silicon provides a spectral sensitivity of up to 25 keV. The pixel size is 75 µm and the detector noise (e.n.c.) is as low as 125 e^- (rms). Compared to the **ePix**, the **JUNGFRAU** features analogue storage cells, which enable on-chip capturing of 16 pictures with up to a 1 MHz frame rate. The opportunity to save multiple images within a single X-ray bunch train will be of great importance for many experiments in terms of signal-to-noise ratio and in-situ background subtraction, but also to probe conditions during dynamic compression cycles using DACs. The single-module sensor contains 500k pixel covering a sensitive area of 38.4×76.8 mm^2. For comparison, the **ePix10k** sensor size is 17.6×19.2 mm^2 accommodating larger pixels, which results in a lower digital resolution. The **JUNGFRAU** detector is in an advanced development stage. There exists a full-frame prototype, which has been tested under laboratory conditions and at synchrotron and FEL light sources. In those tests, which are published in [102, 139], the performance of the 2D detector has been demonstrated.

Gotthard-I is a 1D strip detector that comes with a pitch size of 50 µm and will be used for spectroscopic applications at HED where high dynamic range and high spatial resolution are indispensable. As in the **JUNGFRAU**, a threefold automatic gain switching achieves a dynamic range of 10^4 for 12 keV photons, while the noise is better than 300 e^- e.n.c. The application-specific integrated circuit (ASIC) is optimized for speed, allowing frame rates higher than 1 MHz, without compromising on linearity and noise performances. The maximum achievable frame rate with the present detector version, **Gotthard-I**, is 1 MHz, and the memory buffer for frame storage is currently limited to a maximum of 350 frames. A redesign, named Gotthard-II, is under way to make the detector able to run at 4.5 MHz and store all the 2700 pulses of a bunch train. Furthermore, the upgrade will feature a smaller pitch size of 25 µm. The new **Gotthard-II** version will not be available for Day 1 experiments at the HED instrument, but will become available to HED in 2018.

Commercial systems relying on charge-coupled device (CCD) area detectors for X-rays might be provided when pixel sizes below 50 µm are required. All X-ray detectors will be as compact as possible and operate under vacuum while fulfilling the vacuum requirements at HED ($< 10^{-5}$ mbar).

For the proposed ePix and JUNGFRAU detectors, the radiation hardness, the tolerance of heat waves from the DiPOLE100X laser ($\sim$ kW level), and the resistance to electromagnetic pulses (EMPs) from the laser–plasma interaction are not fully known. Initial experiments at MEC with an ePix100 located about 10 cm from the laser–target interaction zone, using counter-propagating pulses, did not show any

Detector	Specifications					Applications
	Pixel size [µm]	**Sensor size [pixel × pixel]** [mm × mm]	**Dynamic range**	**Noise e.n.c.**	**Repetition rate**	
ePix100	50	704 × 768 35 × 38	10^2 @ 8 keV	< 290	120 Hz	XRTS, XES, XRD, hrIXS
ePix10k	100	352 × 384 35 × 38	10^4 @ 8 keV	< 650	120 Hz	XRD, XRTS
JUNGFRAU	75	512 × 1024 40 × 80	10^4 @ 12 keV	< 130	2 kHz (ca. 1 MHz*)	SAXS, hrIXS, ptychography
Gotthard-I	50	1 × 1280 8 × 64	10^4 @ 12 keV	< 300	40 kHz (1 MHz**)	XES, XAS

Table 7.4: List of X-ray detection systems for HED on Day 1. * 16 images on-chip memory, ** 150 images on-chip memory.

negative effect to the detector. This might be attributed to an improved ASIC design of the ePix, which includes tungsten shielding in order to enhance EMP resistivity.

For both ePix and JUNGFRAU, the gain map for the switching is set and cannot be changed by the user.

7.9.3 Positioning of XRD detectors in IC1

by U. Zastrau

For XRD, the gain-switching detectors (ePix10k or JUNGFRAU) will be mounted in vacuum.

It is foreseen that three to four of these detectors can be combined in a frame with minimal gap between the tiles. These arrangements can be in the form 2×2 or 1×4, in an arc, L-shape, etc.—this has to be determined. The array of detectors should be movable in a spherical coordinate system with the interaction point as the centre. Change in the detector distance is seen as the least important parameter. However, change in the θ and ϕ angles should be foreseen. The detector arrays can be either mounted to the vertical breadboard, where the θ motion is already implemented in the motorized rails and only a left–right motion stage needs to be foreseen. The detectors can also be mounted on the horizontal breadboard, where a x–y–z or θ–ϕ–z stage

will be installed.

7.10 Detectors and detector bench of HIBEF

by A. Schropp

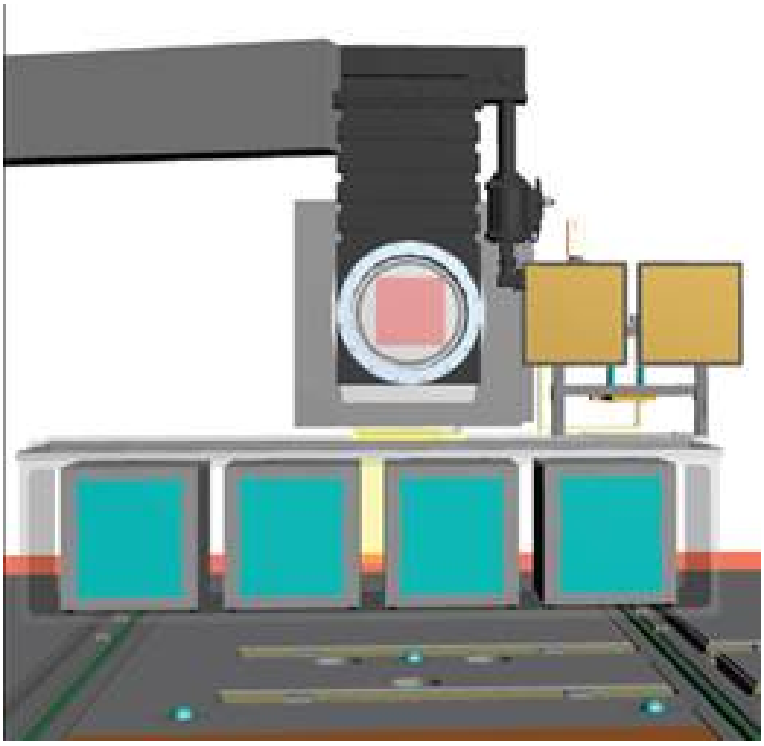

Figure 7.14: Draft CAD-drawing of the planned detector bench. On top of 4 racks (blue), the AGIPD (red denotes the sensitive chip area) and the PerkinElmer detectors (yellow tiles) are shown.

Detectors at the end of the HED hutch will be supported by a bench, which is movable along the European XFEL beam. It will be designed to support various detectors required for X-ray diffraction, spectrometry, magnified phase contrast imaging (PCI), or small-angle X-ray scattering (SAXS). The Adaptive Gain Integrating Pixel Detector (AGIPD) [70] will be implemented as a main detector for X-ray scattering, which can be operated at the full frame rate of 4.5 MHz of the European XFEL. Systems for data acquisition (DAQ) and infrastructure are planned to be installed under the bench. In Figure 7.14, a first CAD drawing of the envisaged setup is presented. Table 7.5 summarizes the specifications for detectors in Interaction Area 2 (IA2).

Detector	Specifications					Applications
	Pixel size [µm]	**Sensor size [pixel × pixel]** [mm × mm]	**Dynamic range**	**Noise e.n.c.**	**Repetition rate**	
AGIPD	200	1024 × 1024 205 × 205	10^4 @ 12 keV	350	5 MHz	XRD
PerkinElmer XRD 4343CT	150	2880 × 2880 432 × 432	? @ ? keV	?	15–85 Hz	XRD

Table 7.5: List of X-ray detection systems for IA2

8 Beam transport and dynamic compression geometries

The experiment area of the HED instrument (called HED-EXP) is split into two subsequent interaction areas (IA) along the X-ray beam.

The first interaction area (IA1) is designed in the framework of the European XFEL baseline instrumentation. The central part is a large multipurpose, all-aluminium vacuum chamber (Interaction Chamber 1, IC1). This chamber was designed in close collaboration with numerous international experts. Its rectangular shape and inner breadboard installations reflect the directionality and horizontal polarization of the incident X-ray FEL beam. This chamber was contracted to the Japanese manufacturer Toyama and will be delivered to the HED instrument in March 2017. The second interaction area (IA2) is designated to host additional target areas brought in by external groups. As a part of these installations, there exists a proposal to combine a diamond anvil cell (DAC) station and a laser compression setup in a second interaction chamber. The design of this chamber is foreseen to follow the one of the target chamber of the Dynamic Compression Sector (DCS) at the Advanced Photon Source (APS) synchrotron in Argonne, Illinois, USA. This chamber is described in detail in Section 8.3.

8.1 Floor stability

by U. Zastrau

The floor in the experiment hall of the European XFEL (XHEXP) has a Nano-E[1] stable floor. Figure 8.1 shows the vibration and movements at the location of the Single Particles, Clusters, and Biomolecules and Serial Femtosecond Crystallography (SPB/SFX) instrument (served by the SASE1 undulator) on a Sunday (where no civil construction was ongoing).

[1] VDI 2038-(2913) standard. For Nano-E, the root-mean-square (RMS) of the third octave spectra is below 0.8 μm/s per 1–5 Hz or 3.2 μm/s per 20-100 Hz. This is an extreme criterion for resolutions up to 0.2–0.5 nm, only achievable on extremely massive ground plates

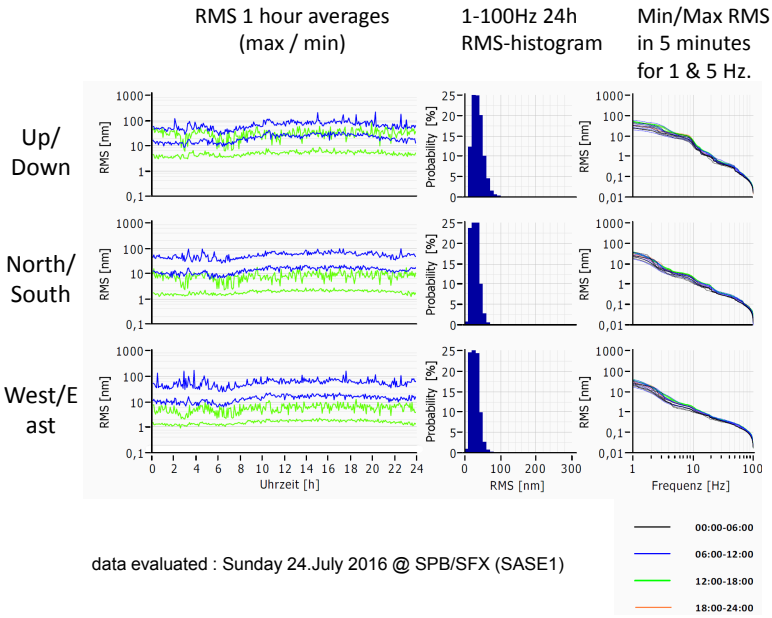

Figure 8.1: Vibration measurements in the European XFEL experiment hall on a Sunday in July 2016 (no civil construction ongoing)

8.2 Interaction Area 1: Large interaction chamber IC1

by I. Thorpe and M. Nakatsutsumi

8.2.1 Dimensions and layout of IC1

A side and top view with the major dimensions of the interaction chamber IC1 are shown in Figure 8.2.

8.2.2 Basic laser specification (summary from DiPOLE100X)

The following table summarizes the basic laser specifications of DiPOLE100X:

- Diode-pumped solid-state laser with multiple thin slabs of Yb^{3+}:YAG gain medium
- 1–10 Hz, bandwidth 2 nm, maximum about 100 J per pulse
- λ = 1030 nm or 515 nm (with reduced energy according to frequency conversion)
- 2 to ~ 15 ns duration, top hat or ramped

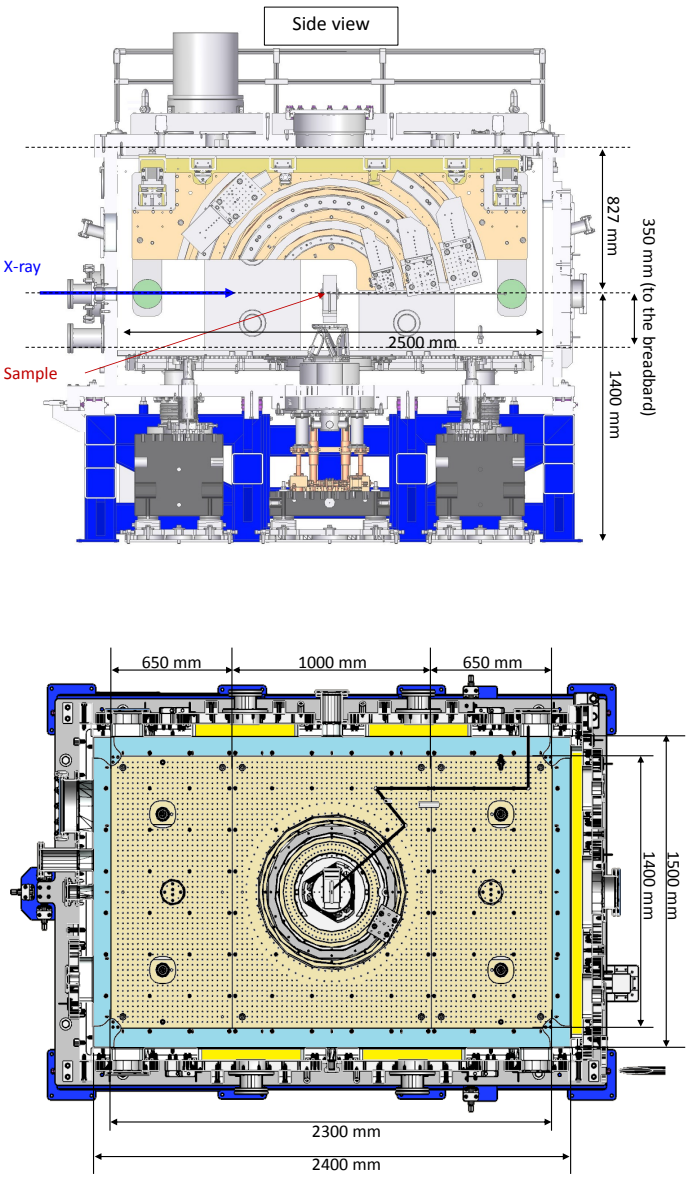

Figure 8.2: Side view (top) and top view (bottom) of the interaction chamber IC1 at HED with relevant dimensions

- Beam size after the final amplifier: 75×75 mm^2, square super-Gaussian shape, order 8 (see Figure 8.3)
- Polarization: perpendicular to the ground

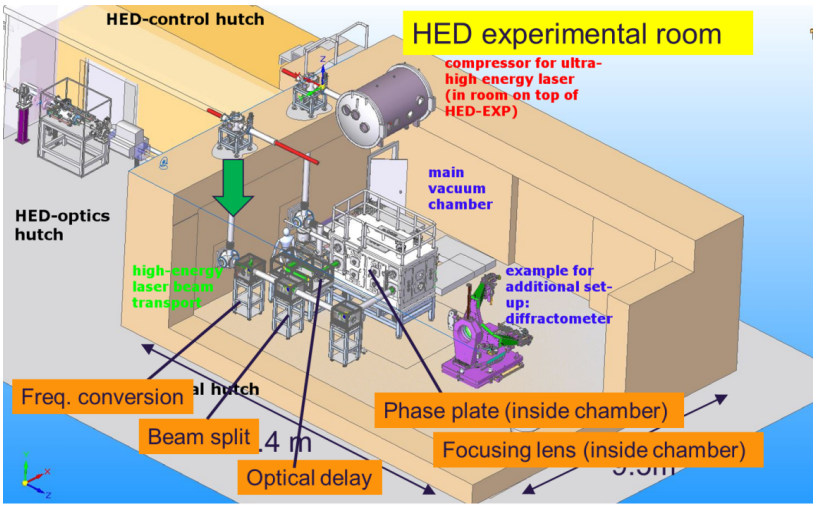

Figure 8.3: Overview of the HE-OL (DiPOLE100X) laser transport after the final amplifier in the HED-HPLAS hutch (laser room on top of experiment hutch, not shown). The drawing is outdated, but the rough location of each component is unchanged.

8.2.3 Laser beam transport to IA1

After the final amplifier, the laser beam is brought down to the HED-EXP hutch using two mirrors with 45° angle of incidence. The beam transport consists of a spatial filter, frequency conversion crystal, beam splitting, and optical delay before the beam enters the vacuum chamber. In the HED-EXP hutch, the beam is transported in the horizontal plane at 1400 mm above the floor, i.e. the same height as the X-ray beam. After the frequency conversion crystal, a beam splitter and an optical delay line are installed before the vacuum chamber, which enable the provision of two beams with variable mutual delay and angle of incidence on the sample. The maximum delay is ±1.6 ns (±50 cm). After the second-harmonic frequency conversion crystal, at least two dichroic mirrors are required to eliminate any unconverted fundamental wavelength (see Figure 8.4). When one uses the fundamental wavelength for the experiment, these mirrors will be replaced with high-reflectivity (HR) mirrors at the fundamental frequency.

8.2.4 Beam transport inside IC1

Figure 8.5 shows a top view of the high-energy optical laser (HE-OL) transport inside the IA1 vacuum chamber. The entrance ports are fixed. The angle with respect with the X-ray beam can be chosen among −20°, 0°, 20°, 45°, 70°, 90°, 110°, 135°, 160°, 180°, and 200°. The focusing lens has a focal length of about 500 mm.

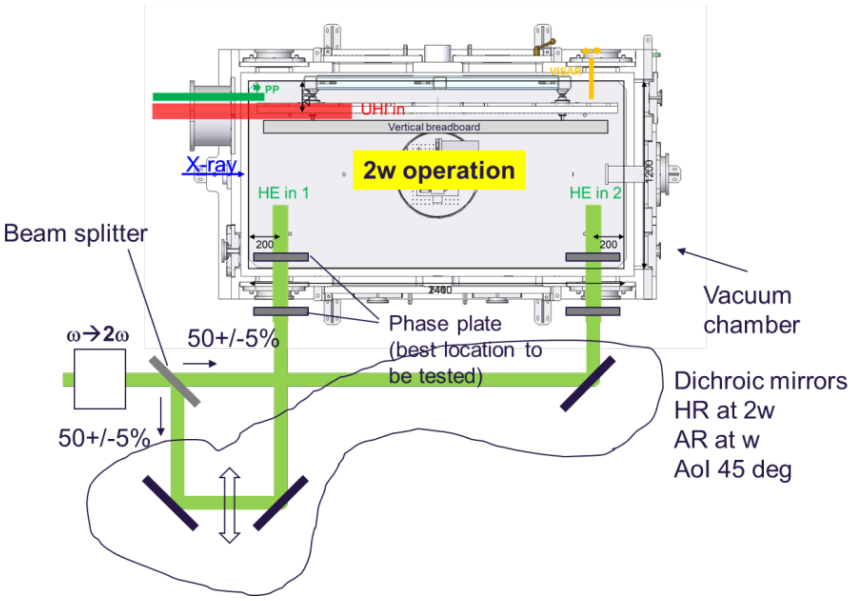

Figure 8.4: Top view of the ns laser in-coupling to the target chamber IC1

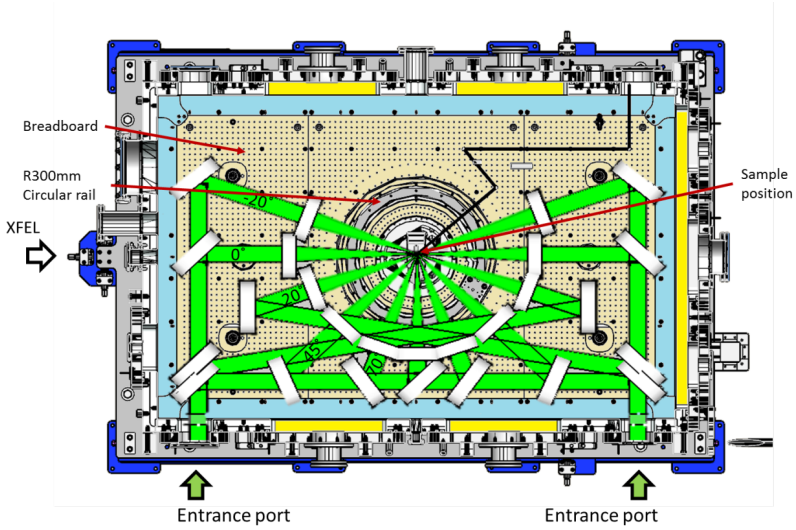

Figure 8.5: Top view of IC1 showing the possible beam transport geometries. The size of the beam and optical mounts are to scale.

The most frequent angles between the ns laser and the X-ray beam will be quasi-collinear and transverse geometry (see Section 3.2). In IC1, however, we are prepared for all other setups, for non-standard geometries, for split beams, in either co- and counter-propagating shock experiments.

Using the short-pulse 400 TW laser simultaneously with the DiPOLE100X ns laser is possible in IC1, but only with a limited number of angles between the laser beams.

The breadboard in the horizontal plane (see Figure 8.5) has a square M6 tapped-hole pattern of 25 mm pitch. The primary sample location is at the centre of the chamber. There is a $R = 300$ mm curved circular rail (un-motorized) on which the focusing optics can be mounted.

There is another breadboard in the vertical plane (see Figure 8.6). This breadboard can be used to mount X-ray scattering diagnostics, as discussed in Section 7.1. A curved rail with a motorized stage (see Figure 8.6 right) will be implemented and carry the spectrometer and the high-resolution analyser crystals. This breadboard is motorized in the north–south direction (up–down direction in Figure 8.5). The distance from the sample to the surface of the motorized stage can be chosen between 150 mm, 300 mm, and 410.5 mm. During the setup phase, one can bring the breadboard close to the entrance door, up to 359 mm from the sample in downward direction in Figure 8.5.

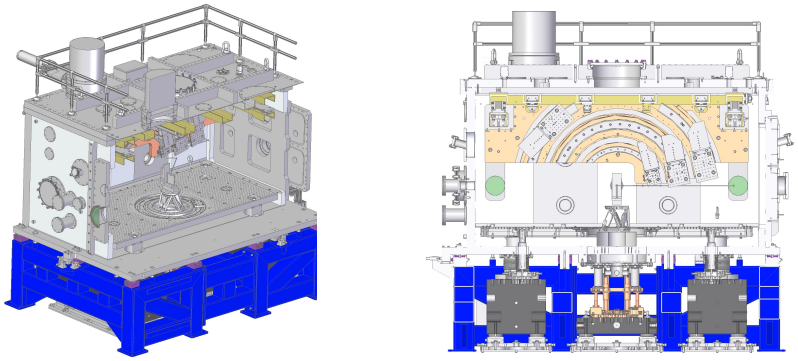

Figure 8.6: 3D (left) and side view (right) of IC1, showing the interior, in particular the horizontal and vertical breadboards with the curved rails on the latter

HED is currently prepared for DiPOLE100X operation with both 1ω and 2ω light in *s*-polarization, using slightly more expensive mirrors with a dual-colour coating.

8.2.5 Phase plates

To provide a uniform intensity distribution over space in the laser focus, phase plates are planned to be used. Top-hat profiles of 100 µm or 200 µm diameter are foreseen. The phase plate needs to be designed for a specific spot size, M^2-value, wavelength, and focal f-number. It will be placed before or shortly after the focusing lens. It should not be placed too far away from the lens, as free propagation smears out the phase

pattern created by the phase plate due to diffraction.

Phase plates should be located together with lenses in vacuum. With the DiPOLE100X, an M^2 of 3–7 results in 100% intensity modulation in the focus. HED should use a large beam and tailored large non-standard phase plates, e.g. 500 µm phase plates look promising with respect to granularity.

8.2.6 Optics size

The size of optical elements should be large enough to avoid beam clipping and diffraction from the edge, and it should allow for some alignment margins:

- The FWHM of the beam is 75 mm with super-Gaussian distribution (see Figure 8.7a). A beam size of 80 mm is used, which corresponds to 6% of the peak intensity at the edge of the beam.
- An alignment margin of 10 mm around the beam is considered.
- A clear aperture witch accounts for lower coating quality outside a 85% area.

The 80 × 80 mm^2 beam size, plus 10 mm alignment margin, plus 85% of clear aperture yields 120 × 120 mm^2 optic size for a 0° angle of incidence or a 150 mm diameter round optic. For oblique incidence (an angle of incidence between 35° and 55° is planned), 120 × 170 mm^2 optics will be used for (see Figure 8.7).

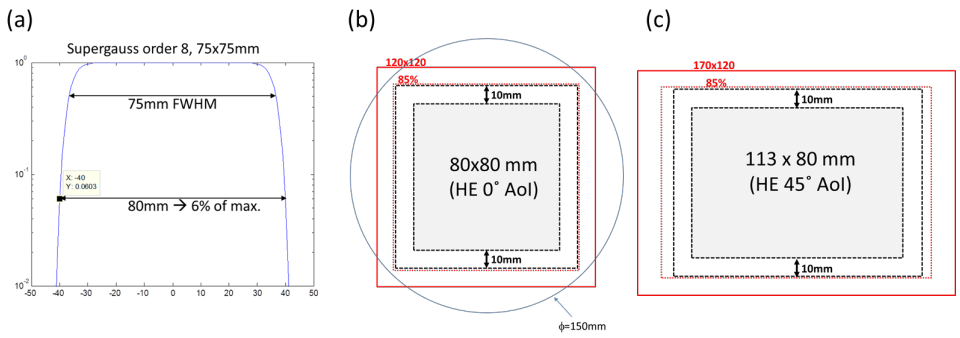

Figure 8.7: (a) Beam intensity line-out. The DiPOLE100X beam after the final amplifier has a beam size of 75 × 75 mm^2 FWHM with super-Gaussian profile. At 80 mm, the intensity drops to 6%. Necessary optic size for (b) 0° and (c) 45° angle of incidence. The grey shaded area corresponds to a 80 × 80 mm^2 size on the mirror.

8.2.7 Large-area detector for XRD

IA1 can also be equipped with a large detector. A second interaction point at the rear side of the chamber, close to the rear vacuum chamber door, is foreseen for this purpose. At the moment, there is no detailed plan; however, any large-area detector can be implemented by means of a re-entry flange, a vacuum pocket, etc. It is possible that the detector bench (see Section 7.10, including the AGIPD large-area detector) will be movable up to the rear side of IC1. It has to be pointed out that, when using the second interaction point, the DiPOLE100X laser can irradiate the sample only from the X-ray side, limiting the shock geometries.

When a proper mechanism is installed, a further option will be the use of a fast sample scanner to replace targets.

8.2.8 Sample scanner and robot inside IC1

by Z. Konôpková, M. Nakatsutsumi, and C. Deiter

A unique feature of IA1 is an integrated fast sample scanner capable of placing new targets into the laser beam at high repetition rates of up to 10 Hz. The challenge of using a high-energy laser in shock wave experiments is the relatively large distance between samples required to avoid damage to the neighbouring targets. Thus, the sample holder has to provide a large usable area to accommodate many samples and the speed to move to the next target between the two laser pulses.

The current design of the sample holder consists of a carrier frame whose outer shape is specific to each facility, laboratory, and/or instrument, and an inner sample frame that fulfils the requirements of the different samples and the specific types of experiments. The precision of the three translations that are performed by the sample stage should be better than 1–10 µm in all three dimensions. Moreover, the electronic devices and equipment within the target chamber and in the surrounding rooms are susceptible to damage and malfunction by electromagnetic pulse (EMP)–induced voltages. Due to the high electromagnetic fields generated by the laser–target interaction close to the sample, the electronic components of the sample stage have to be protected by shielding or located at a safe distance.

The sample frames will carry cartridges with an interior target area of $\sim 100 \times 100$ mm^2; the sample frame thickness is $\sim$ 6 mm (see Figure 8.8). The transfer arm thus replaces the sample frames carrying $\sim$ 100–300 solid targets onto a fast positioning stage inside the chamber. The frame will bear at least three reference marks, such

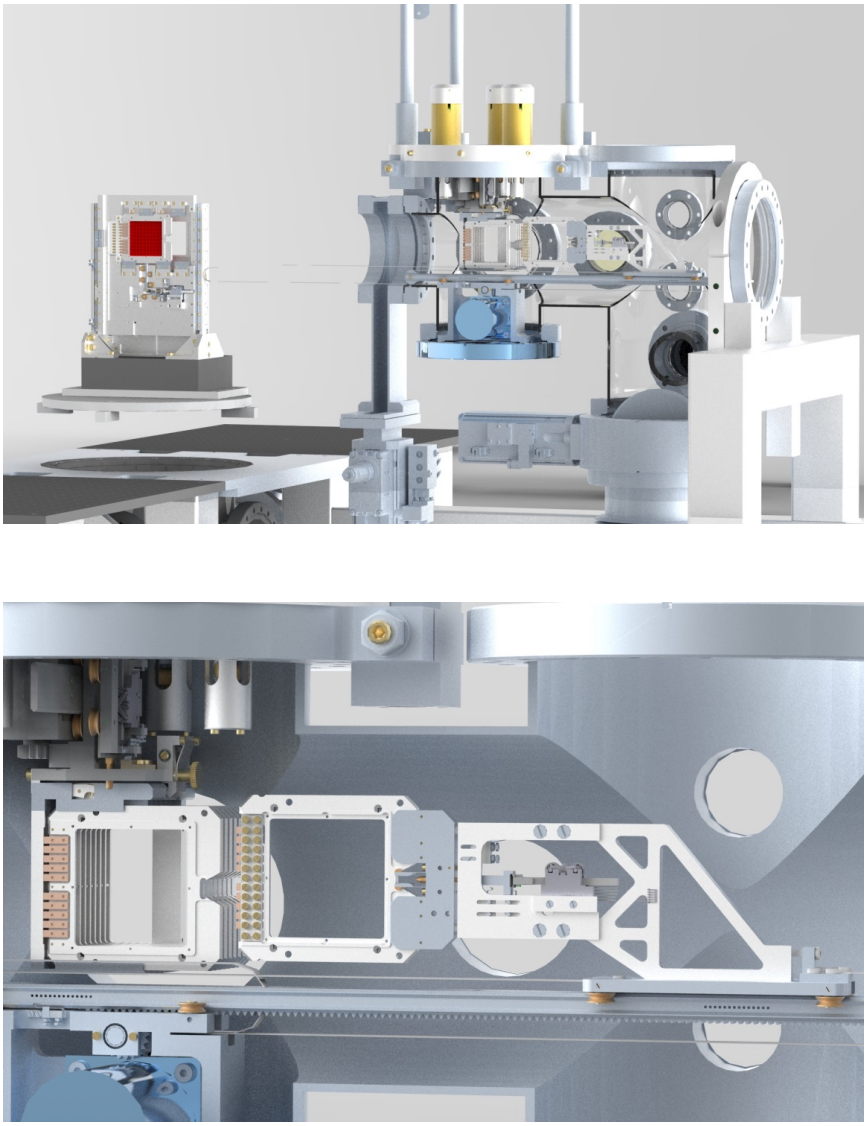

Figure 8.8: Sample changer design for the Spectroscopy and Coherent Scattering (SCS) instrument. *Top:* Transfer system chamber with sample frames and transfer arm grabbing a frame (right). A long-distance linear stage delivers the frame into the chamber (left). The transfer system chamber is mounted onto the first interaction chamber port from outside. *Bottom:* Sample frame mounted on the transfer arm. Cartridges with the targets (not shown) will be mounted into the frame. Current design by C. Deiter for the SCS instrument.

as a knife edge, pinhole, or fluorescence marker. The sample stage acting as a 2D raster device places the targets into the X-ray and laser interaction point with an accuracy of ~ 1 µm, at most 10 µm. The speed of the sample stage is specified to be 5 mm / 80 ms (start / stop, 20 ms dwell time). One frame with 100–300 targets at 10 Hz has to be replenished within some minutes. The transfer arm grabs the empty frame and replaces it with new frames from the cache. Up to 20 frames are ready to be delivered onto the fast scanning stage from the cache. The great advantage of this sample changer system is the possibility to change/replenish the targets without breaking the vacuum of the main interaction chamber.

8.2.9 Heat management

In full operation, the DiPOLE100X laser will deliver about 1 kW (100 J in 10 Hz) optical energy to the target. This power will heat up the mirrors and also the target mount. In addition, the chamber walls may heat up. The temperature evolution needs to be monitored, and action (such as active water cooling) should be taken after an initial evaluation and learning period. For X-ray optics such as large bent crystals or diced analysers, which are sensitive to heat expansion, a reflective thin heat shield (Al-coated mylar foil, etc.) should be installed.

8.2.10 Debris management

Shooting solid targets at a high repetition rate of several Hz with any laser system that generates plasma poses serious debris problems. Debris (atoms, molecules, fragments, or several µm-sized shrapnel) will ballistically fly from the interaction point onto any object.

In the case of ns laser ablation, this may be less shrapnel but small fast particles. These will coat laser mirrors, in particular the focusing optics. Debris will generate dust layers on rail systems and stages, and it will potentially damage detectors that are close by. Countermeasures have to be discussed and implemented. Detectors can be covered by parylene foils. Lenses and parabolas can be equipped with quartz plates. Debris may also coat neighbouring target foils with unwanted material if they are mounted in a close-packed array. This might alter their diffraction pattern and compression performance.

Jet targets from low-Z material that evaporate under ambient conditions do not pose these risks.

8.2.11 Exploration of liquid jet targets at HED in IA1

by S. Göde

The HED instrument is designed to prepare and examine extreme states of matter at high temperatures and internal pressures. In nature, such conditions can be found in outer space, e.g. in planet interiors, or they can be artificially created in inertial confinement fusion (ICF) implosions. Some of the most interesting materials in this field are e.g. water, methane, and hydrogen. To prepare the above-mentioned targets in high energy density states, new target delivery systems need to be developed. To this end, we explore liquid-jet and cryogenic-jet techniques, which have the great potential to provide solid-density matter that under ambient conditions exists in the gas phase. Liquid jets further supply replenishing targets, which, in light of the laser capabilities at the HED instrument, allow high repetition rate experiments.

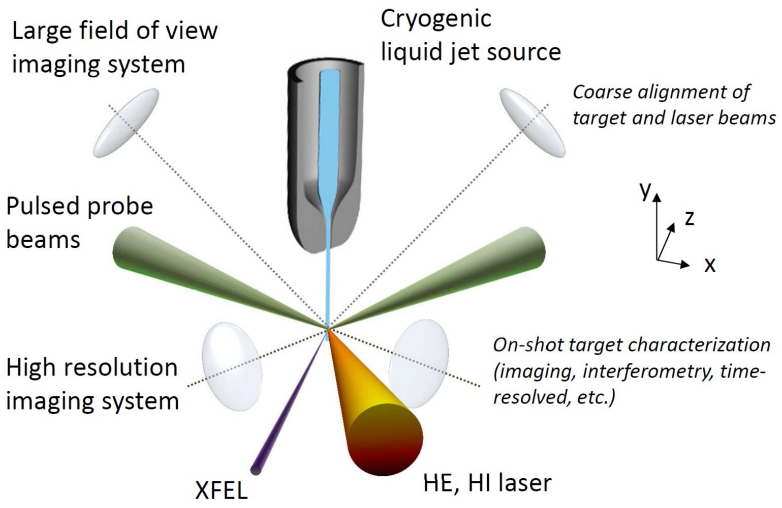

Figure 8.9: Schematic setup of a typical laser experiment using liquid microjets. Optical drive (HE, HI) laser and X-ray probe (XFEL) laser are indicated. One low- and one high-magnification imaging system are used for alignment tasks and for on-shot target and overlap characterization. A temporally delayed probe beam enables time-resolved studies (e.g. plasma characterization).

First liquid-jet experiments using cryogenic hydrogen have been successfully conducted at various laser facilities, including FLASH at DESY, LCLS at SLAC, and the Draco laser at Helmholtz-Zentrum Dresden-Rossendorf (HZDR) during the past years [169, 57]. From these, we learned that the reduced dimensionality and small size (in the micrometre range) of the target require sophisticated imaging and alignment strategies, as illustrated in Figure 8.9. A typical experimental setup makes use of one low- and one high-magnification imaging system, each having

two orthogonal visual axes. While the low-magnification imaging system is used for coarse alignment tasks, the high-magnification system determines the precise overlap between the laser locus and the target with highest spatial resolution. Using a pulsed light source (PP laser) further allows time-resolved plasma studies, e.g. interferometry, to be conducted on a shot-to-shot basis. In a typical high-power laser experiment, the laser focus is optimized at a fixed location. Hence, the interaction point is defined and the jet target must be positioned accordingly. Full 3D motion of the jet source is done by motorized translation stages or a hexapod system. Both allow positioning accuracies of below a micrometre. The mechanical integration of the source has to provide optimal decoupling from any vibration source. Strong energy absorption from high-energy (HE) or high-intensity (HI) laser pulses can cause significant disturbance or even damage of the source nozzle aperture through heat transfer or shock waves propagating along the jet axis. As a result, the nozzle–focus distance requires adjustment based on laser parameters and can vary between 5 mm and 50 mm. Depending on the mechanical setup, the nozzle quality, and the nozzle–focus distance, a pointing stability of the jet down to a few micrometres is feasible.

A typical layout of a cryogenic source assembly for hydrogen jets is shown in Figure 8.10 (a). The basic working principle of the source is described in Kim, Göde, and Glenzer [83]. Briefly, a temperature- and pressure-controlled liquid reservoir is fed by high-purity gas. A cryostat system controls the temperature, ranging from 3 K up to 400 K, with a few mK temperature stability. By adjusting the right temperature, a liquid accumulates inside the reservoir and leaves through a small, typically micrometre-sized aperture into the vacuum chamber. Under laminar flow conditions, a liquid jet is established, which may undergo Rayleigh–Taylor breakup into droplets within a few millimetres. On the other side, strong evaporative cooling eventually causes the liquid to freeze. Both processes are competing and finally determine the morphology of the target, e.g. volumetric modulations and surface roughness. Pictures of an operating liquid-hydrogen jet source providing a continuous-flow 5 µm jet are shown in Figure 8.10 (b).

Cryogenic jet operation requires vacuum conditions better than 5×10^{-4} mbar, above which thermal conductivity via residual gas molecules strongly affects the cooling efficiency of the cryostat. Typical velocities of the jet vary between 1 and up to 100 m/s, determined by the applied stagnation pressure and the viscosity of the fluid. Depending on the aperture cross section, the flow ranges from 10 to 1000 standard cubic centimetres per minute (SCCM). The gas ballast needs to be handled by high-throughput turbomolecular pumps having an accumulated total pumping speed of about 4000 l/s. Very high flows of up to 1000 SCCM can be realized by using a differential pumped catcher unit as a jet dump. Besides the cooling efficiency, the background vacuum level also has a significant impact on the long-term

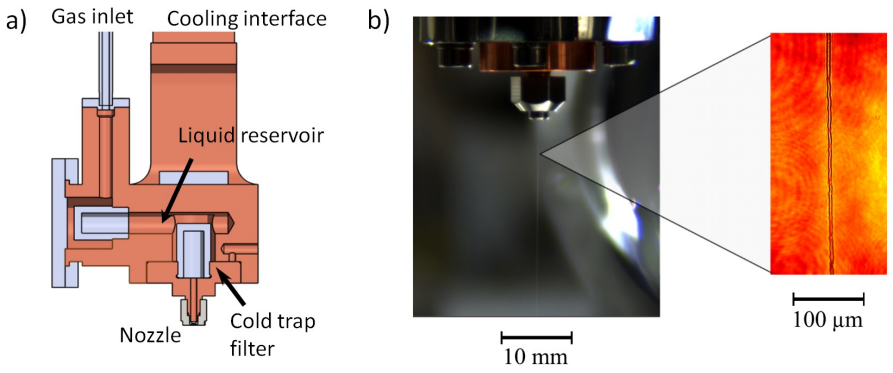

Figure 8.10: (a) Detailed view of a jet source. Figure reproduced from Kim, Göde, and Glenzer [83]. (b) Photograph of a cryogenic hydrogen microjet (centre) with corresponding microscope image (right).

stability of the jet target. Freezing of residual gas can cause ice formation close to the aperture, leading to a reduction of the effective aperture cross section. This effects the expansion dynamics and deteriorates the pointing of the jet over time. Online monitoring of the gas flow using mass flow controllers (MKS, Bronkhorst) will help to identify temporal changes of the effective aperture cross section during operation.

Size, shape, and stability of the jet are predominantly determined by the nozzle orifice. The surface quality in particular is of major importance since small kinks can cause turbulence to build up, which results in an unstable jet (spatial jitter) or even in a diffuse spray of particles with sub-micrometre size. Jets with circular cross section can be routinely generated with apertures made from glass capillaries or micromachined metal plates. Mechanically machined circular apertures made from platinum and iridium, also used for transmission electron microscopy (TEM) electrodes, are commercially available with diameters ranging down to 2 µm. The circularity is as good as 5% of the nominal diameter and the depth of the orifice is typically half of the diameter. Glass capillaries are widely used for water jet application and can be provided by the Sample Environment group (WP79) at European XFEL with customized diameters. For cryogenic application, metal apertures are favourable due to their physical properties, such as thermal conductivity and elasticity.

The apertures mentioned above are limited to circular shapes only. Dry-etching of layered silicon-based wafers, however, allows arbitrary patterns such as slit geometries to be produced. For some applications such as hydrogen, it is expected that, due to the strong evaporative cooling and consequent freezing of the liquid, the shape of the aperture is conserved, forming a planar *sheath-like* jet of solid density. By choosing different aperture geometries and aspect ratios, various widths and thicknesses can be realized. First tests using a $2 \times 20\,\mu m^2$ aperture with liquefied

hydrogen have demonstrated that this approach works in principle. Further tests with a more careful characterization of the jet shape and morphology will follow. We are also looking into other concepts, such as the colliding-jet technique and a modified gas-dynamic virtual nozzle (GDVN) design.

The large target chamber IC1 at HED is prepared for a jet source for both dynamic compression and short-pulse laser experiments. It provides a large top flange above the interaction region, the necessary viewports for inspection, and has sufficient turbo pumping power (~ 4000 l/s). The pumping power could be doubled if needed, since additional top ports are available.

8.3 Interaction Area IA2: Shock geometries and experiments

by J. Eggert, M. McMahon, C. Baehtz, A. Pelka, Z. Konôpková, G. Priebe, H. Damker, and H.-P. Liermann

8.3.1 Scope of a small vacuum chamber at IA2

The key idea behind the second chamber (see Figure 8.11) originates from the need for a small chamber that is optimized for standard X-ray diffraction experiments with large-area detectors to characterize the lattice behaviour of a material during compression with a laser shock or in a DAC.

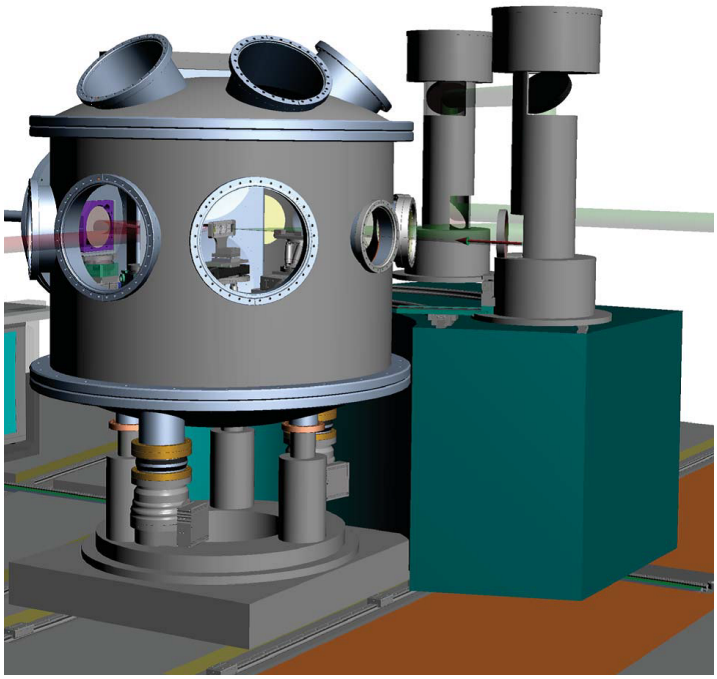

Figure 8.11: 3D representation of the vacuum chamber (IC2) for shock compression and DAC work at IA2

While the science case and the technical requirements for compression using a DAC have been discussed in detail in the CDR for DAC compression at the HED instrument, there is currently no equivalent comprehensive assessment for laser shock or ramp compression experiments in Interaction Area IA2.

In addition, there have been discussions on the merits of mimicking the laser compression chamber used at the Dynamic Compression Sector (DCS) at APS in order to achieve the highest synergy between these chambers, thereby enabling

analytical equipment and diagnostics developed for one chamber to be used at the other. Furthermore, it has become clear during the conceptual design of this chamber that shock compression in the IC1 and IC2 chambers will be complementary, enabling the full coverage of scientific questions proposed in Chapter 2 of this CDR. This will be addressed more fully in Section 8.4. Thus, the major strengths of the design of IC2 is the ability to dial-in a number of different shock geometries in a very short time through full automation of the DiPOLE100X laser and VISAR optics, requiring only small adjustments thereafter. Such a system will be outstanding among shock compression facilities at X-ray FEL and third-generation sources and other back-lighted laser shock facilities. It will reduce setup times significantly, enabling maximum throughput of experiments.

8.3.2 Shock compression geometries

For X-ray diffraction of laser-shock-compressed samples, the design team has identified two primary drive/diffraction geometries that are, and will be, important for future research in the field.

These geometries can be distinguished by the relationship of the incident X-ray beam to the laser compression beam:

- *Coplanar compression*
  The angle between the X-ray beam and the shock compression laser / VISAR is relatively small so that the shocked and un-shocked sample will be probed parallel to the shock direction.

- *90° compression*
  The angle between the X-ray beam and the shock compression laser / VISAR is close to 90° so that only the shocked portion of the sample will be probed perpendicular to the shock direction.

Based on these different requirements, a beam transport and focusing concept was developed, as displayed in Figure 8.12.

The basic features of this design are as follows:

- The focusing lenses and phase plates for the DiPOLE100X laser are placed outside the chamber, enabling focal distances of 700–1000 mm.

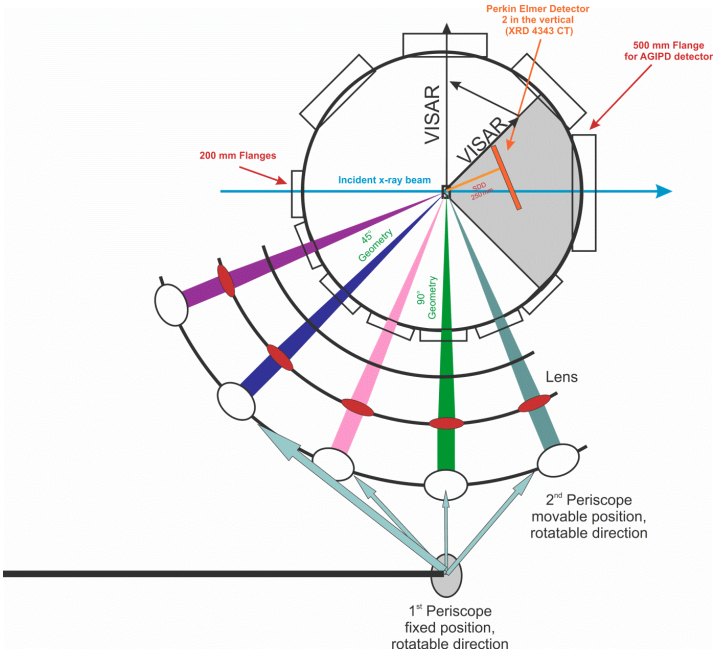

Figure 8.12: Different geometries of incident X-ray beam and shock compression in the IC2 chamber

- The DiPOLE100X laser will be guided to IC2 at angles of 22.5°, 45°, 67.5°, 90°, and 112.5° to the incident X-ray beam (counterclockwise), using a periscope that requires only four dielectric mirrors at 45° angles. Note that a geometry beyond 112.5° is not possible because the use of an AGIPD-type detector for DAC experiments requires a 500 mm flange. This large flange limits the space for an additional 200 mm flange on the downstream side of the vacuum chamber. In addition, the community requested that the AGIPD detector may be used for shock compression experiments at IC2 because of its single-photon detection capability. Because the detector sits on a detector bench, the HE laser may not be coupled into the chamber beyond 112.5°.

- The DiPOLE100X laser beam can be directly transferred from IA1 by removing the last downstream mirror.

- Because of the square nature of the DiPOLE100X laser beam, the windows in IC2 need to offer a 180 mm clear aperture, requiring the use of 200 mm flange windows. This results in a diameter of the vacuum chamber of 1200 mm.

Below, we describe the two most prominent geometries in more detail, using 3D CAD models worked out for the conceptual design in order to assess their feasibility.

8.3.3 22.5° geometry

The 22.5° geometry refers to the angle between the incident X-ray beam and the DiPOLE100X laser beam. In Figure 8.13, the VISAR and the target holder sit at an angle of 210° counterclockwise from the incident X-ray beam (FIXB).

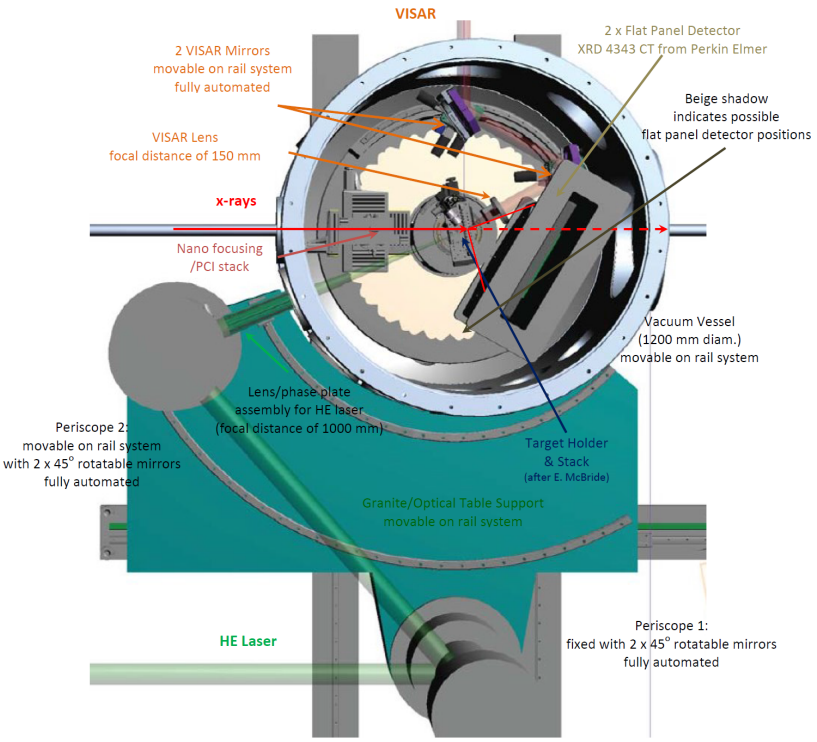

Figure 8.13: Top view of the 3D CAD visualization of the 22.5° shock geometry. There are four major components: high-energy (HE) laser, target holder, VISAR, and X-ray beam with area detector.

This will be the limiting VISAR position because, at 22.5° + 180° = 202.5° FIXB, the DiPOLE100X laser would be reflected back from the surface of the target and could damage the DiPOLE100X laser optics. Rotating beyond 210° FIXB does not make much sense because the VISAR lens would hit the X-ray beam. However, the target holder can move counterclockwise to change the angle between the target and the X-ray/DiPOLE100X laser setup (except for an angle range of ±10° at 270° FIXB where the VISAR mirrors would collide). The movement of the VISAR will be useful to change the centre of the flat-panel detector setup from 0° to almost 135° 2θ (backscattering geometry) in order to cover different q-ranges, e.g. for changing the q-range coverage from symmetric to asymmetric.

However, note that, when the scattering angle is reduced from 135° FIXB to smaller values, the linear polarization of the X-ray beam will result in a significantly reduced

scattered intensity in the horizontal plane, approaching zero scattered intensity at 90° FIXB.

Please note that the nanofocusing/PCI setup shown in Figure 8.13 is only a dummy and has to be fully developed during the preparation of the technical design report (TDR), because focusing at 25 keV will require some 300 lenses (see Sections 6.2 and 7.3).

8.3.4 90° geometry

The 90° geometry refers to the angle between the incident X-ray beam and the target (see Figure 8.14).

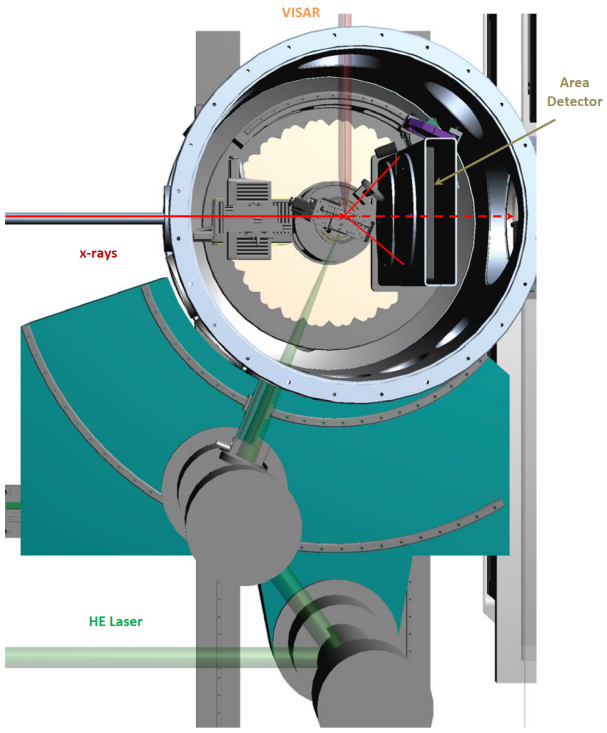

Figure 8.14: Top view of the 3D CAD visualization of the 90° geometry. As in the case of the 22.5° geometry, there are four major components: high-energy (HE) laser, target holder, VISAR, and X-ray beam with area detector.

Because of potential reflection of the DiPOLE100X laser from the surface of the target back into the DiPOLE100X laser, the optics could potentially be damaged. For this reason, the design team decided that the DiPOLE100X laser should enter the target chamber at an angle of 67.5°, for now. Most important for this geometry is that the target is located at 90° FIXB, so that one may image the shock front by phase contrast

imaging (PCI) or collect diffraction at different times of the shock propagation through the target.

An angle of 85° FIXB (close to 90°) might still be possible, but will require extra ray tracing and careful considerations so as to not damage the optics of the DiPOLE100X laser or the window of the vacuum chamber. Please note also that the target and the VISAR positions are fixed and always the same in the 90° geometry. Hence, no movement of the target/VISAR assembly is foreseen (which is also not possible since the VISAR comes in at an angle). In contrast, the centre of the area detector can be moved from −30° to +60° 2θ to explore different q-ranges.

Again, the limitation here is that, at scattering angles smaller than 135° and larger than 225° FXIB, the horizontally polarized X-rays in the incident X-ray FEL beam will result in a reduced scattering power in the horizontal plane, reaching zero at ±45° 2θ (i.e. no scattered intensity in the direction of the incident polarization vector).

Note that, in this configuration, the target holder is blocking some of the scattered diffraction, requiring a redesign of the holder during the preparation of the TDR.

8.3.5 Laser beam transport and beam quality monitoring inside IC2

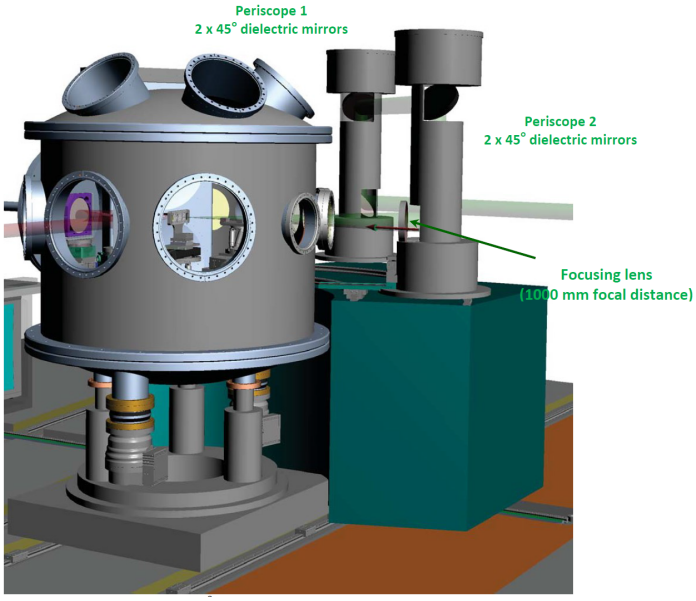

Figure 8.15: Periscope system for the co-planar 22.5° geometry with lens to focus the laser to IC2 inside the vacuum chamber. The focal distance is 1000 mm, resulting in an f-number of 13.3. In front of the lens, there is space for a phase plate.

As can be seen in Figures 8.13 ff., we propose to steer the DiPOLE100X laser beam

with a vertical periscope system towards IC2 inside the vacuum vessel. The periscope system consists of four 200 mm dielectric mirrors positioned at 45° each, with a damage threshold of 5 J/cm^2. Thus, these mirrors will be able to handle the 3 J/cm^2 pulses of the 100 J DiPOLE100X laser (1ω). The positioning of all four mirrors, as well as the periscope system itself, will be fully automated (mirrors with five degrees of freedom) so that the positions required for the various geometries can be dialed in easily. A focusing lens with a focal length of 1000 mm, as well as a phase plate, are placed at the end of the periscope system (see Figure 8.15). The *f*-number of the lens is 1000 mm / 75 mm = 13.3.

DiPOLE100X laser ray tracing has been performed by G. Priebe of European XFEL to eliminate any secondary foci that might lead to damage of the optical components of the DiPOLE100X laser (see Figure 8.16). The focusing lens sits on a translation system parallel to the DiPOLE100X laser beam so that one may defocus the DiPOLE100X laser beam to adjust the size of the focal spot. Table 8.1 shows potential foci that are likely to be used for the scientific experiments proposed in Chapters 2 to 4, as well as the possible use of phase plates.

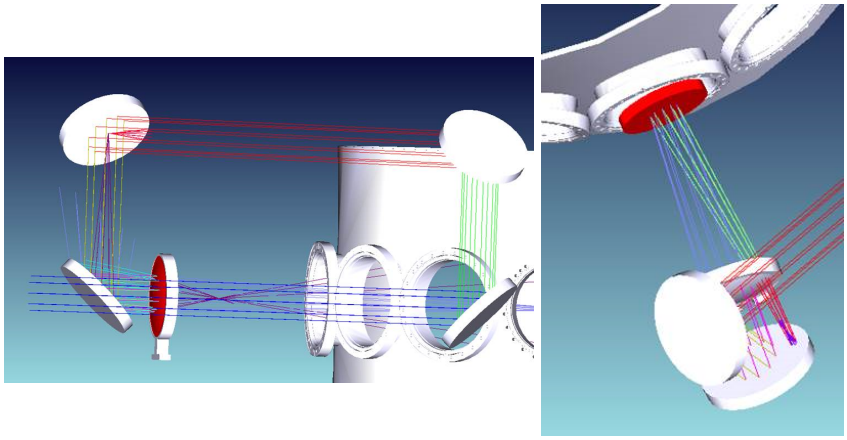

Figure 8.16: DiPOLE100X laser ray tracing to observe any possible secondary foci that might cause damage to optical components of the DiPOLE100X laser transport optics. Ray tracing was done by G. Priebe using ZEMAX. *Left:* Secondary foci expected from the focusing lens. In this simulation, the back reflection focus hits the second mirror of the last periscope setup. We have eliminated this interaction point by extending the length of the periscope. *Right:* Secondary foci produced by windows in the vacuum chamber. By tilting the mirrors by 10°, we will prevent the reflection focus from hitting any optical component.

We note that phase plates will most likely not offer a focal spot of less than 200 µm. Also, defocusing to a 400–800 µm spot size is not recommended because the waveform of the laser will not be well defined; thus, for these beam sizes, phase plates will be required. Technical details of the periscope and the focusing system will be worked out in detail in the TDR. The defocusing system may also be used to

employ a lens with a focal length of less than 1000 mm, such as 700 mm, potentially reducing the *f*-number to 700 mm / 75 mm = 9.3, if desired. However, for such a scenario, additional ray tracing will be required, as well as possible adjustments of the optical components of the periscope system, something that is foreseen for the TDR.

Not shown in Figure 8.15 is a system to monitor the beam quality, temporal profile, and power distribution of the HE laser. The latter might be determined through leakage from the first mirror of the periscope system, which will be straightforward to establish. Furthermore, it is foreseen that the focused beam may be monitored using the back reflection from the 10°-tilted windows of the vacuum vessel. These missing details will be worked out in the TDR.

	DiPOLE100X @ 1ω [µm]	**DiPOLE100X @ 1ω** [phase plates / µm]	**VISAR magnification** [field of view / mm]
Focused (diffraction-limited)	~ 27 (theoretical) 50–100 (real)	200 (minimum)	~ 20 (0.5)
5 mm defocused	400*	400	~ 10 (1)
10 mm defocused	775*	800	~ 10 (1)
50 mm defocused	3774	Not possible	~ 5 (2)
100 mm defocused	7522	Not possible	Not possible
200 mm defocused	15002	Not possible	Not possible

Table 8.1: Possible DiPOLE100X laser spot size achievable with the proposed setup when defocusing the laser or using phase plates. The VISAR parameters are matched to the different foci of the DiPOLE100X laser. *These shock laser foci might be rather inhomogeneous, and phase plates are preferred.

8.3.6 VISAR and IPEM

The overall VISAR system has been described in detail in Section 5.1. Based on this information, the laser beam for the VISAR in the 3D representations of Figures 8.13 ff. has been fixed to a clear aperture of 50 mm. In order to achieve optimal VISAR conditions, we set the focal distance to 150 mm resulting in an *f*-number of 3. Using a larger lens with a clear aperture of 75 mm, one might be able to increase the solid angle and reduce the *f*-number further. The magnification and expected field of view required for the different foci of the HE laser are summarized in Table 8.1. As illustrated in Figures 8.13 ff., the VISAR lens and mirrors inside the chamber offer five degrees of freedom and are completely motorized to dial in any possible VISAR position (limited by possible collisions) in a very short time, requiring only very little

optimization thereafter.

An in-plane equivalent monitor (IPEM) has been foreseen for the shock compression setup at IC2 (see Figure 8.17) in order to verify the overlap of the HE laser with the VISAR and the X-ray beam.

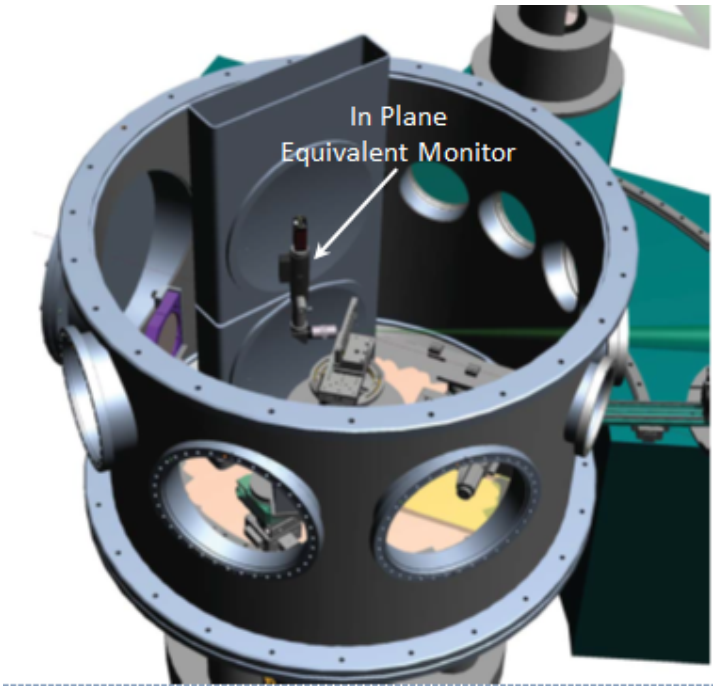

Figure 8.17: 3D representation of the in-plane equivalent monitor (IPEM) proposed for IC2. A Navitar zoom system with a Mitutoyo 10× objective is aimed perpendicular to the back side of the target. Currently, the proposed IPEM collides with the VISAR lens (not shown). Detailed discussion about the position and design of the IPEM will be continued during the preparation of the TDR.

The IPEM currently consists of a zoom body from Navitar with a Mitutoyo 10× objective. However, in the current setup, the microscope collides with the VISAR lens. It was considered to move the VISAR lens and the IPEM on the same rail system, alternating the viewing position of the back side of the target. However, to keep the VISAR system as stable and reproducible as possible, it was decided to leave the VISAR lens in place after initial alignment and calibration of the system. Thus, the precise positioning of the IPEM is a subject for the TDR. Nevertheless, priority is given to a position of the IPEM on the downstream side of the HE laser.

8.3.7 X-ray detection and spectroscopy

X-ray diffraction is the main analytical technique that will benefit from a dedicated IC2 with standard configurations that can be dialed in quickly with only minor adjustment of the laser optics, and with the ability to employ large-area detectors for detecting phase/structural changes and performing stress and strain analysis in shock-compressed materials (see Figures 8.13 ff.).

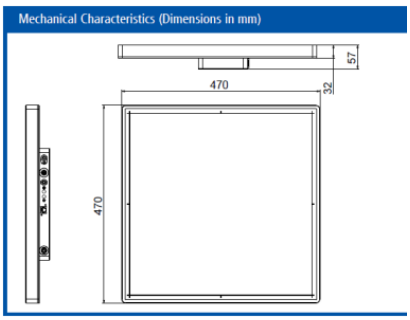

Sensor					
Panel	Single substrate amorphous silicon active TFT/diode array				
Scintillator	Direct deposition CsI:Tl or various Gd_2O_2S:Tb (Gadox)				
Pixel Matrix	2880 × 2880 @ 150 µm pitch				
Total Area	432 mm × 432 mm				
Electronics					
Amplifiers	Low noise ASICs with 6 user selectable gain settings				
ADC	16-bit				
Read-out Modes	Field of View (mm²)	Pixel Matrix	Binning	Pixel Pitch (µm²)	fps
	432 × 432	2880 × 2880	1 × 1	150	15
		1440 × 1440	2 × 2	300	30
		960 × 960	3 × 3	450	45
	288 × 288	1920 × 1920	1 × 1	150	20
		960 × 960	2 × 2	300	40
		640 × 640	3 × 3	450	60
	216 × 216	1440 × 1440	1 × 1	150	25
		736 × 720	2 × 2	300	50
		480 × 480	3 × 3	450	70
	432 × 216	2880 × 1440	1 × 1	150	25
		1440 × 720	2 × 2	300	50
	432 × 72	2880 × 480	1 × 1	150	60
		1440 × 240	2 × 2	300	85
Mechanical					
Size	470 mm (w) × 470 mm (l) × 57 mm (h)				
Weight	16 kg				
Housing	Aluminum with carbon-fiber entrance window				

Communications	
Data I/F	Fiber optical with PCIe 4x image processor
X-ray I/F	Integrated X-ray trigger control
Software	Support for 32 and 64 bit Windows® OS
Image Processing	
Real-time processing H/W	Compact PCIe 4x image processing board for host PC
Corrections	Offset, Gain, Bad Pixel
Imaging Performance	
Typical DQE (CsI)	76% (0 cy/mm), 60% (1 cy/mm), 44% (2 cy/mm), 32% (3 cy/mm) for RQA5
Typical MTF (CsI)	66% (1 cy/mm), 34% (2 cy/mm), 18% (3 cy/mm)
Saturation Dose (CsI)	80 µGy
Energy Range	20 - 225 kV (microfocus) Detector requires additional external shielding
Lag	< 2% 1st frame
Environmental	
Temperature	10 °C to 35 °C operating
Humidity	30 – 70% RH (operating, non-condensing)
Vibration	IEC/EN 60721-3 class 2M3 (10-150 Hz, 0.5 g)
Shock	IEC/EN 60721-3 class 2M3 (11 ms, 2 g)
Power	
Supply	100 – 240 VAC, 50/60 Hz, XRD-EPS Power Supply
Dissipation	25 W

Figure 8.18: Dimensions and parameters of the new PerkinElmer detector XRD 4343CT. Courtesy of PerkinElmer webpage.

Most important for diffraction is the fullest possible access to reciprocal space, with the fewest possible gaps in coverage, and the accurate measurement of the intensities of the scattered X-rays. This can be accomplished using large flat-panel detectors. Here, we propose to employ two new ScI-bonded amorphous-silicon detectors from PerkinElmer, e.g.. XRD 4343CT. This detector offers a relative large active area of 470 × 470 mm^2 with a very small rim for the readout electronics and a pixel size of 0.15 mm (see Figure 8.18) that can be read out at a frequency of 15 Hz. Compared for instance to the PerkinElmer XRD 1621 detector, this detector offers a slightly smaller pixel size (0.15 vs. 0.2 mm) and has a much better lagging behaviour (2% vs 8%). The readout rate is well matched to the maximum repetition rate of the DiPOLE100X laser. Since the primary X-ray beam has to pass through the detectors

to be absorbed in the beamstop at the end of the hutch, we propose to place two of these detectors on top of each other so as to let the primary beam pass, leaving only a very small area of reciprocal space that is not covered by the detectors (see Figure 8.19).

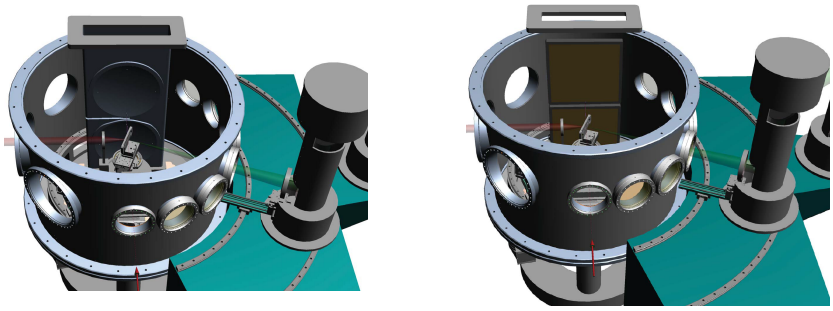

Figure 8.19: 3D representation of the detector setup for the 90° geometry (see Figure 8.14) consisting of two CsI-bonded amorphous-silicon flat-panel detectors of type XRD 4343CT from PerkinElmer.

Because the detectors are placed on top of each other, one can read a solid angle of almost ±65° 2θ with an uncovered area of ±7.5° 2θ (see Figure 8.20) e.g. for the 90° geometry described in Figure 8.14. In addition, in the horizontal plane, one can reach a coverage of almost ±45° 2θ, resulting in almost complete Debye–Scherrer rings of ±45°, which is essential for e.g. stress/strain and texture analysis of shock-compressed matter. Thus, at the highest X-ray FEL energy of 25 keV, the detectors will cover a q-range of up to 9.429 (horiz.) and 13.5 (vert.) $Å^{-1}$, as indicated in Table 8.2.

Unfortunately, the PerkinElmer detectors have to be operated in air, which means that they will have to hang in an air pocket from the top of the vacuum chamber and be protected by a vacuum window of aluminium or similar. When collecting diffraction images at an energy of 25 keV, the absorption of the scatted diffraction will not be significant, because the penetration depth at this energy is 2 mm. An aluminium layer has also the advantage that any parasitic low-energy scattering that might have been created through shock EMP of the shock will be blocked, as well as any debris from the disintegrated target.

During the *Dynamic Laser Compression* workshop with the community in September 2016, it became clear that, for studies of weakly scattering materials such as melts or molecular solids, it might be important to be able to use the GaAs AGIPD detector, which is capable of single-photon counting in high-gain mode. At the same time, the AGIPD can operate at lower energies than the PerkinElmer XRD 4343CT detector, i.e. below 15 keV. In order to be able to use the AGIPD, the formerly foreseen HE

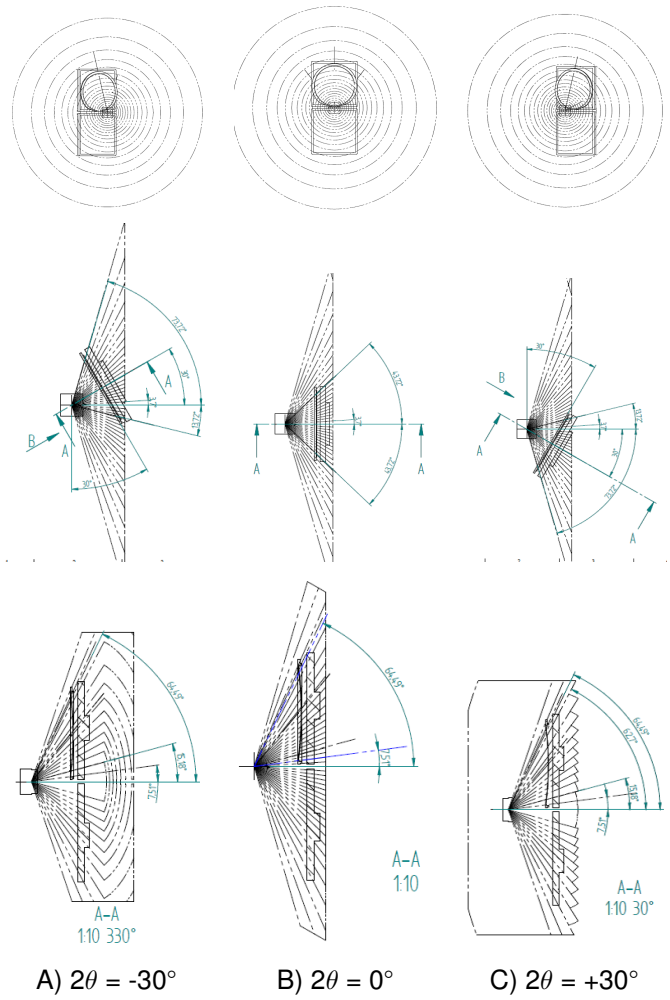

A) 2θ = -30° B) 2θ = 0° C) 2θ = +30°

Figure 8.20: 2θ coverage when the centres of the two XRD 4343CT from PerkinElmer are located at $-30°$, $0°$, and $+30°$ in 2θ. Diffraction rings are spaced by an angle of 3.7° 2θ.

Detector angle	2θ	d [Å] @ 25 keV	q [Å^{-1}] @ 25 keV
-30°	13.7°, -73.7° (H) ±64.5° (V)	2.079°, -0.414° (H) ±0.465° (V)	3.0°, -15.1° (H) ±13.5° (V)
0°	±43.7° (H) ±64.5° (V)	±0.666° (H) ±0.465° (V)	±9.429° (H) ±13.5° (V)
+30°	73.7°, -13.7° (H) ±64.5° (V)	0.414°, -2.079° (H) ±0.465° (V)	15.1°, -3.0° (H) ±13.5° (V)

Table 8.2: Expected coverage of reciprocal and real space at 25 keV with the proposed detector setup. H = in the horizontal plane, V = in the vertical plane.

laser geometry with an 135° angle FIXB will not be realized (see Figure 8.21).

Also, the AGIPD has the disadvantage that it is tiled, meaning that there are gaps between the different modules resulting in uncovered areas, an issue that users do not have to deal with when using the PerkinElmer XRD 4343CT detector. In addition, the coverage of reciprocal space will be limited to $2\theta \sim \pm 25°$ ($d = 1.146$ Å and $q = 5.483$ Å^{-1} at 25 keV).

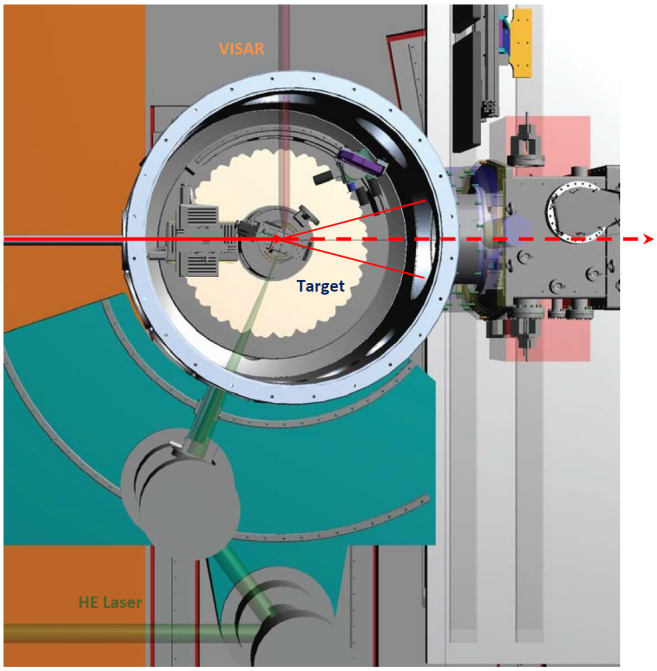

Figure 8.21: 3D representation of IC2 with the AGIPD detector attached to the chamber

8.4 Discussion of the validity of two setups for shock compression

by M. McMahon, J. Eggert, and U. Zastrau

There are two general types of laser experiments being proposed at the HED instrument, the first being attempts to reach maximum pressure, density, or temperature, often in the plasma state, by using a very high-energy drive either by tight focusing of a long-pulse laser or by use of a short-pulse laser. Diagnostics for such experiments tend to require maximum flexibility and multiple, specialized instruments. X-ray spectrometers at a wide variety of locations for inelastic scattering, large- and small-angle diffraction, and phase contrast or coherent diffractive imaging are measurements likely to be requested for every such experiment. The large interaction chamber 1 (IC1) of the HED baseline instrumentation has been designed with these experiments in mind.

The second type of laser experiment being proposed is more focused on materials experiments that involve the use of the long-pulse laser with carefully shaped pulses, very uniform spatial profile, and targets designed to keep the temperature as low as possible (near the isentrope) to study condensed-matter equation of state and material properties. Since every element or compound responds differently, the uncertainties ($<$ 1% in stress and density, and $<$ 10% in temperature) demanded by such experiments arise from the high quality of data collected in similar ambient and static compression experiments. The need for similar experiments to be performed on a wide variety of samples with high precision suggests less variety in experimental setups for the second type of experiment than for the first. This observation is based on the heavy use of standard configurations for long-pulse materials experiments at the MEC instrument at LCLS.

For example, since 2013, various groups have been performing diffraction experiments at MEC. These experiments were initially characterized by the fact that diffraction energies were low and detector coverage was limited. Placement of the detectors was constrained by the need to have the VISAR optics near the sample and by the layout of the other optical elements in the MEC chamber. A particular drawback was the fact that the pixel array detector (PAD) intensities collected in these initial campaigns were poorly characterized, and the backgrounds on the detectors were very high. However, there has been significant improvement at MEC, and diffraction data collected in 2016 were of excellent quality, significantly better than those collected previously. The angular coverage of the detectors was far greater, allowing much more information to be obtained from the intensities around individual Debye–Scherer rings.

Still, the configuration is not perfect: The low-angle cutoff of the detectors is large and will be a problem for samples where the observation of long d-spacing reflections is important. The coverage of the detectors has been greatly improved, but sizable areas of the diffraction pattern remain unobservable, and analyses have revealed that this additional coverage is vital to answering important scientific questions. The change-over between groups also takes more than 2 h each time—despite there being no movements of detectors, etc. This time is needed to re-optimize after wavelength changes, X-ray focusing changes, drive laser changes, and detector filtering changes.

Experience of using MEC over the last three years leads us to conclude that there can be a *standard* configuration for the great majority of X-ray diffraction experiments, and that the interleaved use of this setup by different groups will enable maximum use to be made of X-ray FEL beamtime. While the most recent MEC configuration comes close to this standard configuration, it has a number of shortfalls that can be

overcome by using different equipment, some of which may only work efficiently at the higher X-ray energies available at the HED instrument at European XFEL.

For the second interaction area at the HED instrument, intended for any additional flexible setups, the Interaction Chamber 2 (IC2) is envisioned to serve the needs of materials experiments as well as geophysical research.

The different goals of the two chambers are reflected in the proposed drive beam configurations (11 and 5, respectively) in Figure 8.5 for IC1 and Figure 8.12 for IC2. Unlike IC1, which makes use of many small, tiled PAD detectors that can be distributed widely (50×50 mm^2 in the case of ePIX or 75×75 mm^2 in the case of JUNGFRAU), IC2 incorporates a large, non-vacuum PerkinElmer detector in addition to the large AGIPD detector to cover a wide range of angles for standard wide- and small-angle diffraction or imaging experiments. While multiple ports in IC2 will allow custom diagnostics to be installed (even some diagnostics developed at other facilities, such as DCS at APS), the possibilities to accommodate custom-designed experiments are far lower than for IC1. We foresee that the large chamber, IC1, will be the workhorse chamber for custom experiments needing specialized diagnostics, targets, and setups, while the small chamber, IC2, will serve for high-throughput, largely standard-configuration, long-pulse laser materials experiments. An obvious advantage of IC2 is that it can be easily shared with static DAC experiments that use a very similar standard configuration. It is expected that the transition from static to long-pulse and back to static experiments could take place within a single shift.

We make several observations:

- IC2 is designed specifically for diffraction, optimized around the VISAR system.
- The beam transport optics for IC2 all lie outside the vacuum, making rapid small adjustments possible.
- The six 350 mm flanges on IC2 will allow experimenters to import diagnostics designed for use at DCS and employ them directly to IC2, enhancing the potential to benefit from the complementary nature of synchrotron and X-ray FEL radiation.
- IC2 will include large flat-panel area detectors, which enable accurate relative peak intensities to be collected over an intensity range of 1 : 1000 with high signal-to-noise ratio (low background).
- The photon energy for IC1 is optimal between 5 and 9 keV, which is not optimal for a diffraction setup. While the in-vacuum tile detectors

can reach the very high Bragg angles that are the result of using such long wavelengths, we do not believe that such wavelengths will be used for the great majority of materials diffraction experiments.

- The photon energy for IC2 is designed specifically for 15–25 keV in order to transmit X-rays through 10–20 µm of high-absorption material and to effectively filter the lower-energy ablation plasma. The large detectors on IC2 will enable wide angular coverage from very long to very short *d*-spacings for these higher-energy photons.

- The use of two interaction chambers will significantly increase the throughput of experiments at the HED instrument. In the off-shifts during the preparation of a new experimental configuration in IC1, we could insert a single shift of IC2 experiments. Since IC2 is designed primarily for standard-configuration experiments, most of the preparation for these experiments (such as target preparation) will be done in external lab space, and thus setup time in IC2 will be minimal.

- This rapid (30 min maximum) setup time will enable frequent changes between different user groups—enabling interleaving of experiments.

- The minimal transition time between static DAC and long-pulse IC2 experiments will further increase the throughput of experiments at the HED instrument.

- The pump cycle for the experiment chamber will be shorter for IC2 than for IC1, enabling more rapid cycling between different experiments.

IC2 (in the proposed design) offers great advantages as a standard diffraction setup (XRD) for diffraction of crystalline materials and phase transitions, at photon energies above 15 keV and coupled to VISAR. It allows fast change between fixed angles between the laser shock axis and the X-ray probe axis. If requested, non-standard experiments that involve other geometries (e.g. shocks that propagate towards the X-rays, or two counter-propagating shocks, or very specific angles), experiments at low(er) photon energies, and/or coupling with spectrometers will be performed in IC1.

IC2 provides a large-area detector (PerkinElmer) close to the target as main unique diagnostic. This is covered by a 1 mm aluminium window and is sensitive to photons above 15 keV. The potential to also couple the AGIPD for smaller scattering angle—alternatively or behind the PerkinElmer detector—was requested by the community. Currently, IC1 will offer only smaller tiled detectors (on the order of $50 \times 50\,\mathrm{mm}^2$ in the case of ePIX or $75 \times 75\,\mathrm{mm}^2$ in the case of JUNGFRAU), which

can be combined to a larger array and moved around motorized to scan and search diffraction rings. For IC1, a solution for an in-vacuum large-area detector was requested by the community and will be developed in future (PerkinElmer in a vacuum pocket, or a scintillator-based solution).

IC1 also offers other, off-centre interaction points (on a breadboard-decoupled post if needed). This could be a position close to the rear wall of the chamber, and the detector bench with PerkinElmer detectors and the AGIPD can be brought close to this rear wall.

The design of IC1 reflects the horizontal linear polarization of the European XFEL radiation. Therefore, IC1 is equipped with motorized rails with about 1 m radius mounted on a vertical in-vacuum breadboard, to mount area detectors as well as spectrometers in vacuum. This allows the study of XRD with tiles at higher angles (meaning higher dispersion and higher sensitivity), X-ray emission spectroscopy, ion-acoustic modes using diced analysers (length along the X-ray beam is 2.50 m) and electron-inelastic (plasmon, Compton) scattering. Both inelastic scattering experiments (ion-acoustic, plasmon) typically need to scan the scattering angle to measure the dispersion relation. Also, the photon energy for inelastic X-ray scattering is optimal between 5 and 9 keV, which is not optimal for a dedicated diffraction setup. However, if XRD is employed at these *low* photon energies, the diffraction peaks will lie further out (at higher angles) and the in-vacuum tile detectors are optimized to detect these with high resolution (due to small pixels). Regarding other X-ray techniques, IC1 should be chosen for SAXS, PCI, and point-projecting techniques with a sub-micrometre focus, since IC1 offers the largest distance from the interaction point to the detectors.

It is planned to install a cleanup slit system right in front of both IC1 and IC2.

IC1 also offers a symmetric distance to the two planned bent-crystal spectrometers to perform XANES measurements with converging/diverging beam. IC1 has a sample robot implemented and allows operation without opening the interlock of the hutch or breaking the vacuum for many hours, ensuring long operation cycles. It was discussed that a similar solution should be implemented in IC2 if the system proves to be beneficial.

Regarding fast change-over times, it has to be ensured that the combination of IC1 and IC2 (and in particular the DiPOLE100X laser transport towards the two chambers) is designed jointly in such a way that the main access path to both chambers is not blocked and that two teams can work in parallel without interference. There is the risk that the space is overcrowded so that work at both chambers is slowed down.

9 Control system and online analysis software

by U. Zastrau

9.1 Karabo

Here, we would only like to mention for completeness that the control software for the operation of all motors and other equipment will be neither EPICS nor TANGO, but the Karabo software package specially developed at the European XFEL (link).

9.2 Instrumentation-specific software and implementation

Some instruments, e.g. those that use streak cameras (VISAR, SOP) or special detectors (PerkinElmer), can only be operated with stand-alone (Windows) computers due to the need of using commercial software and drivers. These computers need a defined interface to transfer the images into Karabo, ideally in real time to allow online data processing.

9.3 VISAR and online shock parameters

The Karabo system can potentially analyse a VISAR image on the fly, give out essential parameters for each shock, and plot them as a function of shot number to monitor the stability and drifts of the experimental parameters.

9.4 Diffraction and online $S(k)$ plots

Data processing at higher repetition rate should come from a good standard program that can generate online waterfall diagrams of the last shots, rather than each group devising its own untested programs.

10 Timeline for first experiments

by U. Zastrau

10.1 Top-level milestones

For the coming years, we plan the following top-level milestones for the European XFEL project and the HED instrument:

- **November 2016**
  The SASE2 hutches are ready (all rooms with brick walls, lead walls, rack rooms, laser rooms, cranes, etc.).

- **December 2016**
  Basic infrastructure installation will start (air condition ducts, cable trays, AC units, etc.).

- **May 2017**
  HED hutch will be coarsely cleaned, installation of heavy equipment can start. IC1, the DiPOLE100X laser transport system, and the rail system can be installed.

- **July 2017**
  All the infrastructure will be ready, and the hutch will be thoroughly cleaned and painted. Electrical installations such as cables, air conditioning, water, and gases will be available. By this time, the HED and HIBEF teams will start to set up the HED instrument. This setup will commence with the optics hutch, with the large IC1 being commissioned in parallel. The beam transport system from the laser rooms will be fully installed in parallel, as space around IC1 is tight.

- **Autumn 2017**
  The SASE2 undulators may deliver first X-rays to the HED instrument, depending on the performance of the new linear accelerator and the SASE2 undulators. Once the optics hutch is ready, we will commission the optics hutch devices with X-ray beam up to the beamstop between optics and experiment hutch. During this time, the mechanical setups around IC1, differential pumping stages from IC1 to the optics hutch, slit systems, and laser beam transport for the HI, the DiPOLE100X, and the PP laser will be ongoing.

- **January 2018**
  Once the HED installations are ready to take beam, we will start to commission them step-by-step, starting from the optics hutch. Rooms will be interlocked frequently and access is limited.

- **Spring 2018**
  The DiPOLE100X laser and the 400 TW–class short-pulse laser will be delivered. Unpacking, setup, and full-scale commissioning will take a minimum of six months, possibly up to nine months.

- **Summer 2018**
  Early user operation with X-rays only (plus split and delay unit) will start.

- **Autumn 2018**
  As soon as the PP laser (up to 10 mJ short-pulse at 800 nm) is available, it can be commissioned and then made available for user experiments.

- **2019**
  At the time of this writing, we expect availability of the large HIBEF laser for users in the beginning of 2019.

10.2 Beamtime allocation

For the next years, we plan the following user hours:

- **2018**
  500 h: 2000 h for users, with two instruments operated at the time, effectively yields 4000 h for the entire European XFEL facility. This is divided by six instruments (yields 750 h) minus some spare for commissioning, not fully functioning, etc. (yields 500 h).

- **2019**
  2000 user hours at each instrument (shared bunch mode, regular operation of the facility). From these, 5% (8 shifts) is management reserve, 15% (25 shifts) is HED in-house time (commissioning, method development, and HED in-house research), up to 30% (50 shifts) is priority access for the HIBEF UC, and the remaining up to 50% (83 shifts) are available for regular proposals.

11 Bibliography

[1] O. L. Anderson. *Equations of state of solids for geophysics and ceramic science*. 31. Oxford University Press on Demand, 1995.

[2] R. J. Angel. “Equations of state”. In: *Reviews in Mineralogy and Geochemistry* 41 (2000), pp. 35–59.

[3] R. J. Angel, M. Bujak, J. Zhao, et al. “Effective hydrostatic limits of pressure media for high-pressure crystallographic studies”. In: *J Appl Crystallogr* 40.1 (January 2007), pp. 26–32. DOI: 10.1107/s0021889806045523.

[4] S. Anzellini, A. Dewaele, M. Mezouar, et al. “Melting of iron at Earths inner core boundary based on fast X-ray diffraction”. In: *Science* 340.6131 (2013), pp. 464–466.

[5] S. Banerjee, K. Ertel, P. D. Mason, et al. “DiPOLE: a 10 J, 10 Hz cryogenic gas cooled multi-slab nanosecond Yb:YAG laser”. In: *Optics express* 23.15 (2015), pp. 19542–19551.

[6] S. Banerjee, P. D. Mason, K. Ertel, et al. “100 J-level nanosecond pulsed diode pumped solid state laser”. In: *Optics letters* 41.9 (2016), pp. 2089–2092.

[7] L. M. Barker and R. E. Hollenba. “Shock-wave studies of PMMA, fused silica, and sapphire”. English. In: *J. Appl. Phys.* 41.10 (1970), p. 4208. DOI: 10.1063/1.1658439.

[8] B. Bendow and P. D. Gianino. “Optics of thermal lensing in solids”. In: *Applied optics* 12.4 (1973), pp. 710–718.

[9] A. Benuzzi-Mounaix, F. Dorchies, V. Recoules, et al. “Electronic structure investigation of highly compressed aluminum with K edge absorption spectroscopy”. In: *Phys. Rev. Lett.* 107.16 (2011), p. 165006.

[10] A. Benuzzi-Mounaix, M. Koenig, G. Huser, et al. “Absolute equation of state measurements of iron using laser driven shocks”. English. In: *Phys. Plasmas* 9.6 (June 2002), pp. 2466–2469. DOI: 10.1063/1.1478557.

[11] M. Bethkenhagen, D. Cebulla, R. Redmer, et al. “Superionic Phases of the 1:1 Water–Ammonia Mixture”. In: *The Journal of Physical Chemistry A* 119.42 (2015), pp. 10582–10588.

[12] F. Birch. “Finite Elastic Strain of Cubic Crystals”. In: *Phys Rev* 71.11 (1947), pp. 809–824. DOI: 10.1103/PhysRev.71.809.

[13] G. Blaj. “X-ray Imaging with ePix100a, a High-Speed, High-Resolution, Low-Noise Camera”. unpublished.

[14] G. Blaj, P. Caragiulo, G. Carini, et al. “Future of ePix detectors for high repetition rate FELs”. In: *AIP Conference Proceedings* (2016). DOI: 10.1063/1.4952884.

[15] C. Blome, T. Tschentscher, J. Davaasambuu, et al. “Femtosecond time-resolved powder diffraction experiments using hard X-ray free-electron lasers”. In: *J Synchrotron Radiat* 12.6 (October 2005), pp. 812–819. DOI: 10.1107/s0909049505026464.

[16] R. Boehler. “Temperatures in the Earth’s core from melting-point measurements of iron at high static pressures”. In: *Nature* 363 (1993), pp. 534–536.

[17] D. K. Bradley, J. H. Eggert, R. F. Smith, et al. “Diamond at 800 GPa”. In: *Phys. Rev. Lett.* 102 (7 February 2009), p. 075503. DOI: 10.1103/PhysRevLett.102.075503.

[18] A. Burrows and J. Liebert. “The science of brown dwarfs”. In: *Rev. Mod. Phys.* 65 (2 April 1993), pp. 301–336. DOI: 10.1103/RevModPhys.65.301.

[19] M. Cammarata, R. Bertoni, M. Lorenc, et al. “Sequential activation of molecular breathing and bending during spin-crossover photoswitching revealed by femtosecond optical and X-ray absorption spectroscopy”. In: *Phys. Rev. Lett.* 113.22 (2014), p. 227402.

[20] G. A. Carini, R. Alonso-Mori, G. Blaj, et al. “ePix100 camera: Use and applications at LCLS”. In: (2016). DOI: 10.1063/1.4952880.

[21] A. Cavalleri, C. Tóth, C. W. Siders, et al. “Femtosecond structural dynamics in VO_2 during an ultrafast solid-solid phase transition”. In: *Phys. Rev. Lett.* 87.23 (2001), p. 237401.

[22] C. Cavazzoni. “Superionic and Metallic States of Water and Ammonia at Giant Planet Conditions”. In: *Science* 283.5398 (January 1999), pp. 44–46. DOI: 10.1126/science.283.5398.44.

[23] P. M. Celliers, D. K. Bradley, G. W. Collins, et al. “Line-imaging velocimeter for shock diagnostics at the OMEGA laser facility”. In: *Rev. Sci. Instrum.* 75.11 (2004), pp. 4916–4929. DOI: 10.1063/1.1807008.

[24] G. Chabrier. “Plasma physics and planetary astrophysics”. In: *Plasma Phys. Contr. F* 51.12 (2009), p. 124014.

[25] J. Chihara. “Difference in X-ray scattering between metallic and non-metallic liquids due to conduction electrons”. In: *J. Phys. F Met. Phys.* 17 (1987), p. 295.

[26] J. Chihara. “Interaction of photons with plasmas and liquid metals – photoabsorption and scattering”. In: *J. Phys. Condens. Mat.* 12 (2000), p. 231.

[27] O. Ciricosta, S. Vinko, B. Barbrel, et al. “Measurements of continuum lowering in solid-density plasmas created from elements and compounds”. In: *Nature communications* 7 (2016).

[28] O. Ciricosta, S. Vinko, H.-K. Chung, et al. “Direct measurements of the ionization potential depression in a dense plasma”. In: *Phys. Rev. Lett.* 109.6 (2012), p. 065002.

[29] L. Claus, G. Robertson, L. Fang, et al. “Initial characterization results of a 1024 $\times$ 448 25-μm multi-frame camera with 2 ns integration time for the Ultrafast X-ray Imager (UXI) program at Sandia National Laboratories”. In: *Target Diagnostics Physics and Engineering for Inertial Confinement Fusion V* (September 2016). Ed. by J. A. Koch and G. P. Grim. DOI: 10.1117/12.2238538.

[30] A. J. Comley, B. R. Maddox, R. E. Rudd, et al. “Strength of Shock-Loaded Single-Crystal tantalum [100] determined using in situ broadband X-Ray Laue diffraction”. In: *Phys. Rev. Lett.* 110.11 (March 2013), p. 115501.

[31] J. A. D. Connolly. “The geodynamic equation of state: What and how”. In: *Geochem. Geophys. Geosyst.* 10.10 (October 2009).

[32] A. A. Correa, S. A. Bonev, and G. Galli. “Carbon under extreme conditions: Phase boundaries and electronic properties from first-principles theory”. In: *Proceedings of the National Academy of Sciences* 103.5 (January 2006), pp. 1204–1208. DOI: 10.1073/pnas.0510489103.

[33] A. Denoeud, A. Benuzzi-Mounaix, A. Ravasio, et al. “Metallization of Warm Dense SiO_2 Studied by XANES Spectroscopy”. In: *Physical Review Letters* 113.11 (September 2014). DOI: 10.1103/physrevlett.113.116404.

[34] T. Döppner, C. Fortmann, P. Davis, et al. “X-ray Thomson scattering for measuring dense beryllium plasma collisionality”. In: *Journal of Physics: Conference Series*. Vol. 244. 3. IOP Publishing. 2010, p. 032044.

[35] F. Dorchies, A. Lévy, C. Goyon, et al. “Unraveling the solid-liquid-vapor phase transition dynamics at the atomic level with ultrafast X-ray absorption near-edge spectroscopy”. In: *Physical review letters* 107.24 (2011), p. 245006.

[36] R. T. Downs and A. Singh. “Analysis of deviatoric stress from nonhydrostatic pressure on a single crystal in a diamond anvil cell: The case of monoclinic aegirine, $NaFeSi_2O_6$”. In: *Journal of Physics and Chemistry of Solids* 67.9-10 (September 2006), pp. 1995–2000. DOI: 10.1016/j.jpcs.2006.05.035.

[37] T. S. Duffy. “Some recent advances in understanding the mineralogy of Earth’s deep mantle”. In: *Philosophical Transactions of the Royal Society A: Mathematical, Physical and Engineering Sciences* 366.1883 (November 2008), pp. 4273–4293. DOI: 10.1098/rsta.2008.0172.

[38] T. S. Duffy. “Synchrotron facilities and the study of the Earth’s deep interior”. In: *Reports on Progress in Physics* 68.8 (July 2005), pp. 1811–1859. DOI: 10.1088/0034-4885/68/8/r03.

[39] A. M. Dziewonski and D. L. Anderson. “Preliminary reference Earth model”. In: *Physics of the Earth and Planetary Interiors* 25.4 (June 1981), pp. 297–356. DOI: 10.1016/0031-9201(81)90046-7.

[40] J. H. Eggert, G. Weck, P. Loubeyre, et al. “Quantitative structure factor and density measurements of high-pressure fluids in diamond anvil cells by x-ray diffraction: Argon and water”. In: *Physical Review B* 65.17 (2002), p. 174105.

[41] L. Ehm, F. M. Michel, and J. B. Parise. “Analysis of the Total Scattering Using the Quantitative High Pressure Pair Distribution Function: Case Studies”. In: *High-Pressure Crystallography* (2010), pp. 523–531. DOI: 10.1007/978-90-481-9258-8_43.

[42] P. Emma, R. Akre, J. Arthur, et al. “First lasing and operation of an ångstrom-wavelength free-electron laser”. In: *Nature Photonics* 4.9 (2010), pp. 641–647.

[43] O. Fabrichnaya and F. Aldinger. “Assessment of thermodynamic parameters in the system ZrO_2—Y_2O_3—Al_2O_3”. In: *MEKU* 95.1 (January 2004), pp. 27–39. DOI: 10.3139/146.017909.

[44] K. Falk, A. P. Jephcoat, et al. “Measurement of the dynamic response of compressed hydrogen by inelastic X-ray scattering”. In: *Journal of Physics: Conference Series*. Vol. 244. IOP Publishing. 2010, p. 042014.

[45] Y. Fei. “Thermal expansion”. In: *Mineral physics and crystallography: a handbook of physical constants* 2 (1995), pp. 29–44.

[46] L. Fletcher, E. Galtier, P. Heimann, et al. “Plasmon measurements with a seeded x-ray laser”. In: *Journal of Instrumentation* 8.11 (2013), p. C11014.

[47] L. Fletcher, H. Lee, T. Döppner, et al. “Ultrabright X-ray laser scattering for dynamic warm dense matter physics”. In: *Nature Photonics* 9.4 (2015), pp. 274–279.

[48] V. E. Fortov et al. “Phase Transition in a Strongly Nonideal Deuterium Plasma Generated by Quasi-Isentropical Compression at Megabar Pressures”. In: *Phys. Rev. Lett.* 99 (18 October 2007), p. 185001. DOI: 10.1103/PhysRevLett.99.185001.

[49] D. Fratanduono, T. Boehly, P. Celliers, et al. “The direct measurement of ablation pressure driven by 351-nm laser radiation”. In: *Journal of Applied Physics* 110.7 (2011), p. 073110.

[50] M. French, T. R. Mattsson, N. Nettelmann, et al. “Equation of state and phase diagram of water at ultrahigh pressures as in planetary interiors”. In: *Physical Review B* 79.5 (2009), p. 054107.

[51] E. Gamboa, P. Keiter, R. Drake, et al. “Spatially-resolved X-ray scattering measurements of a planar blast wave”. In: *High Energy Density Physics* 11 (2014), pp. 75–79.

[52] G. D. Gatta, I. Kantor, T. Boffa Ballaran, et al. “Effect of non-hydrostatic conditions on the elastic behaviour of magnetite: an in situ single-crystal X-ray diffraction study”. In: *Physics and Chemistry of Minerals* 34.9 (August 2007), pp. 627–635. DOI: 10.1007/s00269-007-0177-3.

[53] J. Gaudin, C. Fourment, B. Cho, et al. “Towards simultaneous measurements of electronic and structural properties in ultra-fast x-ray free electron laser absorption spectroscopy experiments”. In: *Scientific reports* 4 (2014).

[54] S. H. Glenzer and R. Redmer. “X-ray Thomson scattering in high energy density plasmas”. In: *Rev. Mod. Phys.* 81 (2009), pp. 1625–1663.

[55] S. Glenzer, L. Fletcher, E. Galtier, et al. “Matter under extreme conditions experiments at the Linac Coherent Light Source”. In: *Journal of Physics B: Atomic, Molecular and Optical Physics* 49.9 (2016), p. 092001.

[56] R. J. Goble and S. D. Scott. “Relationship between mineral hardness and compressibility(or bulk modulus)”. In: *Canadian Mineralogist* 23.2 (1985), pp. 273–85.

[57] S. Göde and et al. in preparation.

[58] M. G. Gorman, R. Briggs, E. E. McBride, et al. “Direct Observation of Melting in Shock-Compressed Bismuth With Femtosecond X-ray Diffraction”. In: *Physical Review Letters* 115.9 (August 2015). DOI: 10.1103/physrevlett.115.095701.

[59] G. Gregori and D. O. Gericke. “Low frequency structural dynamics of warm dense matter”. In: *Phys. Plasmas* 16 (2009), p. 056306.

[60] G. Gregori, S. H. Glenzer, and O. L. Landen. “Generalized x-ray scattering cross section from nonequilibrium plasmas”. In: *Phys. Rev. E* 74 (2 August 2006), p. 026402. DOI: 10.1103/PhysRevE.74.026402.

[61] E. Gregoryanz, L. F. Lundegaard, M. I. McMahon, et al. “Structural Diversity of Sodium”. In: *Science* 320.5879 (May 2008), pp. 1054–1057. DOI: 10.1126/science.1155715.

[62] C. L. Guillaume, E. Gregoryanz, O. Degtyareva, et al. “Cold melting and solid structures of dense lithium”. In: *Nature Physics* 7.3 (January 2011), pp. 211–214. DOI: 10.1038/nphys1864.

[63] T. Guillot. “The interiors of giant planets: Models and Outstanding Questions”. In: *Annual Review of Earth and Planetary Sciences* 33.1 (May 2005), pp. 493–530. DOI: 10.1146/annurev.earth.32.101802.120325.

[64] M. Harmand, F. Dorchies, O. Peyrusse, et al. “Broad M-band multi-keV x-ray emission from plasmas created by short laser pulses”. In: *Physics of Plasmas* 16.6 (2009).

[65] M. Harmand, C. Murphy, C. Brown, et al. “Plasma switch as a temporal overlap tool for pump-probe experiments at FEL facilities”. In: *Journal of Instrumentation* 7.08 (2012), P08007.

[66] M. Harmand, A. Ravasio, S. Mazevet, et al. “X-ray absorption spectroscopy of iron at multimegabar pressures in laser shock experiments”. In: *Physical Review B* 92.2 (2015), p. 024108.

[67] M. Harmand. “LCLS report 2016”. in preparation.

[68] J. Hawreliak, B. El-Dasher, H. Lorenzana, et al. “In situ x-ray diffraction measurements of the c/a ratio in the high-pressure ϵ phase of shock-compressed polycrystalline iron”. In: *Phys. Rev. B: Condens. Matter Mater. Phys.* 83.14 (April 2011).

[69] R. J. Hemley, R. Cohen, R. Kraus, et al. “The Iron Melting Curve and Magnetospheres of Habitable Super Earths”. Discovery Science on NIF campaign, FY16–18.

[70] B. Henrich, J. Becker, R. Dinapoli, et al. “The adaptive gain integrating pixel detector AGIPD a detector for the European XFEL”. In: *Nuclear Instruments and Methods in Physics Research Section A: Accelerators, Spectrometers, Detectors and Associated Equipment* 633 (May 2011), S11–S14. DOI: 10.1016/j.nima.2010.06.107.

[71] *HIBEF website*. http://www.hibef.de. Accessed: 2016-07-03.

[72] D. G. Hicks, T. R. Boehly, P. M. Celliers, et al. “Laser-driven single shock compression of fluid deuterium from 45 to 220 GPa”. In: *Phys. Rev. B* 79 (1 January 2009), p. 014112. DOI: 10.1103/PhysRevB.79.014112.

[73] D. Hicks, T. Boehly, P. Celliers, et al. “Shock compression of quartz in the high-pressure fluid regime”. English. In: *Physics of Plasmas* 12.8 (AUG 2005). DOI: 10.1063/1.2009528.

[74] *HiLASE Facility, Czech Republic*. http://www.hilase.cz/en/. 2016.

[75] A. Höll, T. Bornath, et al. “Thomson scattering from near-solid density plasmas using soft x-ray free electron lasers”. In: *High Energy Density Physics* 3.1 (2007), pp. 120–130.

[76] W. B. Holzapfel. “Equations of state for solids under strong compression”. In: *High Pressure Research* 16.2 (October 1998), pp. 81–126. DOI: 10.1080/08957959808200283.

[77] G. Huser, M. Koenig, A. Benuzzi-Mounaix, et al. “Interface velocity of laser shocked Fe/LiF targets”. English. In: *Physics of Plasmas* 11.10 (October 2004), pp. L61–L64. DOI: 10.1063/1.1785154.

[78] T. Ishikawa, H. Aoyagi, T. Asaka, et al. “A compact X-ray free-electron laser emitting in the sub-angstrom region”. In: *nature photonics* 6.8 (2012), pp. 540–544.

[79] S. D. Jacobsen, C. M. Holl, K. A. Adams, et al. “Compression of single-crystal magnesium oxide to 118 GPa and a ruby pressure gauge for helium pressure media”. In: *American Mineralogist* 93.11-12 (November 2008), pp. 1823–1828. DOI: 10.2138/am.2008.2988.

[80] JD. Lindl et al. “The physics basis for ignition using indirect-drive targets in the National Ignition Facility”. In: *Phys. Plasmas* 11 (2004), pp. 339–491.

[81] A. Karandikar and R. Boehler. “Flash melting of tantalum in a diamond cell to 85 GPa”. In: *Physical Review B* 93.5 (February 2016). DOI: 10.1103/physrevb.93.054107.

[82] B. B. Karki and L. Stixrude. “First-Principles Study of Enhancement of Transport Properties of Silica Melt by Water”. In: *Physical Review Letters* 104.21 (May 2010), p. 215901. DOI: 10.1103/physrevlett.104.215901.

[83] J. B. Kim, S. Göde, and S. H. Glenzer. “Development of a cryogenic hydrogen microjet for high-intensity, high-repetition rate experiments”. In: *Review of Scientific Instruments* 87.11 (August 2016), 11E328. DOI: 10.1063/1.4961089.

[84] M. D. Knudson, M. P. Desjarlais, and D. H. Dolan. “Shock-Wave Exploration of the High-Pressure Phases of Carbon”. In: *Science* 322 (December 2008), p. 1822.

[85] M. D. Knudson, M. P. Desjarlais, R. Lemke, et al. “Probing the Interiors of the Ice Giants: Shock Compression of Water to 700 GPa and 3.8 g/cm^3”. In: *Physical review letters* 108.9 (2012), p. 091102.

[86] M. Knudson, M. Desjarlais, A. Becker, et al. “Direct observation of an abrupt insulator-to-metal transition in dense liquid deuterium”. In: *Science* 348.6242 (2015), pp. 1455–1460.

[87] R. Kodama. in preparation. 2015.

[88] M. Koenig et al. “Progress in the study of warm dense matter”. In: *Plasma Physics and Controlled Fusion* 47.12B (2005), B441.

[89] A. Kritcher et al. “Ultrafast X-ray Thomson Scattering of Shock-Compressed Matter”. In: *Science* 322 (October 2008), pp. 69–71.

[90] S. Labrosse, J. W. Hernlund, and N. Coltice. “A crystallizing dense magma ocean at the base of the Earth’s mantle”. In: *Nature* 450.7171 (December 2007), pp. 866–869. DOI: 10.1038/nature06355.

[91] H. T. Lemke, C. Bressler, L. X. Chen, et al. “Femtosecond X-ray absorption spectroscopy at a hard X-ray free electron laser: application to spin crossover dynamics”. In: *The Journal of Physical Chemistry A* 117.4 (2013), pp. 735–740.

[92] B. Lengeler, C. G. Schroer, M. Richwin, et al. “A microscope for hard x-rays based on parabolic compound refractive lenses”. In: *Appl. Phys. Lett.* 74.26 (1999), pp. 3924–3926.

[93] W. Lorenzen, B. Holst, and R. Redmer. “First-order liquid-liquid phase transition in dense hydrogen”. In: *Phys. Rev. B* 82.19 (2010), pp. 195107–195112.

[94] A. Lutman, R. Coffee, Y. Ding, et al. “Experimental demonstration of femtosecond two-color x-ray free-electron lasers”. In: *Phys. Rev. Lett.* 110.13 (2013), p. 134801.

[95] A. Lutman, F.-J. Decker, J. Arthur, et al. “Demonstration of Single-Crystal Self-Seeded Two-Color X-Ray Free-Electron Lasers”. In: *Phys. Rev. Lett.* 113.25 (2014), p. 254801.

[96] M. MacDonald, P. Keiter, D. Montgomery, et al. “Demonstration of x-ray fluorescence imaging of a high-energy-density plasma”. In: *Review of Scientific Instruments* 85.11 (2014), 11E602.

[97] A. Mančić, A. Lévy, M. Harmand, et al. “Picosecond short-range disordering in isochorically heated aluminum at solid density”. In: *Physical review letters* 104.3 (2010), p. 035002.

[98] P. Mason, M. Fitton, A. Lintern, et al. “Scalable design for a high energy cryogenic gas cooled diode pumped laser amplifier”. In: *Applied Optics* 54.13 (2015), pp. 4227–4238.

[99] D. McGonegle, D. Milathianaki, B. A. Remington, et al. “Simulations of in situ x-ray diffraction from uniaxially compressed highly textured polycrystalline targets”. In: *J. Appl. Phys.* 118.6 (14 Aug. 2015), p. 065902.

[100] D. Milathianaki, S. Boutet, G. J. Williams, et al. “Femtosecond visualization of lattice dynamics in shock-compressed matter”. In: *Science* 342.6155 (November 2013), pp. 220–223.

[101] I. Miyamoto, H. Nanba, and H. Maruo. “CO_2 Lasers and Applications II”. In: *Proceedings of the SPIE*. Vol. 1276. 1990, pp. 112–121.

[102] A. Mozzanica, A. Bergamaschi, S. Cartier, et al. “Prototype characterization of the JUNGFRAU pixel detector for SwissFEL”. In: *Journal of Instrumentation* 9.05 (2014), p. C05010. DOI: 10.1088/1748-0221/9/05/C05010.

[103] F. D. Murnaghan. “A Theory of Elasticity”. In: *Phys. Rev.* 51 (7 April 1937), pp. 593–593. DOI: 10.1103/PhysRev.51.593.

[104] F. D. Murnaghan. “The Compressibility of Media under Extreme Pressures”. In: *PNAS* 30.9 (1944), pp. 244–247. DOI: 10.1073/pnas.30.9.244.

[105] N. Nettelmann et al. “Ab initio equation of state data for hydrogen, helium, and water and the internal structure of Jupiter”. In: *Astrophys. J.* 683 (2008), pp. 1217–1228.

[106] B. Nagler, B. Arnold, G. Bouchard, et al. “The Matter in Extreme Conditions instrument at the Linac Coherent Light Source”. In: *Journal of Synchrotron Radiation* 22.3 (May 2015). DOI: 10.1107/S1600577515004865.

[107] P. Neumayer, C. Fortmann, T. Döppner, et al. “Plasmons in Strongly Coupled Shock-Compressed Matter”. In: *Phys. Rev. Lett.* 105 (7 August 2010), p. 075003. DOI: 10.1103/PhysRevLett.105.075003.

[108] J. H. Nguyen and N. C. Holmes. “Melting of iron at the physical conditions of the Earth’s core”. In: *Nature* 427.6972 (2004), pp. 339–342.

[109] P. M. Nilson, J. R. Davies, et al. “Time-Resolved Measurements of Hot-Electron Equilibration Dynamics in High-Intensity Laser Interactions with Thin-Foil Solid Targets”. In: *Phys. Rev. Lett.* 108 (8 February 2012), p. 085002. DOI: 10.1103/PhysRevLett.108.085002.

[110] P. M. Nilson, W. Theobald, J. F. Myatt, et al. “Bulk heating of solid-density plasmas during high-intensity-laser plasma interactions”. In: *Phys. Rev. E* 79 (1 January 2009), p. 016406. DOI: 10.1103/PhysRevE.79.016406.

[111] J. B. Parise, L. Ehm, and F. M. Michel. “Analysis of the Total Scattering Using the Quantitative High Pressure Pair Distribution Function: Practical Considerations”. In: *High-Pressure Crystallography* (2010), pp. 513–522. DOI: 10.1007/978-90-481-9258-8_42.

[112] S. Pascarelli and O. Mathon. “Advances in high brilliance energy dispersive X-ray absorption spectroscopy”. In: *Physical Chemistry Chemical Physics* 12.21 (2010), pp. 5535–5546.

[113] Y. Ping, F. Coppari, D. G. Hicks, et al. “Solid Iron Compressed Up to 560 GPa”. In: *Physical Review Letters* 111.6 (August 2013). DOI: 10.1103/physrevlett.111.065501.

[114] *Powerpoint presentation of ESRF by S. Pascarelli*. http://www.esrf.eu. dated: 2016-01-19.

[115] G. Priebe, U. Zastrau, and M. Lederer. *Timing interfacing between XFEL and HIBEF user consortium*. Tech. rep. XFEL technical report, 2016.

[116] R. Ernstorfer, M. Harb, et al. “The Formation of Warm Dense Matter: Experimental Evidence for Electronic Bond Hardening in Gold”. In: *Science* 323 (2009), pp. 1033–1037.

[117] J.-Y. Raty, E. Schwegler, and S. A. Bonev. “Electronic and structural transitions in dense liquid sodium”. In: *Nature* 449.7161 (September 2007), pp. 448–451. DOI: 10.1038/nature06123.

[118] V. Recoules, J. Clérouin, G. Zérah, et al. “Effect of Intense Laser Irradiation on the Lattice Stability of Semiconductors and Metals”. In: *Phys. Rev. Lett.* 96.5 (February 2006), p. 055503.

[119] R. Redmer, T. R. Mattsson, N. Nettelmann, et al. “The phase diagram of water and the magnetic fields of Uranus and Neptune”. In: *Icarus* 211.1 (January 2011), pp. 798–803. DOI: 10.1016/j.icarus.2010.08.008.

[120] J. Robertson. “Diamond-like amorphous carbon”. In: *Mater. Sci. Eng. R* 37.4 (2002), pp. 129–281.

[121] S. Roling, H. Zacharias, L. Samoylova, et al. “Time-dependent wave front propagation simulation of a hard x-ray split-and-delay unit: Towards a measurement of the temporal coherence properties of x-ray free electron lasers”. In: *Physical Review Special Topics-Accelerators and Beams* 17.11 (2014), p. 110705.

[122] S. Roling, L. Samoylova, B. Siemer, et al. “Design of an X-ray split-and delay-unit for the European XFEL”. In: *SPIE Optical Engineering + Applications*. International Society for Optics and Photonics. 2012, pp. 850407–850407.

[123] M. Ross. “The ice layer in Uranus and Neptune—diamonds in the sky?” In: *Nature* 292.5822 (July 1981), pp. 435–436. DOI: 10.1038/292435a0.

[124] A. Rousse, C. Rischel, S. Fourmaux, et al. “Non-thermal melting in semiconductors measured at femtosecond resolution”. In: *Nature* 410.6824 (2001), pp. 65–68.

[125] J. R. Rygg, J. Eggert, A. Lazicki, et al. “Powder diffraction from solids in the terapascal regime”. In: *Review of Scientific Instruments* 83.11 (2012), p. 113904.

[126] S. Saxena. “Earth mineralogical model: Gibbs free energy minimization computation in the system MgO–FeO–SiO_2”. In: *Geochimica et Cosmochimica Acta* 60.13 (July 1996), pp. 2379–2395. DOI: 10.1016/0016-7037(96)00096-8.

[127] S. K. Saxena, N. Chatterjee, Y. Fei, et al. *Thermodynamic data on oxides and silicates: an assessed data set based on thermochemistry and high pressure phase equilibrium*. Springer Science & Business Media, 2012.

[128] C. G. Schroer, M. Kuhlmann, B. Lengeler, et al. “Beryllium parabolic refractive x-ray lenses”. In: *Design and Microfabrication of Novel X-Ray Optics*. Ed. by D. C. Mancini. Vol. 4783. Proceedings of the SPIE. Bellingham: SPIE, 2002, pp. 10–18.

[129] C. G. Schroer, B. Lengeler, B. Benner, et al. “Microbeam production using compound refractive lenses: beam characterization and applications”. In: *X-Ray Micro- and Nano-Focusing: Applications and Techniques II*. Ed. by I. McNulty. Vol. 4499. Proceedings of the SPIE. Bellingham, WA: SPIE, 2001, pp. 52–63.

[130] A. Schropp, R. Hoppe, V. Meier, et al. “Full spatial characterization of a nanofocused x-ray free-electron laser beam by ptychographic imaging”. In: *Scientific Reports* 3 (2013), p. 1633. DOI: 10.1038/srep01633.

[131] A. Schropp, R. Hoppe, V. Meier, et al. “Imaging Shock Waves in Diamond with Both High Temporal and Spatial Resolution at an XFEL”. In: *Scientific Reports* 5 (2015), p. 11089.

[132] F. Seiboth, A. Schropp, R. Hoppe, et al. “Focusing XFEL SASE pulses by rotationally parabolic refractive x-ray lenses”. In: *J. Phys. Conf. Ser.* 499 (2014), p. 012004.

[133] A. P. Shevelko, A. Antonov, et al. “Focusing crystal von Hamos spectrometer for x-ray spectroscopy and x-ray fluorescence applications”. In: *International Symposium on Optical Science and Technology*. International Society for Optics and Photonics. 2000, pp. 148–154.

[134] A. K. Singh, H. P. Liermann, S. K. Saxena, et al. “Nonhydrostatic compression of gold powder to 60 GPa in a diamond anvil cell: estimation of compressive strength from x-ray diffraction data”. In: *Journal of Physics: Condensed Matter* 18.25 (June 2006), S969–S978. DOI: 10.1088/0953-8984/18/25/s05.

[135] A. K. Singh. “The lattice strains in a specimen (cubic system) compressed nonhydrostatically in an opposed anvil device”. In: *Journal of Applied Physics* 73.9 (1993), pp. 4278–4286. DOI: 10.1063/1.352809.

[136] A. K. Singh, C. Balasingh, H.-k. Mao, et al. “Analysis of lattice strains measured under nonhydrostatic pressure”. In: *Journal of Applied Physics* 83.12 (1998), p. 7567. DOI: 10.1063/1.367872.

[137] A. K. Singh, H.-k. Mao, J. Shu, et al. “Estimation of Single-Crystal Elastic Moduli from Polycrystalline X-Ray Diffraction at High Pressure: Application to FeO and Iron”. In: *Physical Review Letters* 80.10 (March 1998), pp. 2157–2160. DOI: 10.1103/physrevlett.80.2157.

[138] B. J. Siwick, J. R. Dwyer, R. E. Jordan, et al. “An atomic-level view of melting using femtosecond electron diffraction”. In: *Science* 302.5649 (2003), pp. 1382–1385.

[139] J. H. Smith, A. Mozzanica, and B. Schmitt. “Technical Design Report”. In: (2015).

[140] R. Smith, J. Eggert, M. Saculla, et al. “Ultrafast dynamic compression technique to study the kinetics of phase transformations in bismuth”. In: *Phys. Rev. Lett.* 101.6 (August 2008), p. 065701.

[141] R. F. Smith, J. H. Eggert, A. Jankowski, et al. “Stiff Response of Aluminum under Ultrafast Shockless Compression to 110 GPA”. In: *Physical Review Letters* 98.6, 065701 (2007), p. 065701. DOI: 10.1103/PhysRevLett.98.065701.

[142] A. Snigirev, V. Kohn, I. Snigireva, et al. “A compound refractive lens for focusing high energy x-rays”. In: *Nature (London)* 384 (1996), p. 49.

[143] P. Sperling, E. J. Gamboa, et al. “Free-Electron X-Ray Laser Measurements of Collisional-Damped Plasmons in Isochorically Heated Warm Dense Matter”. In: *Phys. Rev. Lett.* 115 (11 September 2015), p. 115001. DOI: 10.1103/PhysRevLett.115.115001.

[144] P. Sperling, E. Gamboa, H. Lee, et al. “Free-electron x-ray laser measurements of collisional-damped plasmons in isochorically heated warm dense matter”. In: *Physical Review Letters* 115.11 (2015), p. 115001.

[145] F. Stacey and P. Davis. “High pressure equations of state with applications to the lower mantle and core”. In: *Physics of the Earth and Planetary Interiors* 142.3-4 (May 2004), pp. 137–184. DOI: 10.1016/j.pepi.2004.02.003.

[146] L. Stixrude. “Structure of Iron to 1 Gbar and 40 000 K”. In: *Physical Review Letters* 108.5 (February 2012), p. 055505. DOI: 10.1103/physrevlett.108.055505.

[147] M. J. Suggit, A. Higginbotham, J. A. Hawreliak, et al. “Nanosecond white-light laue diffraction measurements of dislocation microstructure in shock-compressed single-crystal copper”. In: *Nat. Commun.* 3 (January 2012), p. 1224.

[148] S. Sundaram and E. Mazur. “Inducing and probing non-thermal transitions in semiconductors using femtosecond laser pulses”. In: *Nature materials* 1.4 (2002), pp. 217–224.

[149] J. W. Swegle and D. E. Grady. “Shock viscosity and the prediction of shock wave rise times”. In: *J. Appl. Phys.* 58.2 (1985), p. 692.

[150] D. C. Swift and R. G. Kraus. “Properties of plastic ablators in laser-driven material dynamics experiments”. In: *Physical Review E* 77.6 (2008), p. 066402.

[151] D. C. Swift, R. G. Kraus, E. N. Loomis, et al. “Shock formation and the ideal shape of ramp compression waves”. In: *Physical Review E* 78.6 (2008), p. 066115.

[152] M. Tirone, J. Ganguly, and J. P. Morgan. “Modeling petrological geodynamics in the Earth’s mantle”. In: *Geochem. Geophys. Geosyst.* 10.4 (April 2009).

[153] S. Toleikis, R. Fäustlin, et al. “Soft x-ray scattering using fel radiation for probing near-solid density plasmas at few electron volt temperatures”. In: *High Energy Density Physics* 6.1 (2010), pp. 15–20.

[154] U. Zastrau, L. B. Fletcher, et al. “Bent crystal spectrometer for both frequency and wavenumber resolved x-ray scattering at a seeded free-electron laser”. In: *Rev. Sci. Instr.* (2014), under review.

[155] U. Zastrau, P. Audebert, et al. “Temperature and K_α-yield radial distributions in laser-produced solid-density plasmas imaged with ultrahigh-resolution x-ray spectroscopy”. In: *Phys. Rev. E* 81.2 (2010), p. 026406.

[156] B. F. Variano, N. E. Schlotter, D. M. Hwang, et al. “Investigation of finite size effects in a first order phase transition: High pressure Raman study of CdS microcrystallites”. In: *J. Chem. Phys.* 88.4 (1988), p. 2848. DOI: 10.1063/1.453969.

[157] S. Vinko, O. Ciricosta, B. Cho, et al. “Creation and diagnosis of a solid-density plasma with an X-ray free-electron laser”. In: *Nature* 482.7383 (2012), pp. 59–62.

[158] *Website of the DCS at the APS*. http://dcs-aps.wsu.edu/. accessed: 2016-01-19.

[159] H.-R. Wenk, I. Lonardelli, S. Merkel, et al. “Deformation textures produced in diamond anvil experiments, analysed in radial diffraction geometry”. In: *Journal of Physics: Condensed Matter* 18.25 (June 2006), S933–S947. DOI: 10.1088/0953-8984/18/25/s02.

[160] K. Widmann et al. “Single state measurement of electrical conductivity of warm dense gold”. In: *Phys. Rev. Lett.* 92 (2004), p. 125002.

[161] M. C. Wilding, M. Wilson, and P. F. McMillan. “Structural studies and polymorphism in amorphous solids and liquids at high pressure”. In: *Chemical Society Reviews* 35.10 (2006), p. 964. DOI: 10.1039/b517775h.

[162] M. Wöstmann, R. Mitzner, T. Noll, et al. “The XUV split-and-delay unit at beamline BL2 at FLASH”. In: *Journal of Physics B: Atomic, Molecular and Optical Physics* 46.16 (2013), p. 164005.

[163] K. Wünsch, P. Hilse, M. Schlanges, et al. “Structure of strongly coupled multicomponent plasmas”. In: *Phys. Rev. E* 77.5 (May 2008). DOI: 10.1103/physreve.77.056404.

[164] K. Wünsch, J. Vorberger, G. Gregori, et al. “X-ray scattering as a probe for warm dense mixtures and high-pressure miscibility”. In: *EPL (Europhysics Letters)* 94.2 (2011), p. 25001.

[165] H. Yoneda, Y. Inubushi, M. Yabashi, et al. “Saturable absorption of intense hard X-rays in iron”. In: *Nature communications* 5 (2014).

[166] U. Zastrau, C. Brown, et al. “Focal aberrations of large-aperture HOPG von-Hàmos x-ray spectrometers”. In: *Journal of Instrumentation* 7.09 (2012), P09015.

[167] U. Zastrau, E. Gamboa, et al. “Tracking the density evolution in counter-propagating-shocks on graphite using imaging x-ray scattering”. In: *Applied Physics Letters* ((under review) 2016).

[168] U. Zastrau, A. Sengebusch, et al. “High-resolution radial K_α spectra obtained from a multi-keV electron distribution in solid-density titanium foils generated by relativistic laser–matter interaction”. In: *High Energy Density Physics* 7.2 (2011), pp. 47–53.

[169] U. Zastrau, P. Sperling, M. Harmand, et al. “Resolving Ultrafast Heating of Dense Cryogenic Hydrogen”. In: *Phys. Rev. Lett.* 112.10 (2014), p. 105002. DOI: 10.1103/PhysRevLett.112.105002.

[170] U. Zastrau, A. Woldegeorgis, E. Förster, et al. “Characterization of strongly-bent HAPG crystals for von-Hámos x-ray spectrographs”. In: *Journal of Instrumentation* 8.10 (2013), P10006.

[171] J. Zhao, R. J. Angel, and N. L. Ross. “Effects of deviatoric stresses in the diamond-anvil pressure cell on single-crystal samples”. In: *J Appl Crystallogr* 43.4 (June 2010), pp. 743–751. DOI: 10.1107/s0021889810016675.

[172] D. Zhu, M. Cammarata, J. M. Feldkamp, et al. “A single-shot transmissive spectrometer for hard x-ray free electron lasers”. In: *Applied Physics Letters* 101.3 (2012), p. 034103.

A Scattering power

Calculations of scattered flux in a Diamond Anvil Cell with a 0.02 mm thick sample of Iron on a Perkin Elmer Detector using Blome et al. (2005)

From Blome et al. 2005 we find for N_P = photons per pixel,

$$N_{\mathrm{P}} = N_{hkl}\Delta(2\Theta)_{\mathrm{pixel}}/\Sigma. \tag{1}$$

where N_{hkl} = integrated number of photons, Σ = width of the Bragg peak, and $\Delta(2\theta)_{pixel}$ the angular size of the pixel. Here N_{hkl} is given by:

$$N_{hkl} = \frac{N_o \times T}{A}\left(\frac{e^4}{m_e^2 c^4}\right)\frac{V\lambda^3 m\left|F_{hkl}\right|^2}{4\nu^2}\frac{1}{\sin(\Theta)}\frac{\Delta y}{2\pi L\sin(2\Theta)} \tag{2}$$

Part 1 **Part 2** **Part 3** **Part 4** **Part5**

The values for the different parameters are as follows:

A) Part 1 (N_{eff} and Area)

N_o = Number of incident photons and T = Transmission can be combined in $N_{eff} = N_o$ x T = number of detectable photons

$T = T_{sample}T_{geo}T_{bw}$ with

T_{sample} = transition due to sample absorption at 25 keV of a 0.025 and 0.1 mm sample of iron = 0.78 and 0.35

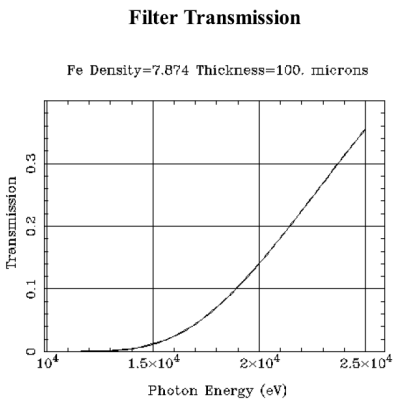

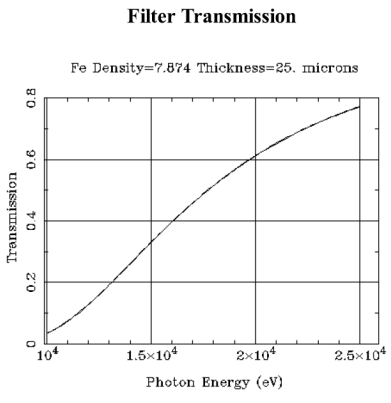

T_{geo} = transition due to geometrical absorption which should be 1 since there is no restriction.

T_{bw} = transition due to bandwidth reduction which could be covered by varying the initial amount of flux.

Table 1: Calculations for Np (photons per pixel) for Iron based on Blome et al. (2005).

Scenario	N_0 (ph/pulse)	T	N_{eff} (ph/pulse)	A (μm^2)	V (μm^3)	$\|F^2\|_{(110)}$	θ (degrees)	$N_{(110)}$	N_p
25 keV ($\Delta E/E$ 10^{-3} $BW)_{vac}$	10^{12}	0.78	7.8 x 10^{11}	400	10000	1401.943	7.027	5 x 10^5	2 x 10^5
		0.35	3.5 x 10^{11}	400	40000	1401.943	7.027	9 x 10^5	4 x 10^5
25 keV ($\Delta E/E$ 10^{-4} $BW)_{vac}$	10^{11}	0.35	3.5 x 10^{10}	400	40000	1401.943	7.027	3 x 10^4	2 x 10^4

With the above values $T = T_{sample} = 0.78$ and $T = T_{sample} = 0.35$ are for a thickness of iron foil of 25 and 100 um. The contribution from an ablator in front of the target are not considered in this calculation. For different incident flux values (based on the bandwidth) you then find the value for N_{eff} listed in Table 1.

The variable A is the scattering area that depends on the beam size. Here we assumed a size of 20 um. The volume is then depending on the different thicknesses to see the effect on absorption of the x-ray beam and scattering power. Thus, we suggest 25 and 100 µm resulting in an area of A = 1000 and 4000 μm^2.

B) Part 2

$$\frac{e^4}{m_e^2\ c^4} = 7.94\ \cdot\ 10^{-26} cm^2 =\ 7.94\ \cdot\ 10^{-18} \mu m^2$$

nagler2015matter

C) Part 3 (Volume, Wavelength, multiplicity, unit cell volume, structure factor)

- The scattering volume is dependent on the scattering area and the thickness of the sample. Since we choose different beam size scattering volume is going to vary as well.
  A = 1, 4, 25, 100, 400 and 900 μm^2
  Thickness = 25 µm
  V = 20, 80, 500, 2000, 8000, 18000 μm^3

- λ = wavelength (25 keV) = 0.4959 Å

- m = multiplicity for the bcc iron for example (110) has a multiplicity of 12 (values for other reflection see in Table 2)
- ν = unit cell volume for bcc iron = $(2.8665\ Å)^3 = 23.5412\ Å^3 = 2.354\ 10^{-11}\ \mu m^3$.

- $|F_{hkl}|$ = structure factor of the hkl reflection => we will pick the structure factor of the (110) reflection.

Attached are the necessary information on the multiplicity and the structure factor for iron bcc.

Space Group = I m 3 m
Cell Parameter a = 2.86650

(hkl)	Multiplicity	Sin(θ)/λ	2θ (degrees)	FWHM (degrees)	FWHM (mrad)	$\|F^2\|_{(hkl)}$
110	12	0.24668	14.054	0.07460	1.3	1401.943
200	6	0.34886	19.926	0.07281		962.564
211	24	0.42726	24.467	0.07147		717.654
220	12	0.49336	28.325	0.07035		566.096
310	24	0.55159	31.752	0.06939		465.816
222	8	0.60424	34.875	0.06853		396.264

Table 2: Diffraction information for bcc iron, Space Group = Im3m, Cell Parameter a = 2.86650 (from …).

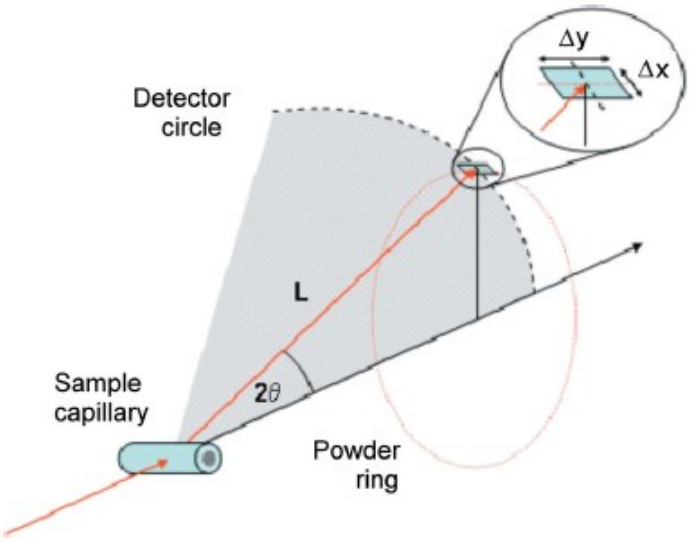

D) Part 4 and 5 (Diffraction Angle, SDD, pixel size)

- Diffraction angles are listed in table 2.
- The parameter L in formula (2) is dependent on the SDD which we assume to be a minimum of 300 mm, so that is becomes L = SDD/cos(2θ) = 309.2569.
- dy is related to illuminated area on the detector. Since the pixel size of the Perkin Elmer detector XRD1621 is 0.2 mm and we want to know how many photon one pixel will hit we approximate dy = 0.2 mm.

E) Np

From Formula (1) we can calculate the Np (photons per pixel). Here Σ = width of the Bragg peak in given in table 2 and $\Delta(2\theta)_{pixel}$ = angular size of the pixel can be calculated from $tg(2\theta_{+/-}) = \Delta$ +/- (dy/2) / SDD where D = tg(2θ)*SDD is the vertical distance at the SDD from the incident beam. The $\Delta(2\theta)_{pixel}$ (300 mm SDD) = 0.0359^{o} = 0.627 mrad.